NORTHWESTERN UNIVERSITY

Investigation of the Initiation, Progression and Treatment of Pediatric Gliomas

A DISSERTATION

SUBMITTED TO THE GRADUATE SCHOOL IN PARTIAL FULFILMENT OF THE REQUIREMENTS

for the degree of

DOCTOR OF PHILOSOPHY

Field of Driskill Graduate Training Program in Life Sciences

By

Aalaa Sanad Abdallah

EVANSTON, ILLINOIS

JUNE 2023

ABSTRACT

Pediatric high-grade gliomas (pHGGs) are aggressive pediatric CNS tumors and an important subset are characterized by mutations in *H3F3A*, the gene that encodes Histone H3.3 (H3.3). Substitution of Glycine at position 34 of H3.3 with either Arginine or Valine (H3.3G34R/V), was recently described and characterized in a large cohort of pHGG samples as occurring in 5-20% of pHGGs. Attempts to study the mechanism of H3.3G34R have proven difficult due to the lack of knowledge regarding the cell-of-origin and the requirement for co-occurring mutations for model development. We sought to develop a biologically relevant animal model of pHGG to probe the downstream effects of the H3.3G34R mutation in the context of vital co-occurring mutations. We developed a genetically engineered mouse model (GEMM) that incorporates PDGF-A activation, *TP53* loss and the H3.3G34R mutation both in the presence and loss of Alpha thalassemia/mental retardation syndrome X-linked (ATRX), which is commonly mutated in H3.3G34 mutant pHGGs. We demonstrated that ATRX loss significantly increases tumor latency in the absence of H3.3G34R and inhibits ependymal differentiation in the presence of H3.3G34R. Transcriptomic analysis revealed that ATRX loss in the context of H3.3G34R upregulates *Hoxa* cluster genes. We also found that the H3.3G34R overexpression leads to enrichment of neuronal markers but only in the context of ATRX loss. This study proposes a mechanism in which ATRX loss is the major contributor to many key transcriptomic changes in H3.3G34R pHGGs.

The Notch signaling pathway is a well-characterized and critical regulator of embryonic development as well as various adult processes. Notch signaling is also extremely active in glioma stem cells (GSCs), the precursor cells of glioma. Our next objective was to extract

information on the effects of H3.3G34R expression and/or ATRX loss on Notch signaling in pHGG and the associated underlying mechanisms. To achieve this goal, we extracted information on Notch ligands and associated genes from the RNA-Sequencing data we previously generated. In GEMMs of pHGG, we observed that ATRX and H3.3G34R expression promote Notch pathway activation independently of each other and that Notch pathway activation correlated with our previously reported changes in *Dll3* regulation. We then utilized patient-derived orthotopic xenograft (PDOX) models of pHGG to confirm association of Notch pathway activation and both ATRX and H3.3G34R expression. Overall, we found that while ATRX loss and H3.3G34R expression both independently activate Notch, ATRX loss is the main contributor to NOTCH pathway activation in tumor samples.

The protein growth arrest-specific protein 6 (GAS6) is a high-affinity ligand for AXL and serves as an activator of AXL signaling. Important downstream pathways of AXL/GAS6 signaling include PI3K/AKT/mTOR, JAK/STAT, NFkB, and RAS/RAF/MEK/ERK, which influence tumor cell survival, apoptosis, therapeutic resistance and angiogenesis. Aberrant expression of AXL is associated with poorer overall survival and cancer progression. AXL and GAS6 are highly expressed in a large subset of adult glioblastoma where high expression of AXL and/or AXL/GAS6 was associated with significantly shorter tumor progression and overall survival. AVB-500 is a fusion protein which binds to GAS6, ablating the AXL/GAS6 signaling pathway. We assessed the therapeutic efficacy and acute downstream molecular mechanisms of AVB-500 in PDOX mouse models of pediatric glioblastoma. Overall, AVB-500 had did extend median survival times however the difference did not reach statistical significance. We also observed that 24 hours after treatment with AVB-500, markers of angiogenesis were

downregulated. AVB-500 represents a promising therapeutic target for pediatric glioblastoma though further optimization of dosage and timing are required.

DEDICATION

In the Name of Allāh, the Most Gracious, the Most Merciful

I dedicate this body of work to my mother, Samia Ibrahim, who sacrificed without thought and stopped at nothing in order to give her children a better life.

ACKNOWLEDGEMENTS

First, I would like to express my immense gratitude to my thesis committee: Dr. Daniel Foltz, Dr. Daniel Brat, and Dr. Samantha Gadd. Your advice, guidance, and expertise were invaluable to my project. I picked you all because I thought you were nice and good at science; turns out I was right on both accounts! A huge thank you to Dr. Oren Becher and the former Becher lab, including Megan Romero, Radhika Patel, Emily Kagan, Dr. Christine Hoeman, Dr. Swati Dhar, and Dr. Chen Shen. Special thanks to my first official graduate school mentor, Joey Cardona. You taught me everything I know – so this was all your fault. Oren – I don't think there is anyone else who is so acutely aware of my failures as you – thanks for not telling anyone about those. And thank you for looking out for me when even I wasn't quite sure I deserved it.

I have been lucky to enjoy the help of countless professors, admins, staff, post-docs, and students throughout the last five years. Thank you to Dr. Erin Baker, Archer Curry, Dr. Emma Leichty and Brooke Palmer whose diligence and compassion for animals made me a much better researcher. To Dr. Mary Ross Newman – thanks for taking care of me. A huge thank you to Amreena Suri, Dr. Loretta Li, Dr. Matt Arwood, Madeleine Muller, and Joann Taylor for putting up with my noisiness and always being available for a friendly chat – there were days were I don't think you guys realized just how much I needed that. Thank you to the DGP office, Dr. Toni Gutierrez, Dr. Steve Anderson, Grace Musante, Dr. Cara Gottardi and Dr. Pam Carpentier for their grace, guidance, and unending patience. Pam – sorry about all that stuff I said. You're actually very nice and cool.

Thank you to my Los Angeles family who cared me for me from afar when I was really missing the LA sunshine: Anthony Barreras, Chelsea Montgomery, Jayne Weigley, Irene McDermott, Hanz Legaspi, Sara Sallam, and Shamms Fahmawi – I promise to text more! Thank

you so much to Leyla Ramadan and Fatima Elmohrak for being my 2nd and 3rd moms (and looking after my 1st mom while I've been away)! A huge thank you to Dr. Christine Dauphine, Dr. Jamil Momand, Dr. Krishna Foster, and the CSULA MORE programs, who all worked very hard to prepare me for this whole PhD thing.

Thank you to my numerous public health families including those at the Lurie DSD clinic, the REACH lab, and the MPH program: Dr. Laura Rasmussen-Torvik, Adrienne Marks, Allison Weisman, Dr. J Whitehead, Dr. Emilie Johnson, Dr. Monica Laronda, Sophia Kamanzi, Josephine Hirsch, Danielle Lee, Dr. Courtney Finlayson, Dr. Jaclyn Papadakis, Dr. Briahna Yuodsnukis, Dr. Elizabeth Yerkes, Dr. Diane Chen, Dr. Earl Cheng, and Dr. Lauren Beach. Special shout out to Adam Davies, the best boss I've ever had. Lauren – my only regret is that I didn't meet you sooner. I thought I knew everything about research but you showed me just how much I still have to learn. I think you might be the best researcher ever.

An absolutely gargantuan thank you to Dr. Xiao-Nan Li as well as the current and former members of the Li Lab – Dr. Yuchen Du, Sophie Xiao, Dr. Casey Mehrhoff, Dr. Milagros Suarez, Dr. Deying Yang, Lauren Leung, Dr. Zilu Huang, and Dr. Alice Zhai. Sophie – you didn't have to be that nice to me, you know. But I guess that's just who you are. Dr. Du – everyone around me helped make me a good scientist but you always seemed to believe that I could be great. Your kind words and belief in me made me want to be great too. And of course, to Dr. Li – you took a chance on me and I will forever be indebted to you. I am reminded of your kind spirit and generosity every day we work alongside each other. Thank you for showing me the role that integrity and empathy have in research. You are not only a great scientist but also an incredibly decent person.

Thank you to my wonderful friends, Shuvam Chaudhuri, Elizabeth Tsui, Nathan Hodge, Jenai Quan, Shweta Dipali, Jocelyn Salvador, Viriya Keo, Vanessa Hayashi, Alex Shirley, Megan Riley, Corey Dussold, Sharon Tam, Alex Duval, Jamie Guillen, Hannah Mubarak, Ala Elmashae, and Haneen Amouri, whom I've spent hours and days and weeks leaning on and enjoying the company of. Alf shukr to Nora, Sarah H., Katie, and Sarah D. for improving my Arabic and my mood for the last year (and also Rashid). To Wendy Geslewitz and Rebecca Southern – the more support I needed, the more you guys gave. I will always be grateful for that. To Celeste Rosencrance, thank you for being my first (and easily my coolest) friend in this city – and thank you for telling me where to buy a winter coat! To Jennifer Cheng, who not only gifted me her friendship but also made me a better friend in the process – every time I talk to you, I somehow like you even more. And finally, to Hana Kubo and Esther Liu, two of the best friends I have ever had. The only time I ever actually considered staying is when I realized that leaving Chicago meant leaving the two of you. You both saw me as I truly was and still showed up every day. In my worst nightmares, I had to do this without you.

Truly none of this would have been possible without the help of Kim Seokjin, Eunha, and Sana. Special thanks to IU, Jeon Jeongguk, Umji, Min Yoongi, Choi Soobin, Heuning Kai, Yerin, Park Jimin, Choi Yeonjun, Yuju, Kim Taehyung, Kang Taehyun, SinB, Kim Namjoon, Choi Beomgyu, Sowon, and Jung Hoseok. Further thanks to Yuna, Ryujin, Yeji, Chaeryeong, Lia, Jihyo, Nayeon, Jeongyeon, Tzuyu, Momo, Chaeyoung, Dahyun, Mina, Bangchan, Changbin, Hyunjin, Han, Felix, I.N., Lee Know, Seungmin, Mamamoo, SHINee, Red Velvet, aespa, BlackPink, NCT, (G)I-dle, Seventeen, STAYC, Billlie, Dreamcatcher, CSR, Limelight, Le Sserafim, WJSN, Oh My Girl, Momoland, NewJeans, Enhyphen, Everglow, Loona, NMixx, Sunmi, SNSD, Exo, GOT7, ATEEZ, iKon, Big Bang, and Apink. Thanks to Fog, JT, Mango,

Zeg, Josh, Nikki, and the KPK discord for getting me through the final months of my PhD. And thanks to RJ for getting me through all the middle parts.

To the city of Chicago – I see what you did there! I'm not going to say it. You can't make me say it! But seriously, what am I supposed to do with all this winter wear?

To my nephews and niece, Christopher Davis, Kyle Davis, and Sana Abdallah – thank you all for being so ADORABLE! To Evelyn McDermott – I literally don't know what to write about you…you know me better than anyone so just read my mind and add that here. To my sister, Summer Davis – no one has taught me more about responsibility than you. I definitely understand why you're the favorite. To Khadijah Abdallah, my dear sister – I'm so glad you ended up not sucking. Thank you for your support and willingness to always give it to me straight – you were always destined to be an older sister. To my late father, Sanad Abdallah – it took me a while to realize it but more than anyone else, you were the person who set me on this path. Perhaps all these unexplained parts of myself can also be traced back to you.

To my brother, Ahmad Abdallah – I don't always make it obvious but I hope you know just how much I respect your guidance and advice. There are few opinions I value more highly than yours. Oh and thanks for marrying Khadijah, she's great. To Sarah Abdallah, my big sister and one of my first teachers – you've got a lot of great traits but I am always in awe of your generosity. Whether it was money, time, energy, or knowledge, you shared everything with me as if it was a foregone conclusion. To every iteration of myself, especially the ones I hated the most – thank you. I promise to spend just as much time celebrating your successes as I do learning from your mistakes. And finally, for my precious mother, Samia Ibrahim – everyone else helped but without you, it would have been impossible. So really, this PhD belongs to both of us. Congratulations Dr. Ibrahim!

LIST OF ABBREVIATIONS

ALT – Alternative Lengthening of Telomeres

ATAC-Seq – Assay for Transposase-Accessible Chromatin with Sequencing

ATRX - Alpha-Thalassemia/Mental Retardation, X-linked

CCM – Center for Comparative Medicine

ChIP-Seq – Chromatin Immunoprecipitation Sequencing

CNS – Central Nervous System

CUT&RUN - Cleavage Under Targets & Release Using Nuclease

DAXX – Death Domain-Associated protein

DMEM - Dulbecco's Modified Eagle Medium

DOS - Delta and OSM-11-like proteins

DSL - Delta/Serrate/LAG-2

EMT – Epithelial-to-Mesenchymal Transition

FBS – Fetal Bovine Serum

FFPE - Formalin-Fixed Paraffin-Embedded

fl/fl – Flox/Flox

GAS6 - Growth Arrest Specific 6

GBM - Glioblastoma

GCTB – Giant Cell Tumor of the Bone

GEMM – Genetically Engineered Mouse Model

GSC – Glioma Stem Cell

GSEA – Gene Set Enrichment Analysis

H&E – Hematoxylin & Eosin

i.p. – Intraperitoneal

IACUC - Institutional Animal Care & Use Committee

IDH – Isocitrate Dehydrogenase

IF - Immunofluorescence

IHC - Immunohistochemistry

IRB – Institutional Review Board

IUE – In Utero Electroporation

KO – Knock Out

LoF – Loss of Function

NPC – Neural Progenitor Cell

NSC – Neural Stem Cell

Ntv-a – Nestin Tumor Virus A

OL - Oligodendrocytes

OPC – Oligodendrocyte Precursor Cells

PDOX – Patient Derived Orthotopic Xenograft

pHGG – Pediatric High-Grade Glioma

PNET - Primitive Neuro-Ectodermal Tumors

RCAS - Replication-Competent ASLV long terminal repeat (LTR) with a Splice acceptor

rpm – Rotations Per Minute

RT-qPCR - Quantitative Real-Time Polymerase Chain Reaction

RTK – Receptor Tyrosine Kinase

SCID – Severe Combined Immunodeficiency

SCLC – Small Cell Lung Cancer

STR – Short Tandem Repeat

SVZ – Subventricular Zone

Telo-FISH – Telomere Fluorescence In Situ Hybridization

WT - Wildtype

XRT – Fractionated Radiation

Y – Empty Vector

LIST OF FIGURES

Figure 14. RT-qPCR assessment of *Dll3* expression in an *ex vivo* RCAS progenitor model and PDOX models and Representative DLL3 staining of three PDOX models.

Figure 15. Expression of AXL mRNA in a panel of xenograft mouse models of pediatric brain cancers.

Figure 16. In vivo therapeutic efficacy of AVB-500 in PDOX models of childhood brain tumors.

Figure 17. Representative imaging indicating no significant changes to gross morphology in IC-1406 GBM, IC-2305GBM, or IC-104488GBM.

Figure 18. IC-3938GBM representative imaging confirming tumor formation and for markers of angiogenesis.

LIST OF TABLES

TABLE OF CONTENTS

CHAPTER 1: Novel genetically engineered H3.3G34R model reveals cooperation with ATRX loss in upregulation of PRC2 targets and promotion of neuronal lineage

1.1 Introduction

1.1.1 G34R Pediatric High-Grade Glioma (pHGG)

1.1.1.1 Epidemiology, Etiology and Classification

Tumors of the central nervous system (CNS) are the most common type of solid tumor of childhood and the leading cause of pediatric cancer deaths[1,2]. pHGGs are among the most aggressive pediatric CNS tumors, with a poor survival rate[3]. A large subset of pHGGs harbor recurrent mutations in histone variant H3.3, namely H3.3K27M and H3.3G34R/V[4,5]. Histone H3.3 is encoded by *H3F3A* and *H3F3B* and are non-canonical as they are deposited onto chromatin independent of the cell cycle. Histone H3.3 is deposited onto both euchromatin and heterochromatin, including at telomeres and pericentric repeats by the Alpha-thalassemia/mental retardation, X-linked (ATRX)/Death domain-associated protein (DAXX) complex and H3.3G34 mutant pHGGs almost always contain *ATRX* mutations[6-8]. The recently published inaugural WHO classification of pediatric tumors contains a dedicated section for Pediatric-type diffuse high-grade gliomas defined by H3 status, including the first instance of H3.3G34-mutant pediatric tumors receiving their own official subclassification[9].

1.1.1.2 Genetic Aberrations, Treatment, and Prognosis

Much of the work done to elucidate the effects of H3.3 driver mutations on pHGG tumorigenesis has focused on the H3.3K27M mutation[9-12]. While H3.3K27M and H3.3G34R/V pHGGs have been reported to share many similarities, such as induction of Notch pathway genes, H3.3K27M and H3.3G34 mutations are mostly mutually exclusive.[5,13,14] In further contrast to H3.3K27M, H3.3G34 mutations only occur in H3F3A and H3.3G34R pHGGs are restricted to the cerebral hemispheres, typically arising in adolescents and young adults[14].

H3.3G34R-mutant pHGGs almost always co-occur with *TP53* loss and commonly contain PDGFRA amplifications[14]. The mechanism through which the H3.3G34R onco-histone functions during pHGG initiation and progression has not been fully elucidated though it has been continually shown that H3.3G34 mutations impede H3K36 methylation *in cis*, likely through repression of SETD2 activity[15]. Recent *in vitro* studies utilizing immortalized mesenchymal stem cells suggest that H3.3G34R and H3.3G34W, an H3.3G34 mutation found in most of the Giant Cell Tumor of the Bone (GCTB), impedes H3K36 methylation via SETD2 disruption[16]. H3.3G34R/V expression does not appear to have any effect on global H3K27me3 expression and very subtle cell-specific effects; it was separately shown that cells containing H3.3G34L/W mutations are indeed enriched for H3K27me3 at specific loci[15,17].

1.1.1.3 Murine Models of G34R pHGG

While there is biochemical justification to believe that mechanisms of H3.3G34 driven tumorigenesis are similar across different organ systems, the exclusivity of particular H3.3G34 mutations to their respective tumor types (H3.3G34W to GCTB and osteosarcoma and H3.3G34R/V to pHGG) necessitates study of these mutations in appropriate model systems[16-18]. Almost all successfully developed GEMMs of H3.3G34 mutant HGGs have incorporated ATRX loss, making it difficult to differentiate between the effects of ATRX status or H3.3G34 mutations on tumorigenesis.

1.1.2 ATRX

1.1.2.1 Canonical ATRX Function

ATRX, a member of the SWI/SNF family of chromatin remodelers, is a 280 kDa protein encoded by the gene *ATRX*, which lies on the long arm of the X chromosome in humans[19,20]. Spontaneous mutations in *ATRX* at the transcript level can induce severe neurological deficiencies (ATRX syndrome), from which the gene and protein product get its name[21,22]. While in complex with the protein DAXX, ATRX facilitates deposition of H3.3 onto the chromatin[6]. ATRX also interacts with H3.3 to maintain telomere structure[8].

1.1.2.2 ATRX Dysregulation in Glioma

ATRX mutations have been reported in both adult and pediatric glioma where the primary mutation result is inactivation or loss-of-function (LoF)[23,24]. In adults, ATRX mutation is associated with isocitrate dehydrogenase (IDH) mutations and associated favorable outcomes[25]. ATRX loss of function is associated with *TP53* mutations, PDGFRA amplification, and the alternative lengthening of telomeres (ALT) phenotype[23,24,26].

1.1.3 Objective and Hypothesis

Our objective was to develop a model of pHGG which recapitulates key features of H3.3G34 mutant gliomas and use it to elucidate the role of the H3.3G34R mutation in the context of ATRX status in pHGG initiation and progression. To achieve our objective, we utilized the RCAS/tv-a avian retroviral system to develop a genetically engineered mouse model (GEMM) which incorporates either H3.3WT or H3.3G34R mutant, PDGF-A activation and *TP53* loss, in the context of both ATRX wild-type (WT) and ATRX knock-out (KO), thus

providing one of the first immunocompetent GEMMs of H3.3G34-mutant pHGG. We found that in our glioma model, overexpression of H3.3G34R does not significantly affect tumor latency or survival relative to overexpression of H3.3WT. We observed that in the absence of H3.3G34R, ATRX loss significantly increases tumor latency and survival but in the presence of H3.3G34R overexpression, ATRX did not significantly impact tumor latency suggesting that the two drivers, ATRX loss and H3.3G34R, cooperate in tumorigenesis. We also found that ATRX loss in the context of H3.3G34R inhibits ependymal differentiation, upregulates *Hoxa* cluster genes, and H3.3G34R overexpression leads to enrichment of neuronal markers but only in the context of ATRX loss.

1.2 Materials and Methods

1.2.1 Cell Lines and Reagent

1.2.1.1 Fibroblast Cell Lines

DF1 cells were grown in complete Dulbecco's Modified Eagle Medium (DMEM) media supplemented with 10% fetal bovine serum (FBS), 2mM L-glutamine, 100U Penicillin and, 100ug streptomycin). All cell lines were cultured within a humidified 37ºC, 5% CO_2 incubator and authenticated through short tandem repeat (STR) profiling at least once per year.

1.2.1.2 Plasmid Constructs

Replication Competent ALV LTR with a Splice Acceptor (RCAS) empty vector (Y) constructs were purchased from Addgene. RCAS-H3.3G34R-GFP, RCAS-H3.3WT-GFP, RCAS-PDGFA, RCAS-Cre, and RCAS-GFP plasmids were developed by and purchased from Eton Bioscience.

1.2.1.3 Cell Transfections

DF1 cells were seeded at a density of 200,000 cells/T-25 flask one day prior to transfection and allowed to grow overnight. For each transfection, 8 uL of X-tremeGENE 9 (Roche) and 243 uL DMEM in a 1.5 mL Eppendorf tube then incubated at room temperature for 5 minutes. 2.5 ug of plasmid was then added to the mixture and incubated at room temperature for 20 minutes. Previously cultured DF-1 cells in T-25 flasks had media (complete DMEM) changed and the transfection mixture was added dropwise into the flask while swirling. Each flask was allowed to grow overnight within a humidified 37ºC, 5% CO2 incubator and monitored

for GFP expression in the case of GFP expressing plasmids. Transfected cells were passaged at confluency a minimum of 3 times before use in GEMM experiments.

1.2.1.4 Antibodies

The following antibodies were used at the indicated dilutions: anti-ATRX (abcam #ab188027, 1:100), anti-GFAP (Cell Signaling Technology #3670S, 1:50), anti-Ki67 (Cell Signaling Technology #12202, 1:400), anti-EMA (Roche Diagnostics, # 05878900001), anti-Olig2 (Millipore #AB9610, 1:500), anti-PDGFRA (Cell Signaling Technology, #3174T, 1:1000), anti-pERK1/2 (ABclonal, #AP0472, 1:100), anti-Iba1/AIF-1 (Cell Signaling Technology, #17198T, 1:1500), and anti-H3.3G34R (abcam, #ab254402, 1:1000).

1.2.2 Animal Studies

1.2.2.1 Animal Experiment Study Approval

All experiments with mice were completed in accordance with Northwestern University Center for Comparative Medicine (CCM) guidelines and Institutional Animal Care and Use Committee approved protocols (IACUC, protocol I500005132).

1.2.2.2 Mouse Strains

C57BL/6 mice were purchased from Jackson Laboratories, then housed and bred in the animal facility of Northwestern University, Feinberg School of Medicine.

1.2.2.3 Genetically Engineered Mouse Lines

Mice with conditional p53 deletion ($p53^{fl/fl)}$ and mice with conditional expression of the RCAS receptor tv-a bound to a Nestin specific promoter (Ntv-a) were purchased from Jackson Laboratory. Ntv-a and $p53^{fl/fl}$ mice were crossed until we yielded mice which homozygously expressed all alleles (Ntv-a;$p53^{fl/fl}$). ATRX flox/flox mice ($ATRX^{fl/fl}$) were generously provided by David Picketts. Ntv-a;$Np53^{fl/fl}$ mice were crossed with $ATRX^{fl/fl}$ until all alleles were homozygously expressed (Ntv-a;$p53^{fl/fl}$;$ATRX^{fl/fl}$). Homozygous expression was confirmed via genotyping (*see 1.2.2.5*).

1.2.2.4 Tail Snip Digestion

Tail snips were obtained from mice before 28 days of age. For Ntv-a and $p53^{fl/fl}$ genotyping, DNA was extracted from tail snips with the REDExtract-N-Amp Tissue PCR Kit Protocol (Millipore Sigma). For $ATRX^{fl/fl}$ genotyping, tail snips were submerged in 100uL lysis buffer (100mM Tris-HCl (pH 8.5), 5 mM EDTA, 0.2% SDS, 200 mM NaCl) supplemented with 0.5% Proteinase K and incubated at 55 ºC overnight. Reaction tubes were mixed, incubated at 55ºC for an additional 2 hours then briefly centrifuged at 10,000 rotations per minute (rpm). 100 uL of 2-proponal was added to each tube then tubes were centrifuged for 10 minutes at 10,000 rpm. Supernatant was removed, DNA pellet was left to dry at 37ºC for 3 hours then DNA was resuspended in 100 uL of TE buffer. Concentration of resuspended DNA was measured with a NanoDrop spectrophotometer (ThermoScientific) then stored at 4 degrees until ready to be genotyped.

1.2.2.5 Genotyping

For Ntv-a and $p53^{fl/fl}$ genotyping, PCR amplification was done with the REDExtract-N-Amp PCR Reaction mix (Millipore Sigma) with appropriate primers (Table 1). For $ATRX^{fl/fl}$ genotyping, PCR amplification was done with the KAPA2G Fast PCR Kit (KAPA Biosystems). PCR products were run on a 1% agarose gel. Prescence of the Ntv-a, $p53^{fl/fl}$, and $ATRX^{fl/fl}$ alleles were confirmed by presence of only one band at 800 base pairs (Ntv-a), only one band at 390 base pairs ($p53^{fl/fl}$), and a greater than 1500 base pair band for the wildtype reaction and 1500 base pair band for the mutant reaction ($ATRX^{fl/fl}$) (Table 1).

Table 1. Genotyping primers.

Allele	Primer Sequence	Direction
Ntv-a	CAGGACCCTCCTGGAGGCTGA	Forward
Ntv-a	GCCCTGGGGAAGGTCCTGCCC	Reverse
$p53^{fl/fl}$	GGTTAAACCCAGCTTGACCA	Forward
$p53^{fl/fl}$	GGAGGCAGAGACAGTTGGAG	Reverse
$ATRX^{fl/fl}$	GGTTTTAGATGAAAATGAAGAG	Forward for wildtype and mutant reactions
$ATRX^{fl/fl}$	TGAACCTGGGGACTTCTTTG	Reverse primer for wildtype reaction
$ATRX^{fl/fl}$	CCACCATGATATTCGGCAAG	Reverse primer for mutant reaction

1.2.2.6 RCAS/tv-a Mouse Modeling

We used the RCAS/tv-a system to overexpress Cre, PDGF-A, and either H3.3G34R-GFP, H3.3WT-GFP or empty vector in two different strains of mice. DF-1 cells expressing

RCAS were spun down for 5 minutes at 5,000 rpm, resuspended in 30 uL of complete DMEM media then combined appropriately to develop each model (Table 2).

Table 2. Summary of experimental design for RCAS models.

Model	Transfected RCAS expressing cells	Mouse strain
H3.3G34R – ATRX KO	RCAS-H3.3G34R, RCAS-Cre, RCAS-PDGFA	Ntv-a;$p53^{fl/fl}$;$ATRX^{fl/fl}$
H3.3WT – ATRX KO	RCAS-H3.3WT, RCAS-Cre, RCAS-PDGFA	Ntv-a;$p53^{fl/fl}$;$ATRX^{fl/fl}$
Empty Vector – ATRX KO	RCAS-Y, RCAS-Cre, RCAS-PDGFA	Ntv-a;$p53^{fl/fl}$;$ATRX^{fl/fl}$
H3.3G34R – ATRX WT	RCAS-H3.3G34R, RCAS-Cre, RCAS-PDGFA	Ntv-a;$p53^{fl/fl}$
H3.3WT – ATRX WT	RCAS-H3.3WT, RCAS-Cre, RCAS-PDGFA	Ntv-a;$p53^{fl/fl}$
Empty Vector – ATRX WT	RCAS-Y, RCAS-Cre, RCAS-PDGFA	Ntv-a;$p53^{fl/fl}$

Resuspended RCAS cell cocktails were injected at 1.2 uL into the cortex of individual mice from the appropriate strain between postnatal days 3-5. Injected mice were weighed every other day and monitored daily until tumor symptoms became apparent (20% weight loss, enlarged head, ataxia, seizing or paralysis). Asymptomatic mice were euthanized after 210 days. Once endpoints were reached, mice were euthanized with CO_2, and brains were removed and either had tumors excised or were fixed with 10% formalin for at least 24 hours before embedding in paraffin for histological and immunohistochemical analysis.

1.2.2.7 Euthanasia

Mice were euthanized in compliance with Northwestern University Center for Comparative Medicine (CCM) guidelines and Institutional Animal Care and Use Committee approved protocols (IACUC, protocol I500005132). Mice were euthanized via CO_2 asphyxiation followed by either cervical dislocation or decapitation.

1.2.3 Histology

1.2.3.1 *Tissue Processing*

Formalin-fixed brains (*see 1.2.2.6*) were serially sectioned in the coronal plane and processed in paraffin by the Northwestern Mouse Histology and Phenotyping Laboratory. Sections cut on a microtome (Leica) at 5-µm were used for histologic and immunohistochemical staining.

1.2.3.2 Hematoxylin and Eosin (H&E) Staining

H&E staining was performed on 5-µm sections of formalin-fixed, paraffin embedded (FFPE) tissue. Slides were deparaffinized in xylene and rehydrated using decreasingly concentrated alcohol solutions followed by water. Slides were stained with Hematoxylin then washed with water and Clarifier to remove excess Hematoxylin. Finally, slides were stained with 0.9% EosinY solution then dehydrated in increasingly concentrated alcohol solutions followed by xylene. Cytoseal (ThermoScientific) was immediately added to stained slides followed by a coverslip. Images were captured under the same light conditions on a BZ-X Series All-In-One Fluorescence Microscope (Keyence).

1.2.3.3 Immunohistochemistry (IHC)

IHC was performed on 5-µm sections of FFPE tissue with an automated IHC system (Ventana Medical Systems) with the following antibodies: anti-ATRX (abcam #ab188027, 1:100), anti-GFAP (Cell Signaling Technology #3670S, 1:50), anti-Ki67 (Cell Signaling Technology #12202, 1:400), anti-EMA (Roche Diagnostics, # 05878900001), and anti-Olig2 (Millipore #AB9610, 1:500). IHC was performed using a Vectastain Elite kit (Vector Laboratories #AK-5001) as described previously with the following antibodies: anti-PDGFRA (Cell Signaling Technology, #3174T, 1:1000), anti-pERK1/2 (ABclonal, #AP0472, 1:100), anti-Iba1/AIF-1 (Cell Signaling Technology, #17198T, 1:1500), and anti-H3.3G34R (abcam, #ab254402, 1:1000)[27]. Rabbit and mouse antibodies were diluted in 2% BSA solution. Images were captured under the same light conditions on a BZ-X Series All-In-One Fluorescence Microscope (Keyence).

1.2.3.4 Tumor Grading

Histologic sections from H3.3G34R and H3.3WT tumors from both ATRX WT and ATRX KO strains were evaluated for infiltration, astroglial or ependymal differentiation, grade, and necrosis. Tumor classification and grading was performed by a neuropathologist blinded to experimental conditions.

1.2.4 RNA-sequencing analysis

1.2.4.1 RNA Extraction and Library Preparation

Total RNA was isolated from snap frozen H3.3WT and H3.3G34R expressing tumors from ATRX WT and ATRX KO mice (n=5 per group) using the RNeasy kit (Qiagen #74104).

Sequencing was performed by the Northwestern University Sequencing Core Facility. The Illumina TruSeq Total RNA Library Preparation Kit (Illumina # 20020596) was used to prepare sequencing libraries including rRNA depletion.

1.2.4.2 Sequencing

Sequencing was performed using an lllumina HiSeq 4000 Sequencer (Illumina) to produce single-end 50-bp reads. Trim Galore (http://www.bioinformatics.babraham.ac.uk/projects/trim_galore/) was used to trim adapters and remove poor quality reads.

1.2.4.3 Differential gene expression

FASTQ files were aligned to the mm10 genome using RNA-STAR, and aligned reads were counted using HTSeq-count with Ensembl mm10 gtf[28,29]. HTSeq-count files were imported into R (https://www.r-project.org/) and differential expression analysis was performed with the DESeq2 package using default settings. DESeq2 normalized reads were imported into Gene set enrichment analysis (GSEA) and standard GSEA was run with the following parameters: permutations = 1000, permutation type = gene set, enrichment statistic = weighted, gene ranking metric = signal2noise, max size = 500, min size = 15, normalization mode = meandiv[30,31]. Box plots and volcano plots were generated using the ggplot2 and EnhancedVolcano R packages, respectively.

1.2.5 Quantitative Real-Time Polymerase Chain Reaction (RT-qPCR)

1.2.5.1 RNA Extraction and Reverse Transcription

Total RNA was isolated using the RNeasy kit (Qiagen #74104). cDNA was synthesized from total mRNA using the High-Capacity cDNA Reverse Transcription Kit (ThermoFisher Scientific #4368814). RT-qPCR EasyOligos (Sigma-Aldrich) primers were used for murine *Hoxa2*, *Hoxa3*, *Hoxa4*, *Hoxa5*, *Hoxa7*, *Nefm*, *Nelf* and *Stmn2* (Table 3). qPCR experiments were run using *Power* SYBR™ Green PCR Master Mix (ThermoFisher Scientific #4367659) on a QuantStudio 6 (ThermoFisher Scientific). Relative gene expression levels were generated using the ddCt method with murine *Taf1c* as the reference gene.

Table 3. Chapter 1 RT-qPCR primer sequences.

Primer Name	Primer Sequence (5' -> 3')
mHoxa2-FWD	CTCGGCCACAAAGAATCCCTG
mHoxa2-REV	TGTCTCTCGGTCAAATCCAGC
mHoxa3-FWD	CCGCGGTCTGAAGGCTAC
mHoxa3-REV	CCAGTGTCCAGGCACTCTTA
mHoxa4-FWD	TGCGATCTTCCAACACTGCC
mHoxa4-REV	AATGGGTGTGGAAGCACCAG
mHoxa5-FWD	AGCCACAAATCAAGCACACA
mHoxa5-REV	CGCTCACGGAACTATGATCTC
mHoxa6-FWD	ACCGACCGGAAGTACACAAG
mHoxa6-REV	GTCTGGTAGCGCGTGTAGGT
mHoxa7-FWD	GAAGCCAGTTTCCGCATCTA
mHoxa7-REV	CGTCAGGTAGCGGTTGAAAT
mNefm-FWD	GGTGTCCTGAAAGGTACAGGG
mNefm-REV	CTCCGTGTGTGTTGTGCCTA
mNefl-FWD	ATGACCTATGCAGGCTTTGCT
mNefl-REV	GGGCGCAATCAACTCTTTGT
mStmn2-FWD	GAAGCAGGGGACATTCCTGT
mStmn2-REV	AGTCATGTGGCGGAGTGTTT
mTaf1c-FWD	CGTCAGACGTCAACTTCAGC
mTaf1c-REV	GGTAAACCTTAGGCGTGGGC

1.2.6 Statistical Analysis

Statistical analysis was performed using GraphPad Prism. Survival curves were analyzed using Log-rank (Mantel-Cox) test. Tumor incidence, grade, necrosis, infiltration, and ependymal differentiation were analyzed using Fisher's exact test. IHC data was analyzed using two-tailed unpaired student t-tests. P values of less than 0.05 were considered significant for all analyses except DESeq2, in which adjusted p values (padj) < 0.05 were considered significant.

1.2.7 Human pHGG Gene Expression

The raw gene expression count matrix for human cells obtained from a patient harboring pHGG and stably transfected with wild type H3.3 (n=4) or H3.3 G34R mutant (n=3) were downloaded from NCBI GEO (GSE182068)[32]. The raw count matrix was imported into DESeq2 for normalization. Genes that satisfied the following criteria were selected for boxplots: (1) significant differential expression in our study and GSE182068 and (2) concordant fold change for G34R vs. H3.3 wild type. Additional human pHGG gene expression data were obtained from the PedcBioPortal (https://pedcbioportal.kidsfirstdrc.org/)[14] for 114 patients with available mRNA expression data and somatic mutation data. H3.3 mutation status was obtained for each patient: H3.3 G34R (n=10), H3.3 G34V (n=1), H3.3 K27M (n=38), and wild type H3.3 (n=65). Genes that satisfied the following criteria were selected for boxplots: (1) significant differential expression in our study and (2) concordant fold change for G34R vs. all. Boxplots were generated using the normalized log2 expression value (GSE182068) or the z-score (PedcBioPortal).

1.3 Results

1.3.1 H3.3G34R overexpression along with PDGF-A and p53 loss induces tumor formation independent of ATRX status

We infected the frontal cortex of ATRX WT (Ntv-a; $p53^{fl/fl}$) or ATRX KO (Ntv-a; $p53^{fl/fl}$; $Atrx^{fl/fl}$) mice with PDGF-A, Cre, and H3.3G34R or H3.3WT and monitored for signs and symptoms of tumor formation (Fig. 1A). H3.3G34R expression and reduced ATRX expression were confirmed via IHC (Fig. 1B-1C, Fig. 2A). IHC indicated increased expression of pERK1/2 and PDGFRA in tumor bearing mice, a hallmark of PDGFRA overactivation in H3.3G34R tumors (Fig. 1D)[33]. H&E and Ki67 stained brain tissue sections revealed clusters of proliferating cells or lesions in the brain consistent with tumor formation (Fig. 1E). H3.3G34 mutant pHGGs comprise a pathologically heterogenous subset of tumors; our model recapitulated several of these pathological features[14,34]. Most samples were high-grade with diffusely infiltrative and necrotic components and expression of Ki67 and GFAP was present in all groups (Table 4, Fig. 1E). It is important to note that Olig2 is highly expressed in most samples in our model despite not being expressed in H3.3G34R patient samples (Fig. 2B).

Table 4. Summary of histopathological analysis of representative tumor samples from all groups.

Categories	ATRX KO - H3.3G34R (n=14)	ATRX KO - H3.3WT (n=15)	ATRX WT - H3.3G34R (n=21)	ATRX WT - H3.3WT (n=21)
High/Intermediate Grade	86%	93%	100%	90%
Ependymal Differentiation	14%	33%	62%	67%
Diffuse Infiltration	64%	47%	33%	33%
Necrosis	29%	53%	48%	52%

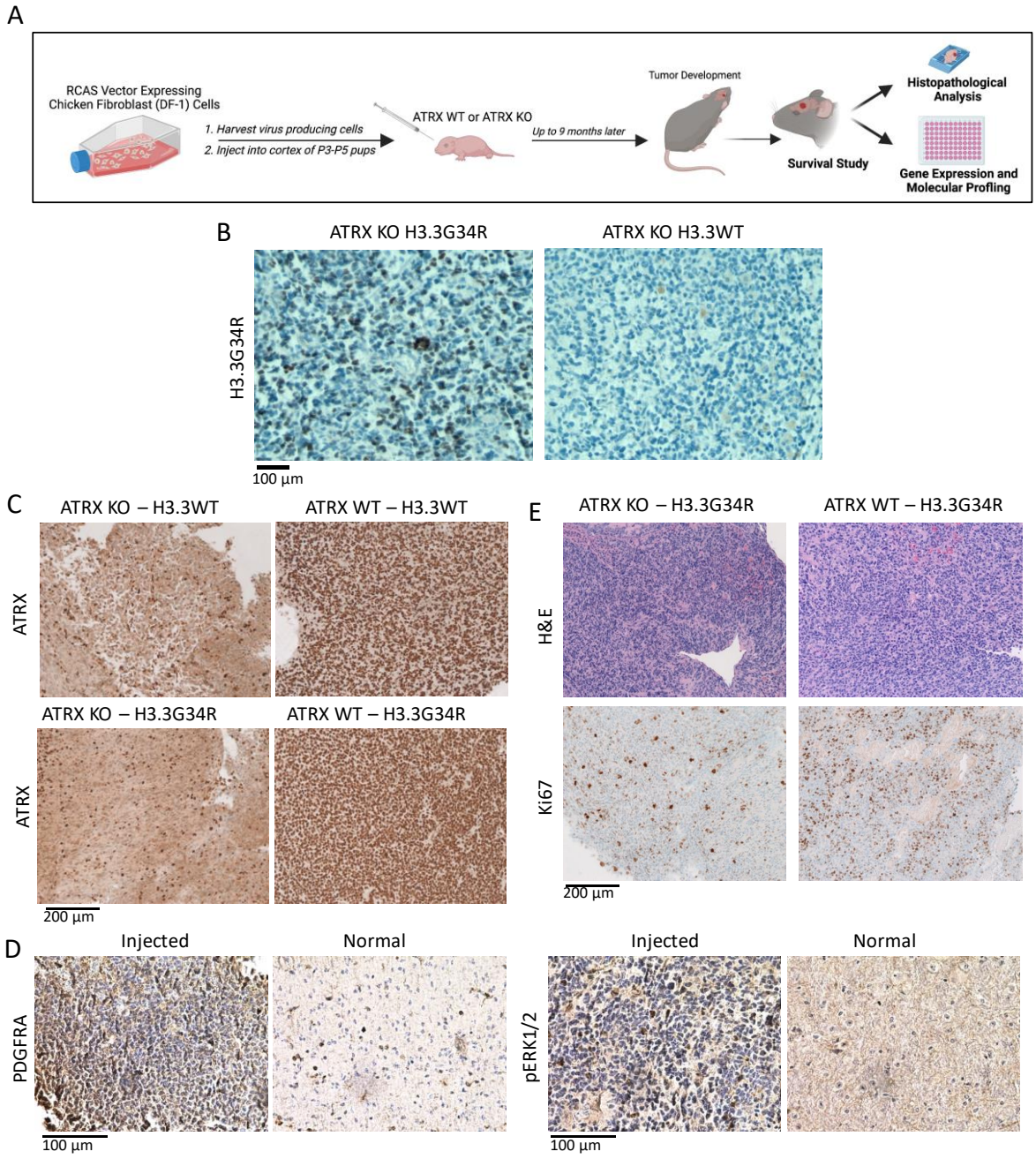

Figure 1. H3.3G34R overexpression along with PDGF-A and p53 loss induces tumor formation independent of ATRX. (A) Development of H3.3G34R and H3.3WT expressing tumors in both ATRX WT and ATRX KO mice using the RCAS/tv-a system workflow. (B) Representative H3.3G34R staining for H3.3G34R and H3.3WT expressing groups. (C) Representative staining for ATRX. (D) Confirmation of PDGFRA overexpression in injected RCAS/Ntv-a mice. (E) Representative H&E and Ki67 staining for H3.3G34R-GFP expressing groups. (D) Confirmation of PDGFRA activation with pERK1/2 as downstream kinases in infected RCAS/Ntv-a mice.

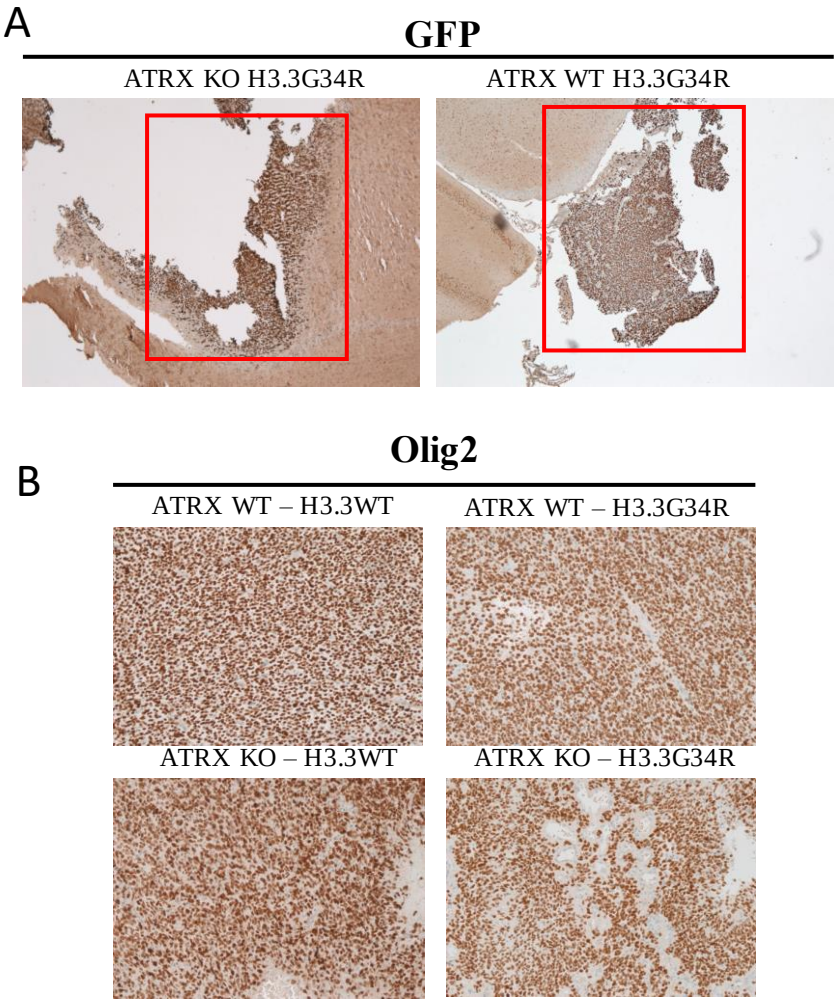

Figure 2. Representative staining of tumors with (A) GFP (5X) and (B) Olig2 (20X).

1.3.2 H3.3G34R overexpression does not significantly impact tumor latency or tumor incidence independent of ATRX status

H&E analysis of ATRX WT H3.3 WT, ATRX WT H3.3G34R, ATRX KO H3.3WT, and ATRX KO H3.3G34R brains revealed tumor incidence of 88%, 81%, 78% and 65%, respectively and there was no significant difference in tumor incidence between any groups (Fig.

3A). All groups displayed a trend of high-grade tumors; low grade tumors were only observed in H3.3WT injection groups however there was no significant difference in tumor grade between any groups (Fig. 4A, 3B). We observed no significant difference in overall survival between H3.3WT and H3.3G34R groups independent of ATRX status (Fig. 4B).

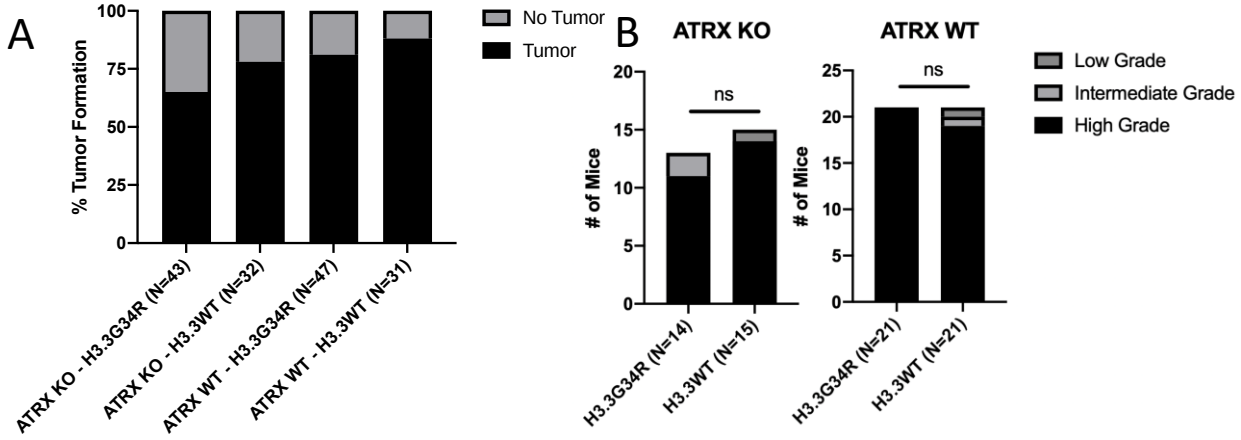

Figure 3. (A) Tumor incidence and (B) tumor grade for indicated injection groups.

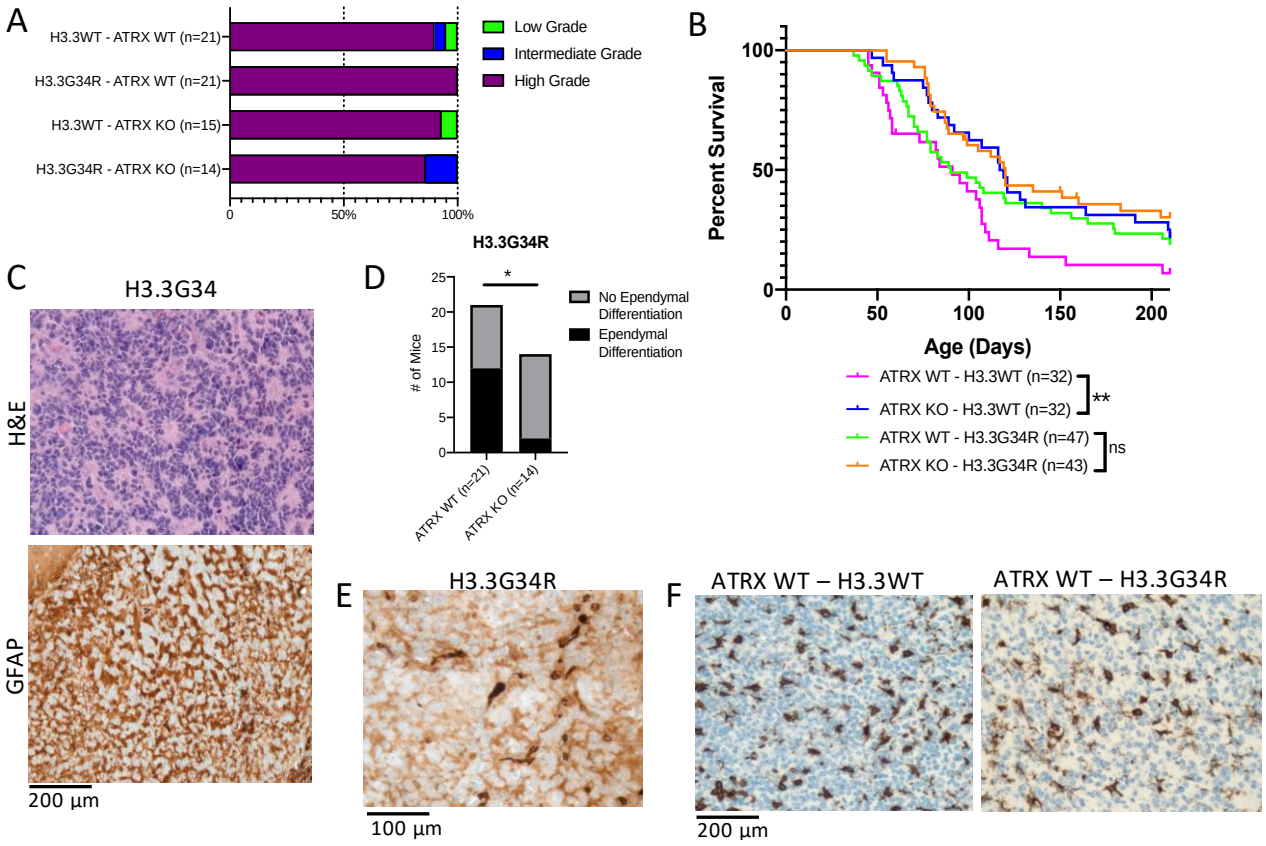

Figure 4. ATRX loss significantly increases tumor latency in the absence of H3.3G34R overexpression. (A) Tumor grades for all injection groups. (B) Kaplan-Meier survival curves for indicated injection groups. (C) Representative GFAP and H&E staining of ependymal differentiation in H3.3G34R-GFP overexpressing samples. (D) Ependymal differentiation incidence for H3.3G34R ATRX WT vs H3.3G34R ATRX KO (*$P < 0.05$, Fisher's exact test). (E) Representative EMA staining of H3.3G34R-GFP overexpressing samples. (F) Representative Iba1 staining of ATRX WT samples.

1.3.3 ATRX loss significantly increases tumor latency in the absence of H3.3G34R overexpression

ATRX loss significantly increased tumor latency only in the absence of H3.3G34R. (Fig. 4B). In H3.3G34R expressing mice, ATRX loss increased tumor latency from 90 days to 120 days ($p = 0.1$, Log-rank test) and in H3.3WT mice, ATRX loss increased tumor latency from 91 to 118 days ($p < 0.01$, Log-rank test) (Fig. 4B). When comparing H3.3G34R and H3.3WT expressing groups, we observed no difference in survival based on sex for with ATRX KO or ATRX WT animals. However, when comparing ATRX KO to ATRX WT animal survival, we found that females had significantly better survival than males for both H3.3WT expressing (HR = 0.32 [95% CI, 0.15 – 0.69], Cox regression analysis) and H3.3G34R (HR = 0.46 [95% CI, 0.23 – 0.92], Cox regression analysis) mice (Table 5). Several samples across all 4 groups contained ependymal differentiation as characterized by the presence of perivascular pseudo-rosettes (Table 4). Like H3.3G34-mutant pHGGs, ependymomas are largely GFAP positive and Olig2 negative and so in the absence of molecular profiles, histologic misinterpretation may occur (Figure 4C). Histopathological analysis revealed that ATRX KO H3.3G34R tumors had significantly lower incidence of ependymal differentiation in comparison to ATRX WT H3.3G34R tumors ($p< 0.05$, Fisher's exact test), indicating a potential role for ATRX in H3.3G34R tumors on perivascular pseudo-rosette formation (Fig. 4C-D). Dot-like immunoreactivity was also observed upon EMA staining (Fig. 4E). We did not observe any differences in Iba1 positive myeloid cells between any biological groups (Fig. 4F).

Table 5. Number of males and females per biological group.

Biological Group	Males	Females
ATRX WT – H3.3WT	17	15
ATRX WT – H3.3G34R	26	21
ATRX KO – H3.3WT	12	20
ATRX KO – H3.3G34R	18	25

1.3.4 ATRX loss in the context of H3.3G34R expression induces upregulation of *Hoxa* cluster genes

To elucidate potential mechanisms underlying ATRX mediated differences in overall survival, we extracted tissue from tumors of all 4 groups and performed RNA sequencing (RNA-Seq) analysis. Analysis of tumors from ATRX KO vs. ATRX WT mice in H3.3G34R and H3.3WT injection groups indicated significant differential expression of 113 genes and 74 genes, respectively (Table 6). Analysis of H3.3G34R vs H3.3WT expressing tumors in ATRX KO and ATRX WT mice indicated significant differential expression of only 34 genes and 12 genes, respectively (Table 6). Overall, ATRX status has a greater effect on the tumor transcriptome than the presence of H3.3G34R (Fig. 5A, 6B, 7). We next performed GSEA analysis to compare the transcriptomes of H3.3WT and H3.3G34R tumors in our ATRX WT and ATRX KO models. ATRX KO H3.3G34R tumors were more enriched for genes associated with 'signal metabolic shifts', decreased enrichment of genes associated with 'interaction with the extracellular matrix' and 'invasiveness' compared to ATRX WT H3.3G34R tumors and ATRX KO H3.3WT tumors displayed increased enrichment of genes associated with 'immune/inflammatory signaling' and 'Notch signaling' as well as decreased enrichment of genes associated with 'cell proliferation'

and 'neuronal markers' compared to ATRX WT H3.3WT tumors (Fig. 8). Differential expression analysis also revealed upregulation of several *Hoxa* cluster genes (*Hoxa5, Hoxa3, Hoxa7, Hoxa4, and Hoxa2*) and the long-noncoding RNA *Hoxaas2* at high levels in ATRX KO H3.3G34R tumors compared to ATRX WT H3.3G34R tumors (Fig. 5A-B). The HOXA gene cluster is a critical regulator of both CNS and osteoblast development[35-37]. RT-qPCR confirmed significant upregulation of *Hoxa2, Hoxa3, Hoxa5* and *Hoxa7* in ATRX KO H3.3G34R tumors relative to ATRX WT H3.3G34R tumors (Fig. 5C). Interestingly, significant differential expression of *Hoxa* cluster genes was not found in analysis of ATRX KO H3.3WT tumors relative to ATRX WT H3.3WT tumors or in analysis of ATRX KO H3.3G34R tumors relative to ATRX KO H3.3WT tumors (Fig. 6B, 7).

Table 6. Number of differentially expressed genes for each group (n=5 per group).

Comparison	All significantly differentially expressed genes	Upregulated genes	Downregulated genes
ATRX WT – H3.3G34R vs H3.3WT	12	7	5
ATRX KO – H3.3G34R vs H3.3WT	34	29	5
H3.3WT – ATRX KO vs ATRX WT	74	35	39
H3.3G34R – ATRX KO vs ATRX WT	113	78	35

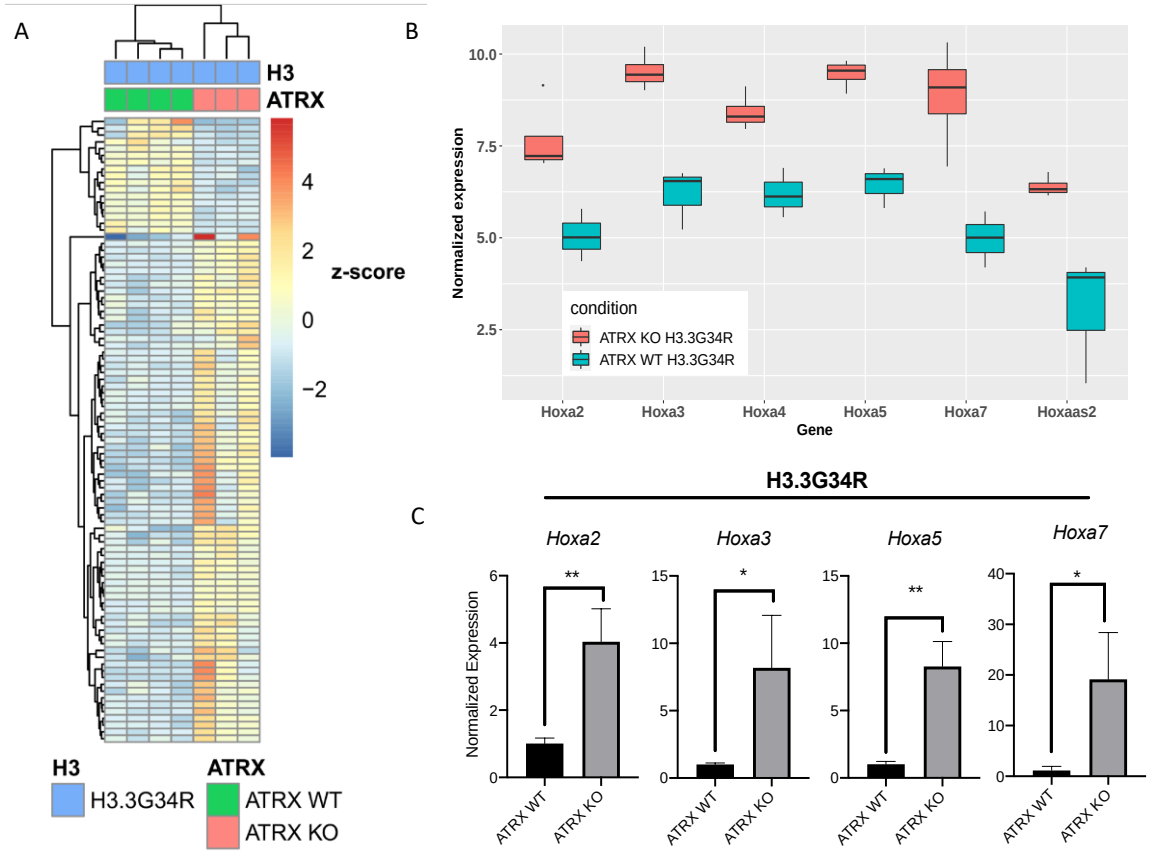

Figure 5. ATRX loss in the context of H3.3G34R induces expression of *Hoxa* genes. (A) Unsupervised hierarchical clustering of differentially regulated genes (padj < 0.05) in H3.3G34R ATRX WT vs H3.3G34R ATRX KO tumors (n = 5 per group). (B) Differential expression of *Hoxa* genes (padj < 0.05) H3.3G34R ATRX WT vs H3.3G34R ATRX KO tumors (n = 5 per group). (C) RT-qPCR validation of *Hoxa2*, *Hoxa3*, *Hoxa5*, and *Hoxa7* upregulation in H3.3G34R ATRX KO vs H3.3G34R ATRX WT tumors (n = 3 per group) (**P* < 0.05, ***P* < 0.01, two-tailed unpaired t-test).

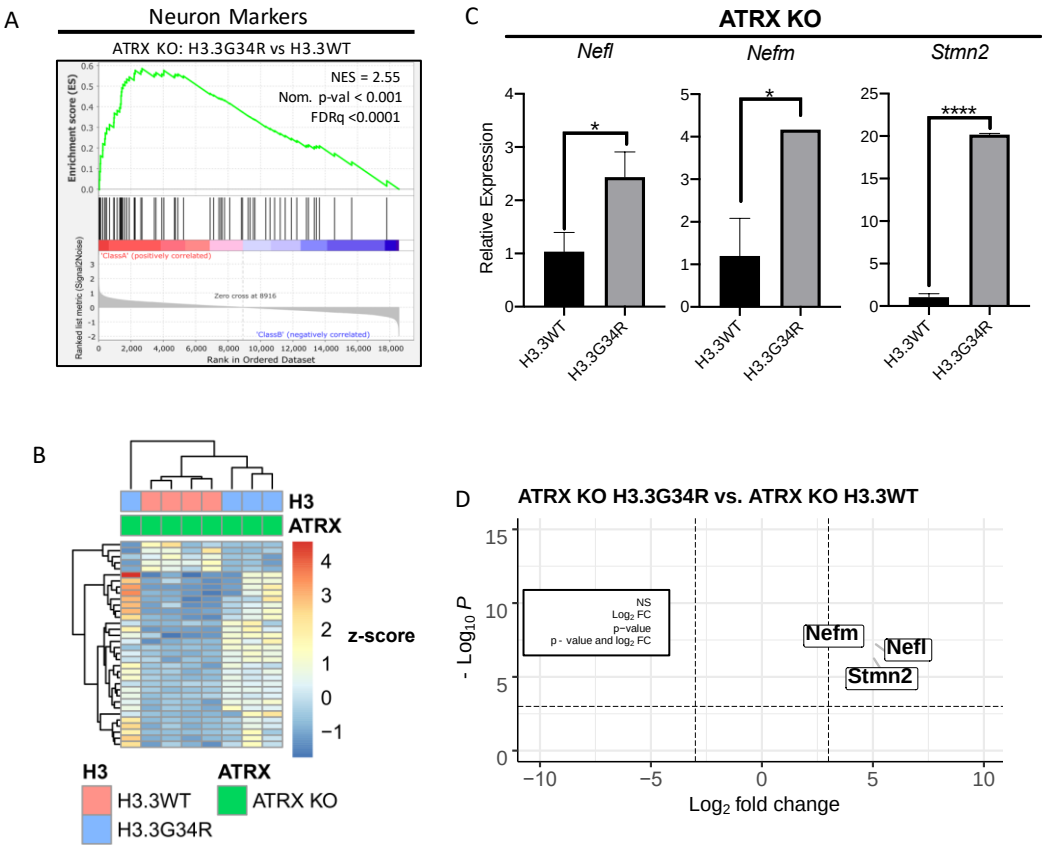

Figure 6. H3.3G34R expression in the context of ATRX loss promotes neuronal lineage. (A) GSEA plot (FDR < 0.001) of neuron marker activation in H3.3G34R ATRX KO vs H3.3WT ATRX KO tumors (n = 5 per group). (B) Unsupervised hierarchical clustering of differentially regulated genes (padj < 0.05) in H3.3G34R ATRX KO vs H3.3WT ATRX KO tumors (n = 5 per group). (C) RT-qPCR validation of *Nefl, Nefm* and *Stmn2* upregulation in H3.3G34R ATRX KO vs ATRX KO H3.3WT tumors (n = 3 per group)(*P < 0.05, ****P < 0.0001, two-tailed unpaired t-test). (D) Volcano plot highlighting *Stmn2, Nefl,* and *Nefm* upregulation (padj < 0.05) in H3.3G34R ATRX KO vs H3.3WT ATRX KO tumors (n = 5 per group).

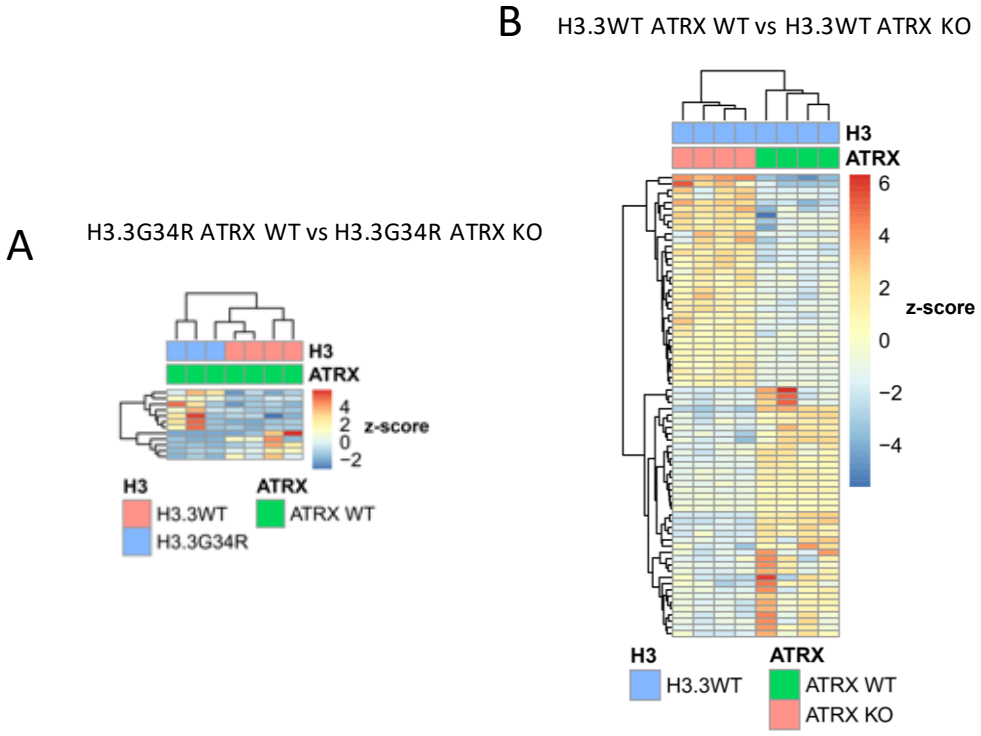

Figure. 7. Unsupervised hierarchical clustering of differentially regulated genes (padj < 0.05) in (A) H3.3G34R ATRX WT vs H3.3G34R ATRX WT tumors and (B) H3.3WT ATRX WT vs H3.3WT ATRX WT tumors(n = 5 per group).

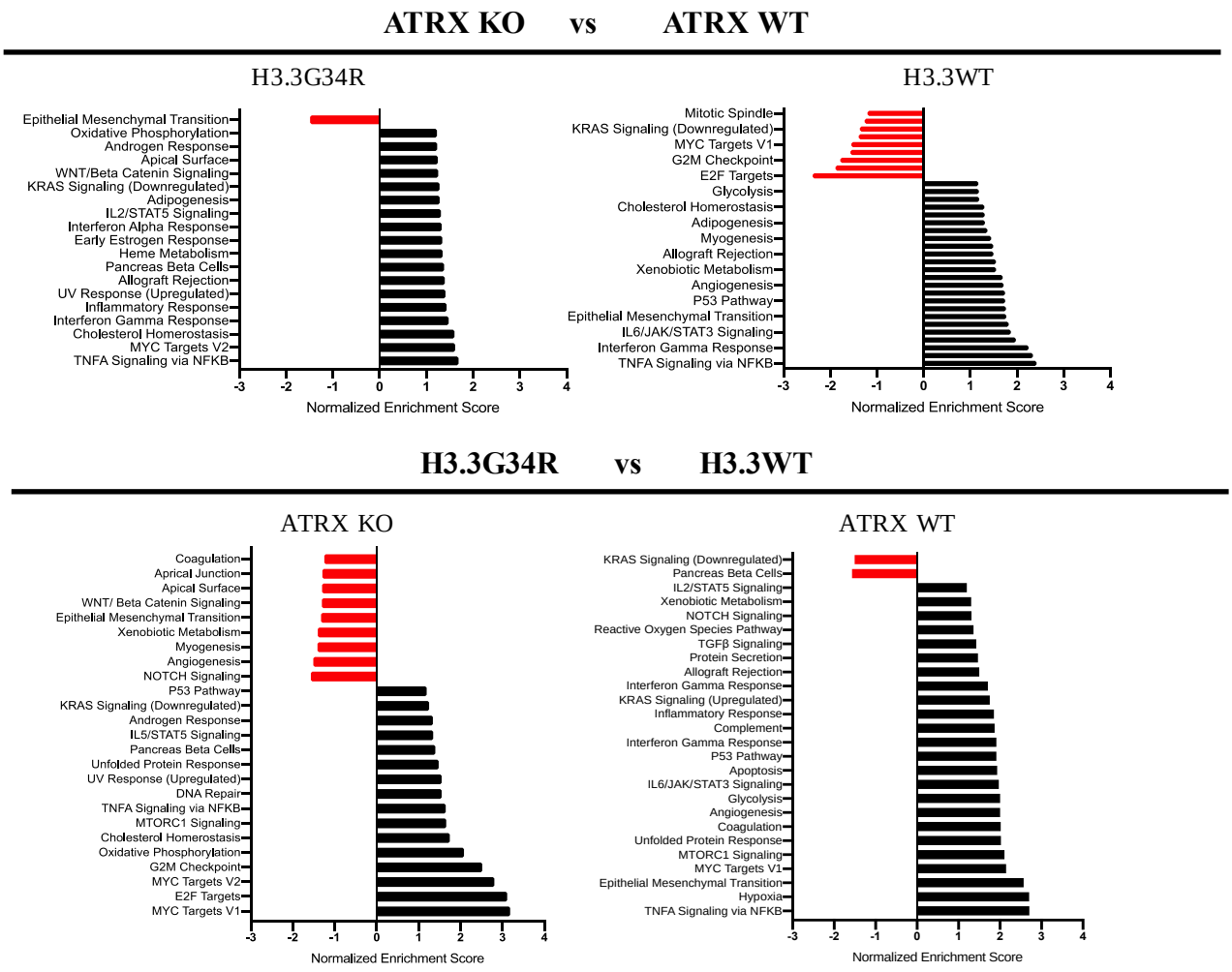

Figure 8. GSEA results summary.

1.3.5 H3.3G34R expression promotes neuronal lineage in the context of ATRX loss

GSEA analysis indicated that ATRX KO H3.3G34R tumors have increased expression of genes associated with 'cell proliferation' and 'metabolism' and decreased expression of genes associated with 'interaction with the extracellular matrix' compared to ATRX KO H3.3WT tumors (Fig. 8). Despite H3.3G34R expression having relatively little effect on the transcriptome of ATRX KO samples, GSEA analysis revealed enrichment of neuronal markers in ATRX KO H3.3G34R vs ATRX KO H3.3WT tumors (Fig. 6A). Differential expression data and RT-qPCR confirmed that the neuronal differentiation marker *Stmn2* was significantly upregulated in ATRX KO H3.3G34R vs ATRX KO H3.3WT tumors (Fig. 6B-C). Transcriptomic data indicates that *Stmn2* may be upregulated in ATRX KO H3.3G34R samples vs ATRX WT H3.3G34R samples however this difference does not quite reach statistical significance (Fig. 6D). *Stmn2* was not upregulated in any other comparison, indicating that H3.3G34R promotes expression of the neural differentiation marker *Stmn2* in the context of ATRX loss (Fig. 6B-D). Transcriptomic data indicated that the neurofilament polypeptides, *Nefm* and *Nefl* were significantly upregulated in ATRX KO H3.3G34R samples vs ATRX KO H3.3WT samples and this was confirmed with RT-qPCR (Fig. 6B-D). *Nefm* and *Nefl* were not significantly differentially expressed in any other comparison.

1.3.6 Differential expression data from a murine model of H3.3G34R glioma demonstrates relevance to the human disease

To confirm biological relevance of our novel murine model of H3.3G34R pHGG, we explored whether the 34 genes that were significant differentially expressed between H3.3G34R; ATRX KO and H3.3WT; ATRX KO and the 113 genes that were significantly differentially

expressed between H3.3G34R ATRX KO vs. ATRX WT were also upregulated in human samples with H3.3G34R. We used one published dataset using an *in vitro* model using a human cell line, SJ-GBM2, derived from a tumor that developed in a child with a high-grade glioma arising in the cerebral cortex, harboring TP53- and ATRX-inactivating mutations, and stably transfected with H3.3WT or H3.3G34R, and a second dataset of pediatric high-grade glioma samples from the PedcBioPortal that were annotated for H3 status (K27M vs. G34R/V vs. WT)[14,32]. Out of 34 genes that were significant differentially expressed between H3.3G34R; ATRX KO and H3.3WT; ATRX KO murine tumors in our study, we observed two genes that were significantly differentially expressed with concordant fold change in the ST-GBM2-H3.3G34R model relative to ST-GBM2-H3.3WT control:COL12A1, and NEFL (Fig. 6B, 9A, 10)[32]. Out of the 113 genes that were significantly differentially expressed between H3.3G34R ATRX KO vs. ATRX WT, 13 genes were significantly differentially expressed with concordant fold change in the ST-GBM2-H3.3G34R model relative to ST-GBM2-H3,3WT control: ANPEP, COL6A2, DCT, DPYD, EMC9, HOXA5, HOXA7, LMX1B, MMP3, NCS1, TMEM151A, TMEM130, and VSTM2L (Fig. 6B, 9B, 10)[32]. With regards to the second dataset in PedcBioPortal, none of the 34 genes that were significantly differentially expressed between H3.3G34R; ATRX KO and H3.3WT; ATRX KO murine tumors in our study were concordantly overexpressed in the human G34R mutant tumors relative to the control tumors. Out of the 113 genes that were significantly differentially expressed H3.3G34R ATRX KO vs. H3.3G34R ATRX WT, five genes namely, COL5A1, COL6A2, KHDC8A, PDGFD, and PGM5 were concordantly overexpressed in G34R mutant human tumors relative to controls. (Fig. 5A, 9C)[14]. This comparative analysis identified genes for further functional validation in the context of

G34R mutant glioma and supports our observations in the murine model, namely that ATRX loss contributes to the transcriptomal effects of H3.3G34R.

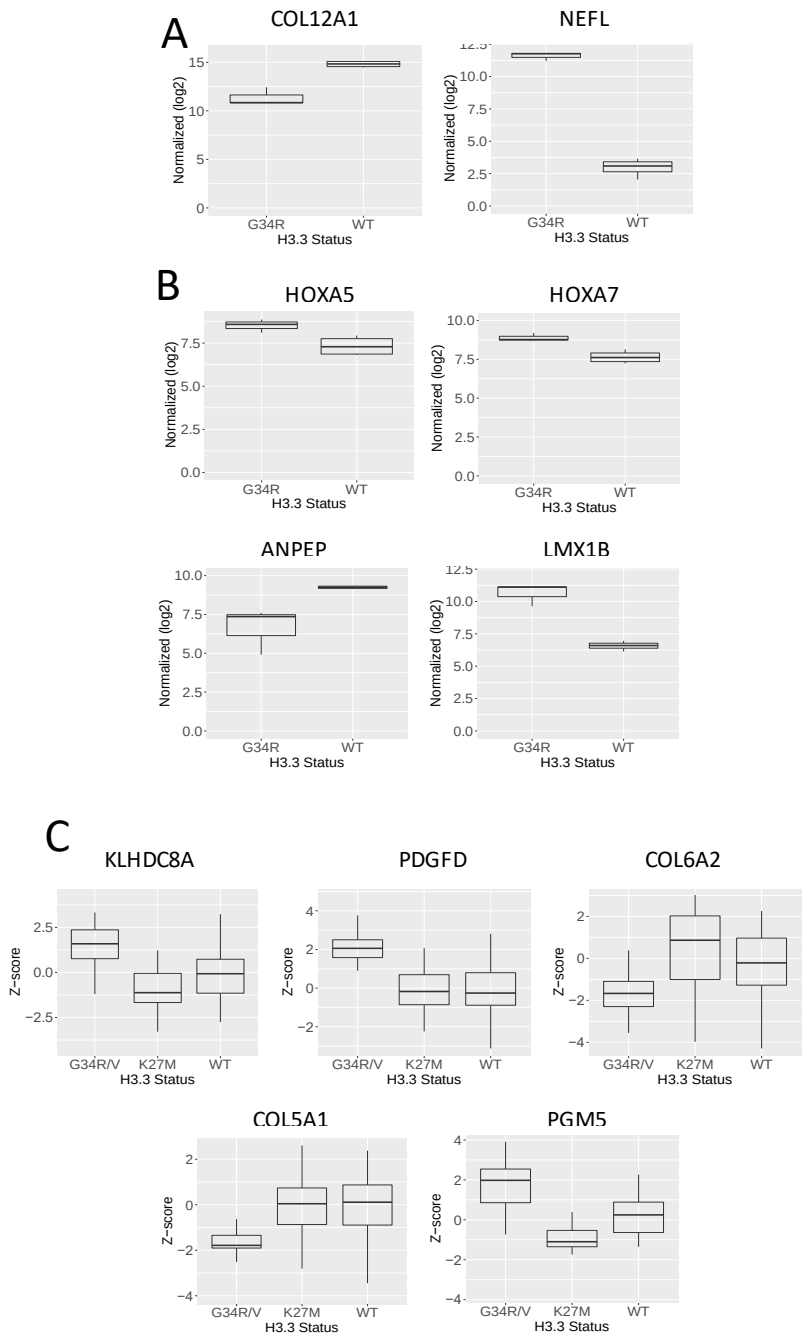

Figure 9. Differential expression data from a murine model of H3.3G34R glioma has similarities to human disease. (A). Box plots for genes which were significantly differentially expressed in the G34R; ATRX KO vs. H3.3WT; ATRX KO murine tumors with concordant fold change in the ST-GBM2-H3.3G34R model relative to ST-GBM2-H3.3WT control (padj < 0.1). (B) Box plots for genes which were significantly differentially expressed in the ATRX KO; G34R vs. ATRX WT; G34R murine tumors with concordant fold change in the ST-GBM2-H3.3G34R model relative to ST-GBM2-H3.3WT control (padj < 0.1) or (C) human G34R mutant tumors relative to K27M mutant tumors and H3WT tumors using the cBioPortal database. (padj < 0.1).

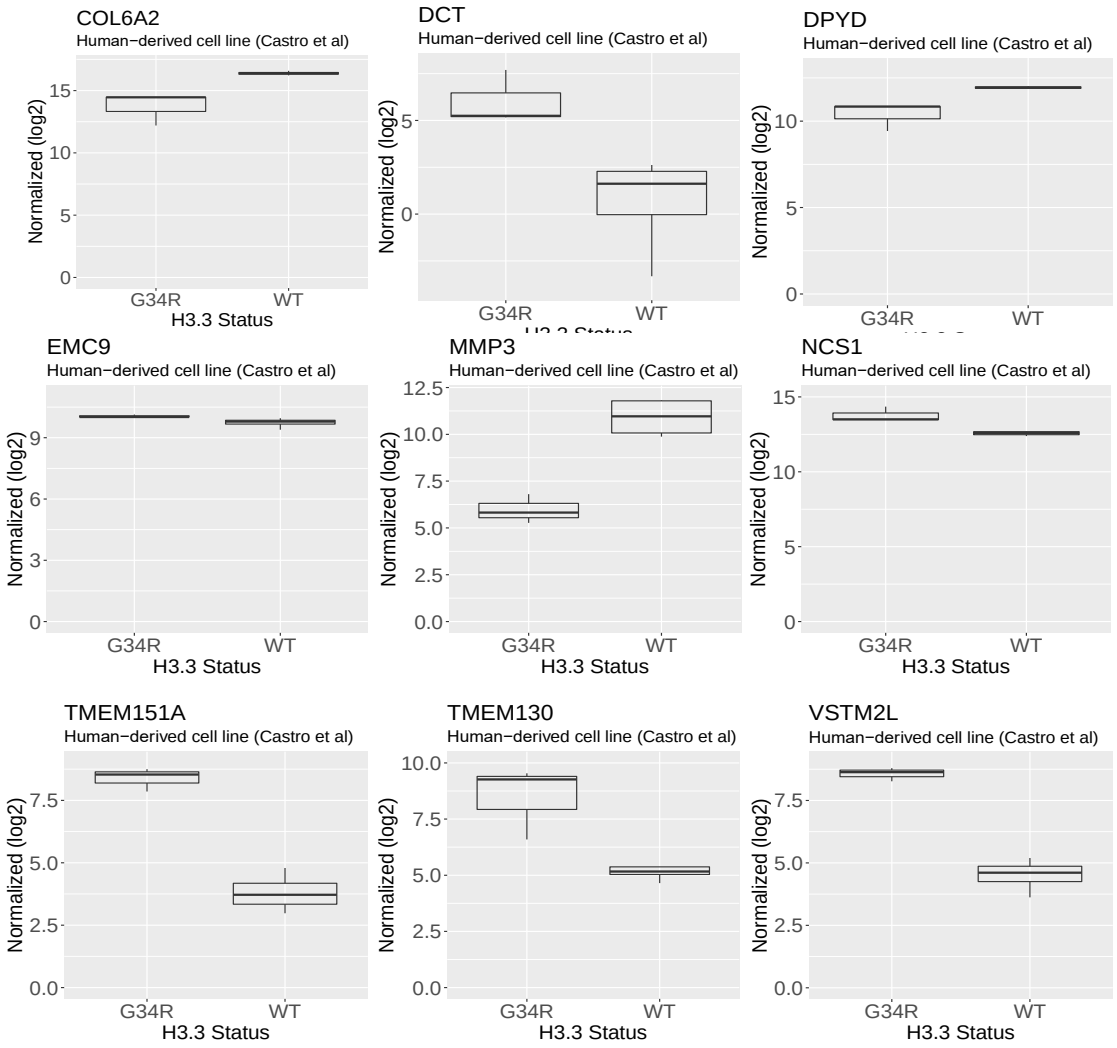

Figure 10. Remaining genes which had a significant concordant fold change in murine tumors and in the ST-GBM2-H3.3G34R model relative to ST-GBM2-H3.3WT control.

1.4 Discussion

Attempts to understand the effects of the H3.3G34R mutation on tumor initiation and progression have increased in the last several years[33,38,39]. Following the identification of recurrent H3.3G34 missense mutations in one of the two genes that encode Histone H3.3 (*H3F3A*), it was postulated that the presence of H3.3G34 mutants decreases SETD2 mediated H3K36 di- and tri- methylation *in cis* however the full mechanism of H3.3G34 mutations on pHGG initiation and progression has not been elucidated[15,16,18,40]. In contrast to the more well-studied H3.3K27M mutation, H3.3G34 pHGGs are a heterogenous mixture of tumors, making it difficult to develop a robust model. In general, there have been few published H3.3G34R models [16,33,38,39,41]. The first published H3.3G34R mutant glioma model was a patient derived xenograft model (PDX)[13]. Several model systems have been proposed in the last several years and it is only recently that two GEMMs of H3.3G34 gliomas has been developed[32,33]. In one GEMM model, introduction of H3G34R and *TP53* loss via *in utero* electroporation (IUE) into neural progenitor cells (NPCs) of mouse forebrains did not produce any tumors[11]. In a subsequent study with the same IUE method however, they included PDGFRA overexpression, ATRX knockdown, and *TP53* knockout and the resultant mice developed cortical tumors[33]. The same study reported that the majority of human H3.3G34R tumors carry activating *PDGFRA* mutations and that these mutations have high selection pressure during recurrence[33]. Recent work has suggested the H3.3G34R mutation may have a role in tumor initiation but is dispensable for tumor maintenance, further highlighting the need for GEMMs [16,33,38]. In the second GEMM model using Sleeping Beauty Transposase system, H3.3G34R is overexpressed with shRNAs against ATRX and p53 together with a mutant NRAS. The authors apply the

model to demonstrate that H3.3G34R impair DNA repair and promote cGAS/STING mediated immune response[32].

We combined H3.3G34R or H3.3WT overexpression and PDGF-A overexpression with *TP53* and ATRX loss (ATRX KO) in immunocompetent mice to develop a novel GEMM of H3.3G34R pHGG. While the cell-of-origin for H3.3G34-mutant pHGGs has not been definitively determined, it was previously shown that human fetal NSC cultures recapitulate transcriptional signatures of pHGGs indicating a nestin-positive neural stem cell is a candidate cell of origin for H3.3G34R pHGGs[33]. Accordingly, we utilized the RCAS/tv-a system to express the H3.3G34R mutation in nestin- expressing progenitor cells of the neonatal murine frontal cortex to model H3.3G34R pHGG *in vivo* and probe potential oncogenic mechanisms of H3.3G34R. In our ATRX KO model, we observed no significant differences in survival between mice overexpressing H3.3G34R vs mice overexpressing H3.3WT; this finding is consistent with earlier work. H3.3G34 mutant gliomas exhibit a trend of increased tumor latency compared to H3.3WT tumors however this trend typically does not reach statistical significance[42]. The majority of H3.3G34 murine models have also reported no significant difference in survival as a result of H3.3G34 expression[13,16,33,38,39,41]. Given the developmental nature of H3.3G34 mutant pHGG, it was suggested that postnatal expression of H3.3G34 mutations in various model systems did not produce meaningful results; however a model in which the G34R/V mutants were introduced into mice embryos mid-gestation via IUE also reported no significant differences in tumor latency or overall survival between groups expressing H3.3G34R/V vs those expressing H3.3WT[11].

We next chose to focus on the role of ATRX loss in H3.3G34 mutant pHGGs. While *TP53* mutations occur in the majority of H3K27M and H3.3G34R/V pHGGs, ATRX mutations

are much more prevalent in H3.3G34 mutant tumors. This result was not entirely surprising as ATRX loss has been associated with better prognosis in other brain tumors[43]. More surprising was the effect the H3.3G34R mutation appeared to have alongside ATRX loss; in the absence of the H3.3G34R mutation, ATRX loss leads to a significant increase in survival and tumor latency, however this effect was not significant when H3.3G34R mutation was expressed. To further elucidate the effect of ATRX loss on H3.3G34R pHGGs, we probed for transcriptomic changes. Overall, we observed that ATRX status had a greater effect on the transcriptome than H3.3G34R presence. Several *Hoxa* genes were upregulated in ATRX KO H3.3G34R mice relative to ATRX WT H3.3G34R mice and not in any other group. RT-qPCR confirmed significant upregulation of murine *Hoxa2*, *Hoxa3*, *Hoxa7*, and *Hoxa5* in ATRX KO H3.3G34R tumors relative to ATRX WT H3.3G34R tumors. Differential gene expression analysis revealed an upregulation of *Hoxa2*, *Hoxa4*, and *Hoxa5* in ATRX KO H3.3G34R relative to ATRX KO H3.3WT tumors though the difference did not quite reach statistical significance. The HOX regulatory genes encode transcription factors and are critical regulators of embryonic development of several organs and cell types includes the CNS and osteoblasts[35,36]. In most vertebrates, the 39 HOX genes are split into 4 groups or "clusters" including HOXA, HOXB, HOXC and HOXD. In cancer, aberrant expression has been reported for more than half the HOX genes. In the brain, the HOXA cluster has been particularly relevant and is upregulated across various tumor types[35]. The HOXA cluster is located on chromosome 7, which is commonly amplified in glioblastoma (GBM) though HOXA upregulation has been reported in copy neutral tumors[37,44-46]. H3.3G34R pHGGs are not described as having chromosome 7 copy number amplifications[47]. We put forth that the enrichment of several *Hoxa* genes is the result of a concerted effort of both ATRX loss and the H3.3G34R mutation. A plausible mechanistic explanation for the synergy is that ATRX is the

histone chaperone for H3.3 incorporation onto heterochromatin (with DAXX), or repetitive elements of the genome, such as telomeres while HIRA is the histone chaperone for H3.3 onto euchromatin. It may be that in mice, which harbor longer telomeres, the transcriptomal effects of H3.3G34R are more pronounced when ATRX is deleted, as ATRX deletion, by default, may result in more H3.3G34R becoming incorporated onto euchromatin via HIRA[6,7,48]. Additional studies are required to determine if this potential mechanism is the true reason for the synergy.

While H3K27M pHGGs correlate with mid- to late gestation embryonic expression patterns, transcriptional signatures of H3.3G34R pHGGs typically correlate with early embryonic development[40]. We observed the same trend in our system. We found that H3.3G34R expression upregulates the early neuronal developmental markers *Stmn2, Nefm,* and *Nefl,* but only in the presence of ATRX loss. *Nefm* and *Nefl* are found in the cytoplasm of neurons and are critical components for the development of the neuronal cytoskeleton. Co-expression of *Nefm* and *Nefl* is typically associated with neuron committed progenitors while expression of *Nefm*, *Nefl,* and *Nefh* (the neurofilament triplet) is associated with later stages of neuronal development[49]. *Nefm* and *Nefl* are also commonly used as markers for axonal damage[49]. Given the multiple functions of neurofilament proteins, further work is needed to determine the exact causes of *Nefm* and *Nefl* aberrant expression in ATRX KO H3.3G34R tumor samples as well as resulting phenotypes.

G34R tumors can sometimes present histologically as primitive neuroectodermal tumors (PNET), which are normally comprised of cells observed during early neural development[50]. Single-cell classification of a cohort of adult and pediatric human GBM samples revealed upregulation of *Stmn2* in a molecularly defined cell cluster of what is referred to as NPC-like cells[51]. While *Stmn2* plays an important role in neuronal growth, it is also important during early

osteogenesis and was recently reported to be differentially regulated in GCTB patient derived H3.3G34W stromal cells[52,53]. This data point provides a potential mechanistic link between H3.3G34R/V pHGG and H3.3G34W/L GCTB/osteosarcoma. Further study is needed to clarify the role of *Stmn2* in both these malignancies.

Comparison of the 34 significantly differentially expressed genes that were significantly upregulated by H3.3G34R relative to H3.3WT in the ATRX KO model to an isogenic human pediatric HGG cell-line that stably expressed H3.3G34R or H3.3WT unraveled 2 genes with concordant overexpression: COL12A1, and NEFL.[32] COL12A1 has not been studied extensively in gliomas but has been implicated in metastasis in breast cancer[54].

Two potential limitations of our study are (1) loss of *TP53* and/or ATRX as well as expression of H3.3G34R and PDGF-A was induced in mice 3-5 days postnatally and it is unclear when during neural development the H3.3G34 mutation is acquired and (2) Olig2 expression is commonly present in our samples however human pHGG tumor samples are overwhelmingly Olig2 negative. It was recently proposed that H3.3G34 mutant pHGGs originate in a subset of interneuron progenitors and that the mutated onco-histone somehow keeps its cell of origin in an undifferentiated state.[33] Oligodendrocyte precursor cells (OPCs) give rise to mature oligodendrocytes (OLs) and DNA methylation data has indicated a lack of activity in genes required for OPC differentiation into OLs in G34 mutant tumors[33]. Potential mechanisms in which H3.3G34 mutations influence preferential differentiations into OLs versus mature interneurons (known as the neuron-glial switch) have not been explored. An interneuron progenitor population persists in the subventricular zone (SVZ) into adulthood therefore, if H3.3G34 mutant pHGGs truly originate in interneuron progenitors, this does not preclude postnatal development of these tumors. Additionally, we were unable to assess the effect of

ATRX loss on ALT in our ATRX KO samples. While it is known that ATRX loss is not sufficient to induce ALT, the ALT status of this model warrants further study. Our model did in fact recapitulate several histopathological and molecular features of H3.3G34R mutant gliomas despite induction in P3-P5 mouse pups. In summary, our work provides biologically relevant, immunocompetent GEMMs of H3.3G34R pHGG both with and without ATRX loss and highlights the cooperation between H3.3G34R mutations and ATRX loss on *Hoxa* gene activation and neuronal lineage.

1.5 Future Directions

Several open questions remain in regards to the transcriptomic and genomic effects of H3.3G34R expression and/or ATRX LoF in pHGG. Our RNA sequencing analysis provides a substantial list of potential genes involved in G34R pathogenesis but validation followed by focused, functional studies are required to identify true genetic drivers. Furthermore, while our bulk RNA sequencing gives an important snapshot of changes in the global transcriptome, single-cell genomic assays such as single cell RNA sequencing or single-cell assay for transposase-accessible chromatin sequencing (ATAC-seq) could provide vital information on specific transcriptomic and genomic changes in H3.3G34R expressing and/or ATRX loss-of-function cells[55]. It is also unclear how ATRX LoF is effecting H3.3 deposition in either H3.3G34R or H3.3WT glioma cells. Genomic assays such as chromatin immunoprecipitation sequencing (ChIP-Seq) or cleavage under targets and release using nuclease (CUT&RUN) would be ideal methods to elucidate the effects of ATRX LoF on histone deposition[56].

As previously stated, due to technical limitations we were unable to assess whether our samples presented with an ALT phenotype. A recent paper showed that the computational tool *TelomereHunter* can accurately estimate telomere content from sequencing data, representing an alternative to the more technically challenging C-Circle assay[57-59]. Telomere fluorescence in situ hybridization (Telo-FISH) is another wet-lab option to visualize ALT in tumor tissue in cases where sequencing data is not available[60]. Additional characterization of the effects of H3.3G34R and ATRX loss of function on hallmarks of carcinogenesis such as cell proliferation, apoptosis, metabolism, metastasis, and angiogenesis are also required in our novel GEMMs[61].

1.6 Conclusion

Biologically relevant animal model systems are critical for the discovery of molecular mechanisms of carcinogenesis. The RCAS/tv-a system provides a fast, high-throughput method to probe region-specific genetic perturbations in an immunocompetent mouse model. Utilizing the RCAS/tv-a system, we have developed several models of pHGGs which incorporate the H3.3G34R mutation either in the presence or absence of ATRX. Our model recapitulates several important molecular and histopathological features of human H3.3G34R pHGGs such as promotion of neuronal lineage and diffusely infiltrating components with perivascular pseudo-rosettes. Our work reveals the critical role ATRX status plays in H3.3G34R mediated gliomagenesis.

CHAPTER 2: H3.3G34R cooperates with ATRX loss in upregulation of the Notch pathway in murine models of pediatric glioma

2.1 Introduction

2.1.1 The Notch Signaling Pathway

The Notch signaling pathway is a well-characterized and critical regulator of embryonic development as well as various adult processes[62]. Aberrations in Notch signaling have been associated with errors in tissue homeostasis, adult stem cell maintenance and several hereditary diseases[62,63]. Notch signaling is vital across different cell types and processes; mutations in Notch receptors or ligands have been implicated in cancer pathogenesis of the skin, head and neck, lungs and brain[64].

2.1.1.1 Mammalian Notch Signaling

Canonically, Notch signaling mediates close range cell-cell interactions through a mechanism of ligand-dependent receptor proteolysis[65]. In mammals, there are 4 Notch receptors (NOTCH1, NOTCH2, NOTCH3, NOTCH4) and several classes of canonical Notch ligands including Delta/Serrate/LAG-2 (DSL)/ Delta and OSM-11-like proteins (DOS) (Dll1, Jagged1 and Jagged 2), DSL only (Dll3 and Dll4) and DOS only (DLK-1, DLK-2/EGFL9)[66]. During canonical mammalian Notch signaling, a Notch ligand will bind the membrane-bound Notch receptor, inducing Notch pathway activation via stepwise receptor proteolysis as determined by the gamma-secretase enzyme complex[66]. In addition to cell-cell interactions (*trans* activation), Notch activation can also occur in *cis*[67]. Canonical Notch signaling has been extensively studied however more recently, non-canonical roles for Notch have been reported in oncogenesis, immunity, and differentiation[68].

2.1.1.2 Notch Signaling in Oncogenesis

Roles for the Notch pathway have been identified in various malignancies, the first of which was T-cell acute lymphoblastic leukemia[67,69]. Broadly, Notch signaling is a well-documented regulator of cell processes that are also hallmarks of carcinogenesis including cell proliferation, apoptosis and stemness[64]. Notch is also required for programs that support cancer progression such as metabolism and transcription. The Notch pathway has been repeatedly shown to be aberrantly activated in glioma[10]. Downstream effects of aberrant Notch signaling in glioma include reduction of apoptosis, increased cell proliferation, and support for poorly differentiated tumors[70]. Notch signaling also represents a potential therapeutic target; it was reported that inhibition of Notch in glioblastoma cell lines with gamma-secretase inhibitors reduced cell proliferation and induced apoptosis[70,71].

2.1.1.3 Effects of Notch on Cancer Cell Stemness

As Notch signaling has a well-documented and critical role in central nervous system (CNS) development via regulation of neural stem cells (NSC), it is not surprising that Notch signaling is also extremely active in glioma stem cells (GSCs), the precursor cells of glioma[72-74]. When Notch signaling is low, NSCs proliferate and undergo differentiation; similarly, blocking interactions between HIF-1α and NICD and resultant inhibition of Notch signaling abrogates GSC maintenance in glioblastoma cell lines[75]. Furthermore, Notch2 expression levels have been associated with the glioma stemness markers nestin and SOX2[70]. Taken together, there is sufficient rationale for a mechanism of Notch supported stemness in glioma.

2.1.1.4 DLL3

The Notch ligand *DLL3* is particularly important for somitogenesis. *DLL3* is highly expressed during fetal brain development and promotes neurogenesis. Very recently, it was reported that *DLL3* expression was upregulated in a cohort of adult isocitrate dehydrogenase (IDH) wildtype (WT) gliomas and significantly associated with favorable outcomes. In the previous chapter, we conducted RNA-Sequencing which reported significant upregulation of *Dll3* in ATRX knockout (KO) and H3.3G34R samples compared to ATRX WT and H3.3WT samples, in genetically engineered mouse models (GEMMs) of pediatric high-grade glioma (pHGG). We also reported an upregulation of genes associated with neurogenesis in ATRX KO – H3.3G34R samples compared to ATRX KO – H3.3WT samples, in GEMMs of pHGG.

2.1.2 Objective and Hypothesis

In the previous chapter, we developed and probed four novel GEMMs of pHGG (H3.3WT – ATRX WT, H3.3G34R – ATRX WT, H3.3WT – ATRX WT, and H3.3G34R – ATRX KO) for transcriptomic changes. Our goal in this chapter was to extract information on the effects of H3.3G34R expression and/or ATRX loss-of-function (LoF) on Notch signaling in pHGG and the associated underlying mechanisms. To achieve this goal, we extracted information on Notch ligands and associated genes from the RNA-Sequencing data we previously generated. In GEMMs of pHGG, we observed that ATRX and H3.3G34R expression promote Notch pathway activation independently of each other and that Notch pathway activation correlated with our previously reported changes in *Dll3* regulation. We then utilized patient-derived orthotopic xenograft (PDOX) models of pHGG to confirm association of Notch pathway activation and both ATRX and H3.3G34R expression.

2.2 Materials and Methods

2.2.1 Tumor Models, Cell Lines and Reagents

2.2.1.1 Fibroblast Cell Lines

DF1 cells were grown in complete Dulbecco's Modified Eagle Medium (DMEM) media supplemented with 10% fetal bovine serum (FBS), 2mM L-glutamine, 100U Penicillin and, 100ug streptomycin). All cell lines were cultured within a humidified 37ºC, 5% CO2 incubator and authenticated through short tandem repeat (STR) profiling at least once per year.

2.2.1.2 Primary Brain Tumor Tissue Samples

Primary brain tumor tissue samples were collected following the approved institutional review board (IRB) protocols of Baylor College of Medicine and Northwestern University. Tissue arrived in complete DMEM media and was immediately processed. Tissue was mechanically dissociated, resuspended in complete DMEM media then filtered through 100 um and 40 μm cell strainers. Cells were counted with a hemacytometer then cryopreserved in Freezing Media (DMEM supplemented with 30% FBS, 2mM L-glutamine, 100U Penicillin and, 100 μg streptomycin) at a density not exceeding 3 million cells/1 mL Freezing Media and put into liquid nitrogen for long-term storage.

2.2.1.3 Plasmid Constructs

Replication Competent ALV LTR with a Splice Acceptor (RCAS) empty vector (Y) constructs were purchased from Addgene. RCAS-H3.3G34R-GFP, RCAS-H3.3WT-GFP, RCAS-PDGFA, RCAS-Cre, and RCAS-GFP plasmids were developed by and purchased from Eton Bioscience.

2.2.1.4 Cell Transfections

DF1 cells were seeded at a density of 200,000 cells/T-25 flask one day prior to transfection and allowed to grow overnight. For each transfection, 8 μL of X-tremeGENE 9 (Roche) and 243 μL DMEM in a 1.5 mL Eppendorf tube then incubated at room temperature for 5 minutes. 2.5 μg of plasmid was then added to the mixture and incubated at room temperature for 20 minutes. Previously cultured DF-1 cells in T-25 flasks had media (complete DMEM) changed and the transfection mixture was added dropwise into the flask while swirling. Each flask was allowed to grow overnight within a humidified 37ºC, 5% CO2 incubator and monitored for GFP expression in the case of GFP expressing plasmids. Transfected cells were passaged at confluency a minimum of 3 times before use in GEMM experiments.

2.2.1.5 Digestion of Murine Cerebrum Progenitors

Normal brainstem was isolated from Ntv-a;$p53^{fl/fl}$ and Ntv-a;$p53^{fl/fl}$;$ATRX^{fl/fl}$ postnatal day 3 (P3) pups and enzymatically digested in Earl's Balanced salt solution containing 4.7mg papain (Worthington) and 60 μg/mL DNAse (Sigma Aldrich). Digestion was inactivated with ovomucoid (0.7mg/mL) (Worthington) containing 14 μg/mL DNAse. Cells were consecutively washed, triturated, and strained to obtain a single cell suspension. Cells were cultured in complete DMEM media at 37°C and 5% CO2, and passaged a maximum of 3 times for experiments.

2.2.1.6 In Vitro Infection of Murine Cerebrum Progenitors with RCAS Viruses

To concentrate RCAS viruses, DF1 cells transfected with RCAS plasmids were passaged a minimum of 6 times from transfection, and then passaged 1:12. After 3 days, virus-containing media was harvested, centrifuged to remove cell debris, filtered through 0.45 μm pores, and concentrated 100-fold using Retro-X Concentrator (Clontech) per the manufacturer's instructions. Cerebrum progenitors were plated and infected with RCAS viruses at 1:100. Assays were conducted 3–5 days post-infection, or were split when confluent and subsequently plated for assays. All experiments were done a minimum of three times on at least three independent preparations of progenitor cells.

Table 7. *Ex vivo* murine cerebrum progenitor infection

Model	Transfected RCAS expressing cells	Brain harvested from (Strain)
H3.3G34R – ATRX KO	RCAS-H3.3G34R, RCAS-Cre, RCAS-PDGFA	Ntv-a;$p53^{fl/fl}$;$ATRX^{fl/fl}$
H3.3WT – ATRX KO	RCAS-H3.3WT, RCAS-Cre, RCAS-PDGFA	Ntv-a;$p53^{fl/fl}$;$ATRX^{fl/fl}$
Empty Vector – ATRX KO	RCAS-Y, RCAS-Cre, RCAS-PDGFA	Ntv-a;$p53^{fl/fl}$;$ATRX^{fl/fl}$
H3.3G34R – ATRX WT	RCAS-H3.3G34R, RCAS-Cre, RCAS-PDGFA	Ntv-a;$p53^{fl/fl}$
H3.3WT – ATRX WT	RCAS-H3.3WT, RCAS-Cre, RCAS-PDGFA	Ntv-a;$p53^{fl/fl}$
Empty Vector – ATRX WT	RCAS-Y, RCAS-Cre, RCAS-PDGFA	Ntv-a;$p53^{fl/fl}$

2.2.1.7 Antibodies

The following antibodies were used at the indicated dilutions: anti-DLL3 (Cell Signaling Technology, #71804S, 1:100), cleaved Notch1 (1:100) (Cell Signaling Technology), Notch1

(1:100) (Cell Signaling Technology #3609S), and Hes1 (1:5000) (Cell Signaling Technology #11988S).

2.2.2 Animal Studies

2.2.2.1 Animal Experiment Study Approval

All experiments with mice were completed in accordance with Northwestern University Center for Comparative Medicine (CCM) guidelines and Institutional Animal Care and Use Committee approved protocols (IACUC, protocol I500005132 and I500009591).

2.2.2.2 Mouse Strains

C57BL/6 and NOD.129S7(B6) -Rag1tm1Mom/J (SCID) mice were purchased from Jackson Laboratories, then bred in house. SCID mice 5–8 weeks of both male and female were housed and bred in the animal facility of Northwestern University, Feinberg School of Medicine.

2.2.2.3 Genetically Engineered Mouse Lines

C57BL/6 mice with conditional p53 deletion ($p53^{fl/fl)}$ and mice with conditional expression of the RCAS receptor tv-a bound to a Nestin specific promoter (Ntv-a) were purchased from Jackson Laboratory. Ntv-a and $p53^{fl/fl}$ mice were crossed until we yielded mice which homozygously expressed all alleles (Ntv-a;$p53^{fl/fl}$). ATRX flox/flox mice ($ATRX^{fl/fl}$) were generously provided by David Picketts. Ntv-a;$Np53^{fl/fl}$ mice were crossed with $ATRX^{fl/fl}$ until all alleles were homozygously expressed (Ntv-a;$p53^{fl/fl}$;$ATRX^{fl/fl}$). Homozygous expression was confirmed via genotyping.

2.2.2.4 Tail Snip Digestion

Tail snips were obtained from mice before 28 days of age. For Ntv-a and $p53^{fl/fl}$ genotyping, DNA was extracted from tail snips with the REDExtract-N-Amp Tissue PCR Kit Protocol (Millipore Sigma). For $ATRX^{fl/fl}$ genotyping, tail snips were submerged in 100uL lysis buffer (100mM Tris-HCl (pH 8.5), 5 mM EDTA, 0.2% SDS, 200 mM NaCl) and supplemented with 0.5% Proteinase K and incubated at 55 ºC overnight. Reaction tubes were mixed, incubated at 55ºC for an additional 2 hours then briefly centrifuged at 10,000 rotations per minute (rpm). 100 uL of 2-proponal was added to each tube then tubes were centrifuged for 10 minutes at 10,000 rpm. Supernatant was removed, DNA pellet was left to dry at 37ºC for 3 hours then DNA was resuspended in 100 uL of TE buffer. Concentration of resuspended DNA was measured with a NanoDrop spectrophotometer (ThermoScientific) then stored at 4 degrees until reading to be genotyped.

2.2.2.5 Genotyping

For Ntv-a and $p53^{fl/fl}$ genotyping, PCR amplification was done with the REDExtract-N-Amp PCR Reaction mix (Millipore Sigma) with appropriate primers. For $ATRX^{fl/fl}$ genotyping, PCR amplification was done with the KAPA2G Fast PCR Kit (KAPA Biosystems). PCR products were run on a 1% agarose gel. Prescence of the Ntv-a, $p53^{fl/fl}$, and $ATRX^{fl/fl}$ alleles were confirmed by presence of only one band at 800 base pairs (Ntv-a), only one band at 390 base pairs ($p53^{fl/fl}$), and a greater than 1500 base pair band for the wildtype reaction and 1500 base pair band for the mutant reaction ($ATRX^{fl/fl}$) (Table 1 – *see page 28*).

2.2.2.6 Patient Derived Orthotopic Xenograft (PDOX) Mouse Modeling

Cryopreserved patient tumor cells for three models were thawed and resuspended in complete DMEM media for orthotopic implantation. Resuspended cells were implanted into the right cerebrum of anesthetized SCID mice at a density of 100,000 cells/2uL complete DMEM media. Mice were monitored for post-operative complications for three days following implantation with no adverse events observed. Tumors were allowed to grow for 2-3 weeks before treatment was begun. Following implantation, mice were monitored daily until reaching a functional endpoint (15% weight loss or severe neurological deficits) and were then euthanized.

2.2.2.7 Euthanasia

Mice were euthanized in compliance with Northwestern University Center for Comparative Medicine (CCM) guidelines and Institutional Animal Care and Use Committee approved protocols (IACUC, protocols I500005132 and I500009591). Mice were euthanized via either (1) CO2 asphyxiation followed by cervical dislocation or (2) intraperitoneal injection of a lethal dose of Euthasol, followed by decapitation.

2.2.3 Histology

2.2.3.1 Tissue Processing

Formalin-fixed brains (10% formalin for 24 hours) were serially sectioned in the coronal plane and processed in paraffin by the Northwestern Mouse Histology and Phenotyping Laboratory. Sections cut on a microtome (Leica) at 5-µm were used for histologic and immunohistochemical staining.

2.2.3.2 Hematoxylin and Eosin (H&E) Staining

H&E staining was performed on 5-µm sections of formalin-fixed, paraffin embedded (FFPE) tissue. Slides were deparaffinized in Xylene and rehydrated using decreasingly concentrated alcohol solutions followed by water. Slides were stained with Hematoxylin then washed with water and Clarifier to remove excess Hematoxylin. Finally, slides were stained with 0.9% EosinY solution then dehydrated in increasingly concentrated alcohol solutions followed by Xylene. Cytoseal was immediately added to stained slides followed by a coverslip. Images were captured under the same light conditions on a BZ-X Series All-In-One Fluorescence Microscope (Keyence).

2.2.3.3 Immunohistochemistry (IHC)

IHC was performed using a Vectastain Elite kit (Vector Laboratories #AK-5001) as described previously with the following antibodies: anti-DLL3 (Cell Signaling Technology, #71804S, 1:100)[27]. Images were captured under the same light conditions on a BZ-X Series All-In-One Fluorescence Microscope (Keyence).

2.2.3.4 Immunofluorescence (IF)

IF was performed on 5-µm sections of FFPE tissue. Slides were deparaffinized by soaking into warm 1.3% Palmolive Ultra Original Concentrated, submerged into antigen retrieval buffer (10mM Sodium Citrate, 0.05% Tween-20, pH 6.0) and heated in a Cuisinart pressure cooker for 1 hour. The following antibodies were used: cleaved Notch1 (1:100) (Cell Signaling Technology) and Hes1 (1:5000) (Cell Signaling Technology #11988S). Images were captured on the same day using the same exposure settings on a BZ-X Series All-In-One Fluorescence Microscope (Keyence).

2.2.4 RNA-Sequencing

2.2.4.1 RNA Extraction and Library Preparation

Total RNA was isolated from snap frozen H3.3WT and H3.3G34R expressing tumors from ATRX WT and ATRX KO mice (n=5 per group) using the RNeasy kit (Qiagen #74104). Sequencing was performed by the Northwestern University Sequencing Core Facility. The Illumina TruSeq Total RNA Library Preparation Kit (Illumina # 20020596) was used to prepare sequencing libraries including rRNA depletion.

2.2.4.2 Sequencing

Sequencing was performed using an lllumina HiSeq 4000 Sequencer (Illumina) to produce single-end 50-bp reads. Trim Galore (http://www.bioinformatics.babraham.ac.uk/projects/trim_galore/) was used to trim adapters and remove poor quality reads.

2.2.4.3 Differential Gene Expression

FASTQ files were aligned to the mm10 genome using RNA-STAR, and aligned reads were counted using HTSeq-count with Ensembl mm10 gtf[28,29]. HTSeq-count files were imported into R (https://www.r-project.org/) and differential expression analysis was performed with the DESeq2 package using default settings. DESeq2 normalized reads were imported into Gene set enrichment analysis (GSEA) and standard GSEA was run with the following parameters:

permutations = 1000, permutation type = gene set, enrichment statistic = weighted, gene ranking metric = signal2noise, max size = 500, min size = 15, normalization mode = meandiv[30,31]. Box plots and volcano plots were generated using the ggplot2 and EnhancedVolcano R packages, respectively.

2.2.5 Quantitative Real-Time Polymerase Chain Reaction (RT-qPCR)

2.2.5.1 RNA Extraction and Reverse Transcription

Total RNA was isolated using the RNeasy kit (Qiagen #74104). cDNA was synthesized from total mRNA using the High-Capacity cDNA Reverse Transcription Kit (ThermoFisher Scientific #4368814). RT-qPCR EasyOligos (Sigma-Aldrich) primers were used for either human or murine *Dll3*. qPCR experiments were run using *Power* SYBR™ Green PCR Master Mix (ThermoFisher Scientific #4367659) on a QuantStudio 6 (ThermoFisher Scientific). Relative gene expression levels were generated using the ddCt method with human *Gapdh* as the reference gene for PDOX samples and murine *Taf1c* as the reference gene for RCAS/tv-a samples.

Table 8. Chapter 2 RT-qPCR primers.

Primer Name	Primer Sequence (5' -> 3')
mDLL3-FWD	TATAGACCGGGACGCTCGTG
mDLL3-REV	AACCTTGTGGCCCTCTCTGT
hDLL3	CACTCAACAACCTAAGGACGCAG
hDLL3	GAGCGTAGATGGAAGGAGCAGA

2.2.6 Statistical Analysis

Statistical analysis was performed using GraphPad Prism. Survival curves were analyzed using Log-rank (Mantel-Cox) test. Tumor incidence, grade, necrosis, infiltration, and ependymal differentiation were analyzed using Fisher's exact test. P values of less than 0.05 were considered significant for all analyses except DESeq2, in which adjusted p values (padj) < 0.05 were considered significant.

2.3 Results

2.3.1 ATRX loss and H3.3G34R expression promote upregulation of genes associated with Notch pathway activation independently of each other in GEMMs of pHGG

GSEA analysis indicates that ATRX WT H3.3G34R tumors displayed increased expression of genes associated with interactions with the extracellular matrix, upregulated Notch signaling, decreased neuronal markers and decreased expression of genes associated with H3K27me3 markers compared to ATRX WT H3.3WT tumors (Fig. 8 – *see page 47*). GSEA analysis indicates upregulation of genes associated with Notch pathway activation in ATRX WT H3.3G34R tumors compared to ATRX WT H3.3WT tumors and in ATRX KO H3.3WT tumors compared to ATRX WT H3.3WT tumors (Fig. 8 – *see page 47)*[13]. Differential expression and RT-qPCR analysis indicates that upregulation of the Notch ligand *Dll3* coincided with Notch signaling enrichment though the trend did not reach significance in the case of ATRX WT H3.3G34R vs ATRX WT H3.3WT (Fig. 11). GSEA analysis indicates that ATRX KO H3.3G34R tumors display increased markers of cell proliferation and metabolism and increased Notch signaling (Fig. 8 – *see page 47*). Upregulation of Notch signaling and *Dll3* expression in ATRX KO H3.3G34R tumors compared to ATRX WT H3.3WT tumors was more pronounced than in other comparisons (Fig. 11).

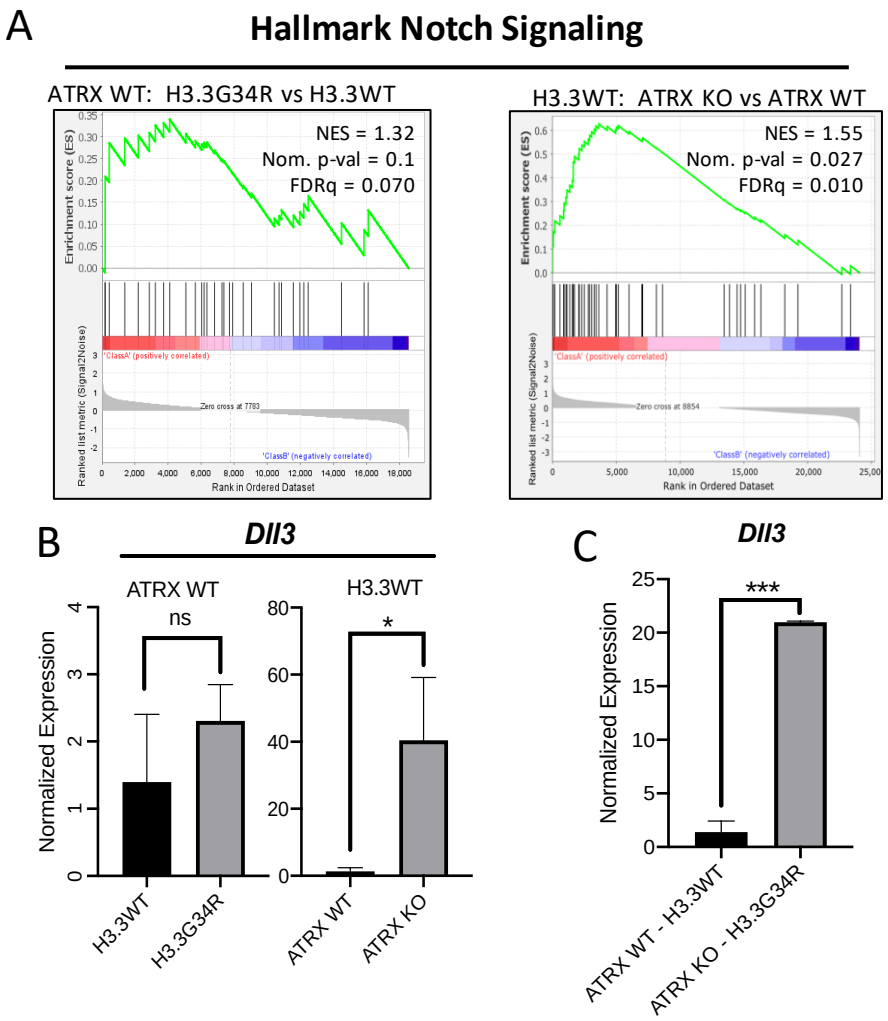

Figure 11. (A) GSEA plot (FDR < 0.1) of hallmark notch in ATRX WT H3.3G34R vs ATRX WT H3.3WT tumors and in ATRX KO H3.3WT vs ATRX WT H3.3WT tumors (n = 5 per group). (B) RT-qPCR validation of *Dll3* upregulation in ATRX WT H3.3G34R vs ATRX WT H3.3WT, ATRX KO H3.3WT vs ATRX WT H3.3WT, and (C) in ATRX KO H3.3G34Rvs H3.3WT ATRX WT tumors (n = 3 per group)(ns $P > 0.05$, ***$P < 0.001$, two-tailed unpaired t-test).

2.3.2 ATRX loss and H3.3G34R expression are independently and synergistically associated with Notch pathway activation in GEMM and PDOX models of pHGG

In order to confirm activation of the Notch pathway in GEMM tumors with ATRX loss and H3.3G34R expression, we performed immunostaining of GEMM brain tumor sections with indicators of active Notch signaling, cNotch1 and Hes1. For both markers, increased expression was observed in ATRX KO and H3.3G34R samples, compared to ATRX WT and H3.3WT samples (Figure 12). The same general trend was observed in PDOX models of pHGG. Compared to normal human cerebrum and a PDOX model of an ATRX WT H3.3WT HGG, three PDOX models of HGG with ATRX LoF and/or H3.3G34R or both had higher expression of cNotch1 (Figure 13). We did observe one PDOX model of an ATRX WT H3.3WT HGG which displayed relatively high expression of cNotch1 which we were unable to account for with our model – we would presume this particular model contains a separate Notch activating aberration however further study is necessary (Figure 13). Within the three PDOX models of HGG with ATRX LoF and/or H3.3G34R or both, we observed that increased expression of cNotch1 was more associated with ATRX LoF than H3.3G34 expression but a larger sample size is required to make a definitive statement on associations between the strength of association of H3.3G34R expression versus ATRX LoF and Notch pathway activation. (Figure 13).

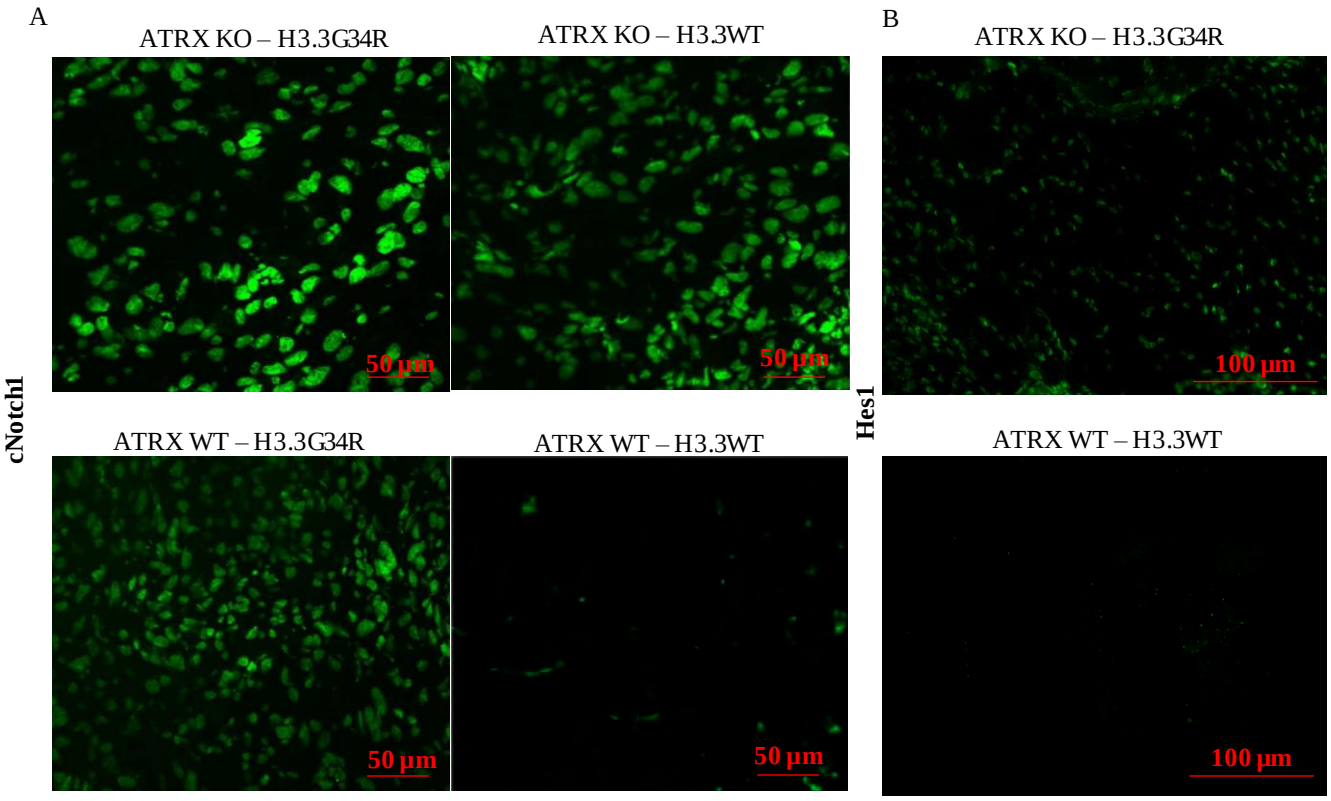

Figure 12. Representative staining of RCAS tumors with (A) cleaved Notch1 and (B) Hes1.

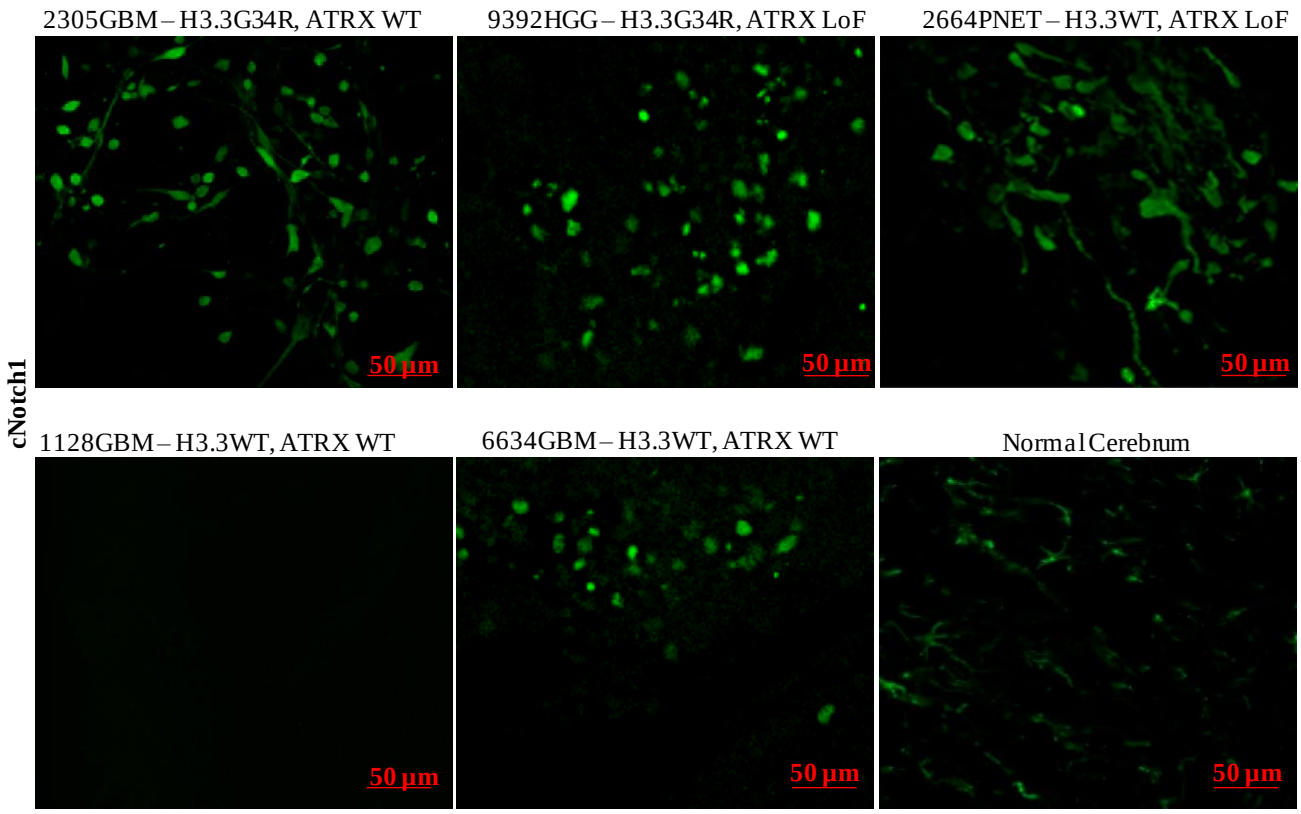

Figure 13. Representative cNotch1 staining of cerebrum from five models of PDOX tumor bearing mice and one un-injected (normal) mouse.

2.3.3 Differential Dll3 expression levels found in GEMMs of pHGG are not recapitulated in mouse neural progenitors or PDOX models pHGG

Upon confirmation of increased Notch signaling in PDOX models of Notch activation in samples with H3.3G34R expression and/or ATRX LoF, we sought to confirm the DLL3 expression trends we observed in our novel GEMMs in additional model systems. To this end, we utilized a RCAS virus treated *ex vivo* neurosphere model in addition to our previously established PDOX models of pHGG. In our *ex vivo* model, we observed a general trend of DLL3 upregulation in models with ATRX KO or H3.3G34R expression though none of these comparisons reach significance (ns $P > 0.05$, two-tailed unpaired t-test) (Figure 14). Compared

to DLL3 expression patterns in our GEMM model, we did not observe any correlative DLL3 expression trends in human derived samples however, due to limited availability of human H3.3G34R tumor samples, statistics were conducted on 1 biological replicate (6 technical replicates) for both the ATRX LoF – H3.3G34R and ATRX WT – H3.3G34R PDOX models (Figure 14). We further probed DLL3 expression in our PDOX levels at the protein level and still did not observe any trends that correlated with either our GEMM or *ex vivo* models (Figure 14).

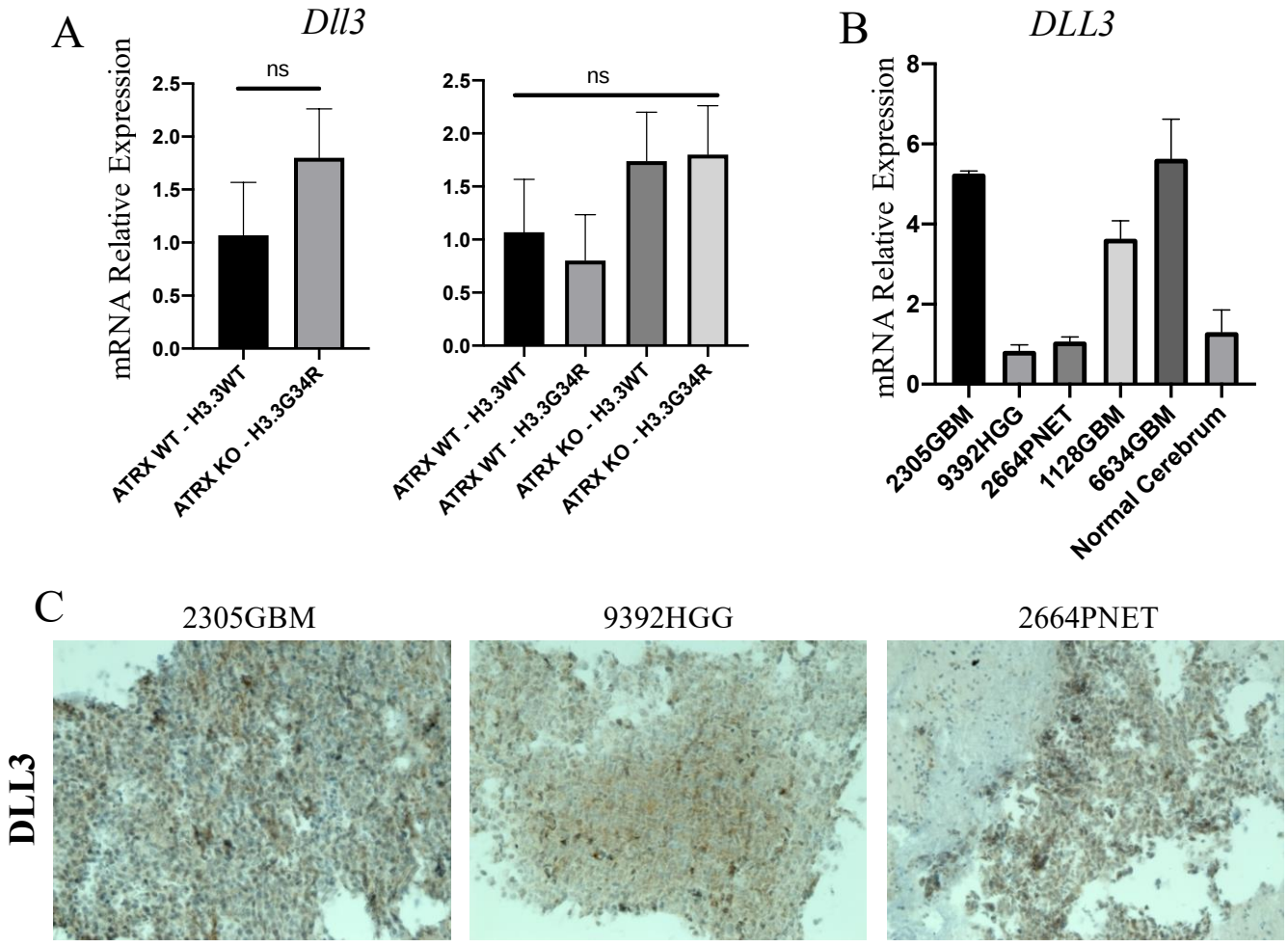

Figure 14. RT-qPCR assessment of *Dll3* expression in (B) an *ex vivo* RCAS progenitor model (C) PDOX models (n = 6 per group)(ns $P > 0.05$, two-tailed unpaired t-test). (C) Representative DLL3 staining of three PDOX model.

2.4 Discussion

The Notch pathway is a critical mediator in preserving the stem-cell like properties of radial glia, allowing a larger population to persist and later give rise to Oligodendrocyte Precursor Cells (OPCs)[76]. Notch signaling has also been identified as a potential oncogenic driver of H3.3G34 mutant pHGGs; inhibition of the Notch pathway led to decreased cell viability in both H3.3G34R and H3.3K27M expressing glioma cells[13]. One possible explanation for this is that Notch inhibition in H3.3G34 mutant cells disrupts its crosstalk with radial glia and subsequently results in a more "mature" cell state which retains less oncogenic properties. A recent study separately reported that, in the context of IDH-mutant gliomas, ATRX inactivation was associated with upregulation of the Notch pathway ligand, JAG1[77]. While we observed upregulation of genes encoding NOTCH ligands in ATRX KO H3.3G34R tumor samples vs ATRX KO H3.3WT tumor samples, significant upregulation of these genes was more closely associated with ATRX status. It appears ATRX loss is the main contributor to NOTCH pathway activation in tumor samples.

The Notch ligand DLL3, typically described as an inhibitory ligand of the pathway, is expressed at low levels in normal, healthy tissue[78]. In small cell lung cancer (SCLC), DLL3 overexpression has been well-established as a Notch pathway inhibitor and contributor to carcinogenesis[78,79]. DLL3 has also been identified as a therapeutic target in adult IDH mutant glioma, where it is commonly upregulated[80]. The mechanism of DLL3 as a Notch inhibitor is antithetical to our own data in which DLL3 overexpression is correlated with Notch pathway activation in our GEMMs. We propose two possible explanations for this phenomenon. First, as we did not observe any trends in DLL3 expression in our PDOX models, it is possible that DLL3

expression is being co-opted in our murine models through an alternate mechanism for the ultimate purpose of Notch pathway upregulation.

Secondly, it is possible that DLL3 is indeed upregulating the Notch pathway through an alternate mechanism however a small sample size for our PDOX model did not fully resolve this event[81]. The aforementioned assessment of DLL3's effects on Notch regulation were conducted in IDH-mutant gliomas, a largely adult genotype[80]. A separate spatial transcriptomics study in IDH-wildtype brain tumors (which is more typical in pediatric glioma) indicated that DLL3 overexpression was associated with upregulated Notch pathway [82]. In either of our proposed scenario, further study is required to resolve the interplay between DLL3 overexpression and Notch pathway regulation in H3.3G34R pHGG.

2.5 Future Directions

Much work is required to fully elucidate the role of H3.3G34R pHGG on the Notch pathway in the context either competent ATRX or ATRX LoF. While this chapter presents a model in which ATRX LoF and H3.3G34R are separately contributing to Notch pathway upregulation, it is still unclear how these two aberrations are cooperating (if at all) to Notch dysregulation. In chapter 1, we present data that would indicate that while H3.3G34R expression and ATRX are both independently upregulating gene sets associated with the Notch pathway, in our H3.3G34R – ATRX KO GEMM, we see downregulating of similar gene sets. We have been unable to provide a meaningful explanation for this phenomenon and so it warrants further study. As mentioned in chapter 1, an important aspect of the relationship between H3.3G34R and ATRX LoF is how ATRX/DAXX-mediated deposition of H3.3 onto the heterochromatin modulates the effects of the G34R mutation (*see 1.5)*. The experiments proposed in that section may also illuminate the relationship of H3.3G34R with ATRX LoF on Notch pathway regulation.

While we did not observe any clear trends in DLL3 expression in our PDOX models, we cannot rule out potential bias as a result of low sample numbers. Similarly, while we did observe a clear relationship between H3.3G34R expression and ATRX LoF with Notch pathway upregulation, that trend was also observed at a very low sample size. The experiments conducted in this chapter should be replicated in larger cohorts of patient or patient-derived samples before we can definitively conclude the effects of H3.3G34R expression and ATRX LoF on the Notch pathway.

Presuming that H3.3G34R expression and ATRX LoF can be correlated to Notch pathway regulation, further characterization of the of the effects of Notch inhibition on initiation,

progression and overall survival of relevant pHGG is needed. Several Notch inhibitors exist which can be used to treat H3.3G34R pHGG cells *in vitro* or *in vivo* models of H3.3G34R pHGG. Downstream analysis of *in vitro* studies with Notch inhibitors should describe its effects on cell proliferation, cell growth and apoptosis. Use of Notch inhibitors *in vivo* could provide useful information on overall survival, tumor incidence, angiogenesis and tumor growth.

CHAPTER 3: Effects of an AXL/GAS6 inhibitor on pediatric Glioblastoma

3.1 Introduction

In the previous chapters, we have described attempts to elucidate mechanisms of initiation and progression of pediatric glioma. In this chapter, we discuss potential therapeutic targets and experimentally assess the therapeutic efficacy of an AXL/GAS6 inhibitor for pediatric gliomas.

3.1.1 The AXL/GAS6 Signaling Pathway

The protein AXL, transcribed by the *AXL* gene located on the q arm of chromosome 19, is a member of the TAM (Tyro3, Axl, MerTK) family of receptor tyrosine kinases (RTKs)[83,84]. RTKs mediate cell-cell communication and are critical for an extensive range of biological processes including cell proliferation, cell differentiation and metabolism[85]. RTKs also have a well-established role in various hallmarks of cancer onset and progression including stemness, angiogenesis and metastasis in a variety of organ systems and cancer types[85,86]. In the last 25 years, RTKs have become an attractive subject for targeted molecular therapy, spurred in part by FDA approval of Herceptin (trastuzumab) in 1998[87,88].

3.1.1.1 Canonical AXL/GAS6 signaling

The protein growth arrest-specific protein 6 (GAS6) is a high-affinity ligand for AXL and serves as an activator of AXL signaling[89]. GAS6 binding of AXL induces homodimerization and trans-autophosphorylation in the intracellular kinase domain which promotes recruitment of effector proteins and adaptor molecules and subsequent activation of additional downstream signaling pathways[89,90]. Important downstream pathways of AXL/GAS6 signaling include

PI3K/AKT/mTOR, JAK/STAT, NFkB, and RAS/RAF/MEK/ERK, which influence tumor cell survival, apoptosis, therapeutic resistance and angiogenesis[89,91-93].

3.1.1.2 AXL/GAS6 signaling in the tumor microenvironment

While AXL is typically expressed at low levels in adults, upregulation of AXL/GAS6 has been demonstrated in a myriad of cancers including leukemia and cancers of the prostate, breast, esophagus, and brain[94,95]. Aberrant expression of AXL is associated with poorer overall survival and cancer progression[96]. AXL promotes anti-apoptotic effects of NF-κB and loss of AXL expression in a mouse model of osteosarcoma resulted in lower expression of the tumor marker Ki67[97,98]. The role of AXL and GAS6 in angiogenesis regulation has not been fully elucidated in either normal conditions or during carcinogenesis however aberrant AXL expression has been implicated in VEGF mediated promotion of angiogenesis in the tumor microenvironment[99-101]. Overall, AXL expression has the potential to support a pro-tumorigenic environment through promotion of cell proliferation, anti-apoptosis, angiogenesis, migration, invasion and the epithelial-mesenchymal transition (EMT)[86,102].

3.1.1.3 AXL/GAS6 signaling in glioma

AXL/GAS6 signaling has been implicated in pathogenesis of various tumors, including those of the central nervous system such as schwannomas and gliomas[96]. Several studies have shown AXL and GAS6 are highly expressed in a large subset of adult glioblastoma where high expression of AXL and/or AXL/GAS6 was associated with significantly shorter tumor progression and overall survival[103,104]. One such study also found that addition of antibodies against AXL increased the inhibition of tumor proliferation induced by neural progenitor cell

(NPC) therapies[104]. Blockage of AXL/GAS6 signaling is also sufficient to reduce glioma growth in mouse models[105]. Overall, AXL/GAS6 expression has been associated with poor survival, progression and proliferation of glioma and represents a promising potential therapeutic target.

3.1.2 Objective and hypothesis

Our hypothesis is that AVB-500 will extend median survival of tumor bearing mice and that treatment will result in lower expression of angiogenesis markers. For this chapter, we assessed the therapeutic efficacy of an AXL/GAS6 inhibitor (AVB-500) in a set of PDOX mouse models of pediatric glioblastoma. We also assessed the effects of combining AVB-500 with radiation therapy, per standard of care, on animal survival times. Finally, we analyzed mechanisms of therapy resistance in recurrent/remnant tumors of the treated patient derived orthotopic xenograft (PDOX) models. Our aim was to provide robust preclinical evidence for the use of AXL/GAS6 inhibitors in pediatric glioblastoma.

3.2 Materials and Methods

3.2.1 Tumor Models and Reagents

3.2.1.1 Primary Brain Tumor Tissue Samples

Primary brain tumor tissue samples were collected following the approved institutional review board (IRB) protocols of Baylor College of Medicine and Lurie Children's Hospital of Chicago at Northwestern University[27,106]. Tissue arrived in complete DMEM media and was immediately processed. Tissue was mechanically dissociated, resuspended in complete DMEM media then filtered through 100 µm and 40 µm cell strainers. Cells were counted with a hemacytometer then cryopreserved in Freezing Media (DMEM supplemented with 30% fetal bovine serum (FBS), 2mM L-glutamine, 100U Penicillin and, 100µg streptomycin) at a density not exceeding 3 million cells/1 mL Freezing Media and put into liquid nitrogen for long-term storage.

3.2.1.2 AXL/GAS6 inhibitor

AVB-500 is a recombinant fusion protein which binds to GAS6 at a 200-fold higher affinity than endogenous AXL, thereby drastically reducing AXL/GAS6 signaling and associated downstream functions[107]. Preclinical and early clinical studies have indicated AVB-500 is efficacious in reducing GAS6 blood serum levels and is well-tolerated both in animals and humans[107-109]. Mice were dosed with AVB-500 at 25 mg/kg via intraperitoneal (i.p.) injection at time points indicated below (*See 3.2.2.4*).

3.2.1.3 Antibodies

The following antibodies were used at the indicated dilutions: anti-Ki67 (Abcam, #ab833, 1:75), anti-cCaspase3 (Cell Signaling Technology, 9579T, 1:400), anti-VEGF-A (Cell Signaling Technology, 50661S, 1:200), and anti-CD31 (Cell Signaling Technology, 77699S, 1:200).

3.2.2 Animal Studies

3.2.2.1 Animal Experiment Study Approval

All experiments with mice were completed in accordance with Northwestern University Center for Comparative Medicine (CCM) guidelines and Institutional Animal Care and Use Committee approved protocols (IACUC, protocol I500009226 and I500009591).

3.2.2.2 Mouse Strains

NOD.129S7(B6) -Rag1tm1Mom/J (SCID) mice were purchased from Jackson Laboratories, then bred in house. SCID mice 5–8 weeks of both male and female were housed and bred in the animal facility of Northwestern University, Feinberg School of Medicine.

3.2.2.3 Patient Derived Orthotopic Xenotransplantation (PDOX) Model Development

Cryopreserved patient tumor cells for three models were thawed and resuspended in complete DMEM media for orthotopic implantation. Resuspended cells were implanted into the right cerebrum of anesthetized (isoflurane, oxygen) SCID mice at a density of 100,000 cells/2uL complete DMEM media. Mice were monitored for post-operative complications for three days following implantation with no adverse events observed. Tumors were allowed to grow for 2-4 weeks to form small, solid orthotopic xenografts before treatment was begun.

3.2.2.4 In Vivo Treatment of PDOX Models

For survival study analysis, 10 mice (5 female and 5 male) from each PDOX model were assigned to one of four groups: Control, AVB-500 only, AVB-500 + fractionated radiation (XRT) or XRT only. For control group, 25 mg/mL saline was given at 25 mg/kg, via i.p., three times a week (Monday, Wednesday, Friday) for 3 weeks. For AVB-500 only group, AVB-500 was given at 25 mg/kg, i.p., three times a week (Monday, Wednesday, Friday) for 3 weeks. For AVB-500 + XRT group, XRT delivered via a small animao irradiator RS-2000 locally at 2 Gy/day for 5 days and AVB-500 was given at 25 mg/kg, i.p., three times a week (Monday, Wednesday, Friday) for 3 weeks. For XRT only group, XRT was delivered locally at 2 Gy/day for 5 days. Following completion of the survival study drug treatment, mice were monitored daily until functional endpoints (15% weight loss or severe neurological deficits) then euthanized. For the "biology group" (samples which would be used for downstream histological and molecular analysis), drug treatment was delayed until week 5 to allow for the formation of medium (5 mm) to large (7-8mm) sized xenografts to support detailed biological analysis. 5 mice from each PDOX model were assigned to one of four groups: Control, AVB-500 only, AVB-500 + XRT or XRT only. For control group, 25 mg/mL saline was given at 25 mg/kg, i.p., three times a week (Monday, Wednesday, Friday) for 1 week. For AVB-500 only group, AVB-500 was given at 25 mg/kg, i.p., three times a week (Monday, Wednesday, Friday) for 1 week. For AVB-500 + XRT group, XRT delivered locally at 2 Gy/day for 5 days and AVB-500 was given at 25 mg/kg, i.p., three times a week (Monday, Wednesday, Friday) for 1 week. For XRT only group, XRT was delivered locally at 2 Gy/day for 5 days. Following completion of the biology groups drug treatment, mice were euthanized according to the following schedule for all PDOX

models: 30 minutes after last treatment (1 mouse/group), 24 hours after last treatment (2 mice/group), 48 hours after last treatment (2 mice/group).

3.2.2.5 Survival Analysis of In Vivo Drug Treatment

Survival time was measured as the time between orthotopic implantation of tumor cells and functional endpoint. Differences in event-free survival (EFS) between the treatment groups were analyzed using the Peto and Peto modification of the Gehan-Wilcoxon test using GraphPad Prism. P values were Bonferroni corrected for multiple testing, based on 4 treatment groups, except where ad hoc pairwise comparisons between treatment groups are denoted Pnominal.

3.2.2.6 Euthanasia

Mice were euthanized in compliance with Northwestern University Center for Comparative Medicine (CCM) guidelines and Institutional Animal Care and Use Committee approved protocols (IACUC, protocols I500005132 and I500009591). Mice were euthanized via intraperitoneal injection of a lethal dose of Euthasol, followed by decapitation.

3.2.3 Histology

3.2.3.1 Tissue Processing

Formalin-fixed whole mouse brains (10% formalin for 24 hours) were processed in paraffin on a HistoStar (ThermoFisher Scientific). Sections cut on an automated microtome (ThermoFisher Scientific) at 5-µm were used for histologic and immunohistochemical staining.

3.2.3.2 Hematoxylin and Eosin (H&E) Staining

H&E staining was performed on 5-µm sections of formalin-fixed, paraffin embedded (FFPE) tissue. Slides were deparaffinized in Xylene and rehydrated using decreasingly concentrated alcohol solutions followed by water. Slides were stained with Hematoxylin then washed with water and Clarifier to remove excess Hematoxylin. Finally, slides were stained with 0.9% EosinY solution then dehydrated in increasingly concentrated alcohol solutions followed by Xylene. Cytoseal was immediately added to stained slides followed by a coverslip. Images were captured under the same light conditions on a BZ-X Series All-In-One Fluorescence Microscope (Keyence).

3.2.3.3 Immunohistochemistry (IHC)

IHC was performed using a Vectastain Elite kit (AK-5001, Vector Laboratories, Burlingame, CA) as described previously. Primary antibodies included the human-specific anti-Ki67 (Abcam, #ab833, 1:75), anti-cCaspase3 (Cell Signaling Technology, 9579T, 1:400), anti-VEGFA (Cell Signaling Technology, 50661S, 1:200), and anti-CD31 (Cell Signaling Technology, 77699S, 1:200). Images were captured under the same light conditions on a BZ-X Series All-In-One Fluorescence Microscope (Keyence).

3.2.4 Statistical Analysis

Statistical analysis was performed using GraphPad Prism. Survival curves were analyzed using Log-rank (Mantel-Cox) test. Tumor incidence, grade, necrosis, infiltration, and ependymal differentiation were analyzed using Fisher's exact test. IHC data was analyzed using two-tailed

unpaired student t-tests. P values of less than 0.05 were considered significant for all analyses except DESeq2, in which adjusted p values (padj) < 0.05 were considered significant.

3.3 Results

3.3.1 AXL is expressed at various levels in pediatric glioblastoma

As our survival and molecular analysis was to be conducted in PDOX models of brain cancer, we first sought to extract information on the AXL pathway in pediatric brain tumors. Data on AXL expression in pediatric brain tumors was extracted from cBioPortal from previous RNAseq analysis of PPTC xenograft tumors[110]. We found that there was significant variation in AXL expression within tumor type, particularly in glioblastomas (Figure 15).

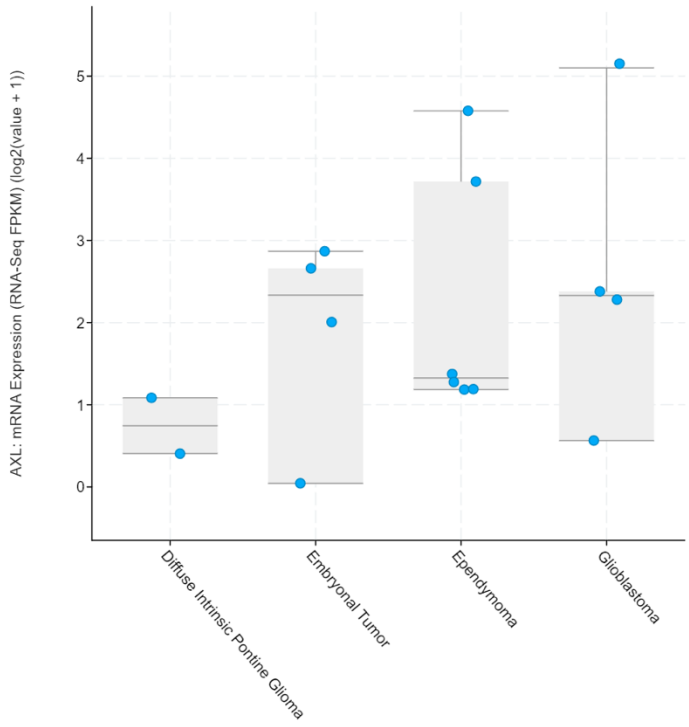

Figure 15. Expression of AXL mRNA in a panel of xenograft mouse models of pediatric brain cancers. Data were extracted from RNAseq analysis of PPTC xenograft tumors and presented as FPKM (Fragments Per Kilobase of transcript per Million mapped reads).

3.3.2 Targeting AXL expression with AVB-500 alone and in combination with radiation therapy

We utilized 3 models of pediatric glioblastoma for our analysis survival analysis and 1 model for our analysis of downstream molecular effects of AVB-500. (Table 8). AVB-500 alone and in combination with fractioned radiation was well tolerated by mice from all 3 models used for survival analysis and no toxicity related deaths were recorded. In the model IC-1406GBM-rIV, treatment with AVB-500 alone extended median survival time to 47.5 days compared to 40 days in the control group (p=0.11, Log-rank test) (Fig. 16A). Treatment with AVB-500 in combination with fractioned radiation extended median survival time to 45 days (p=0.17, Log-rank test) and treatment with fractionated radiation alone significantly extended median survival time to 72 days (p=0.015, Log-rank test) (Fig. 16A).

Table 9. Clinical, histological, and molecular features of PDOX models.

Model ID	Age/ Gender	Diagnosis	Recurrent	Molecular Subtype (Patient Tumor)	Therapy Resistant?
1406GBM	5 y/female	Glioblastoma	No	GBM_pedRTK1a	No
2305GBM	9y/ male	Glioblastoma	N/A	HGG_GBM_G34	No
104488GBM	11 y/ male	Glioblastoma	Yes	GBM_pedRTK1b	Yes
3938GBM	6.4 y/male	Glioblastoma	N/A	GBM_H3K27M	Unknown

A

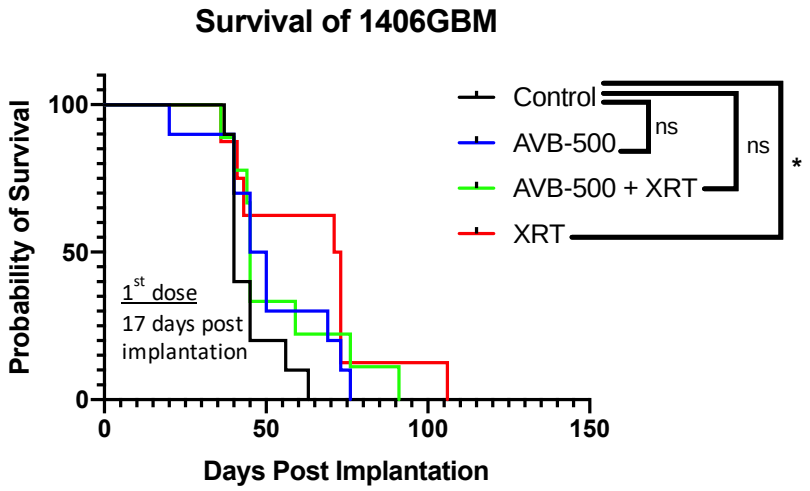

1406GBM -Group	Median Survival (Days)	Log-rank test	Gehan-Breslow-Wilcoxon test
A: Control (vehicle)	40		
B: AVB-500 (20mg/kg)	47.5	0.1090	0.1860
C: AVB-500 (20mg/kg) + XRT	45	0.1718	0.2256
D: XRT	72	0.0153	0.0453

B

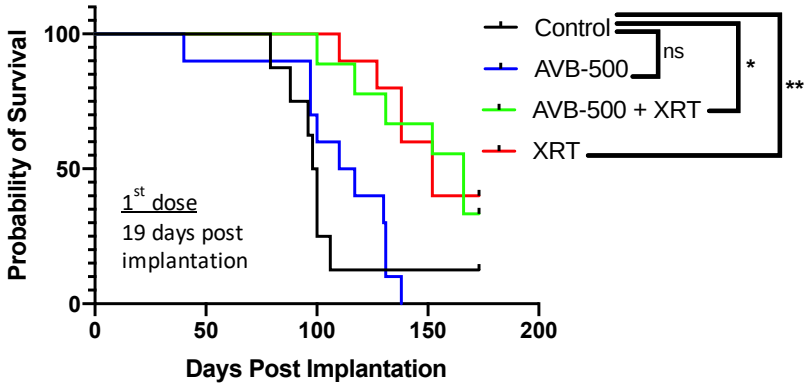

2305GBM - Group	Median Survival (Days)	Log-rank test	Gehan-Breslow-Wilcoxon test
A: Control (vehicle)	99		
B: AVB-500 (20mg/kg)	113.5	0.4867	0.2384
C: AVB-500 (20mg/kg) + XRT	166	0.0186	0.0058
D: XRT	152	0.0048	0.0013

C

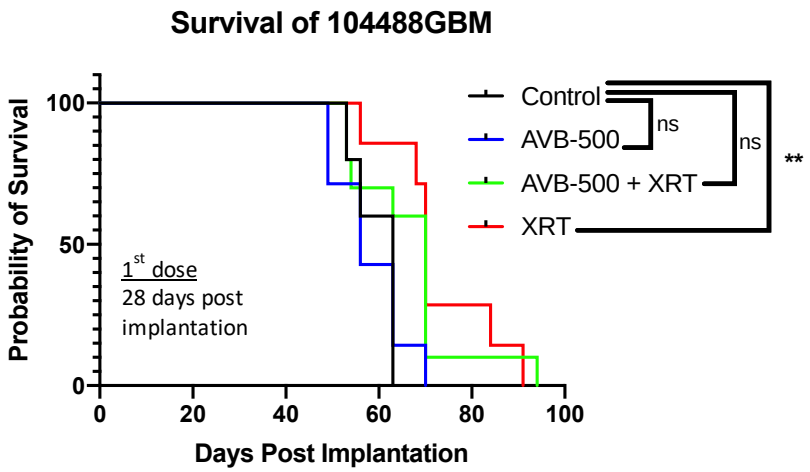

104488GBM - Group	Median Survival (Days)	Log-rank test	Gehan-Breslow-Wilcoxon test
A: Control (vehicle)	63		
B: AVB-500 (20mg/kg)	56	0.8917	0.6755
C: AVB-500 (20mg/kg) + XRT	70	0.0948	0.1763
D: XRT	70	0.0080	0.0126

Figure 16. In vivo therapeutic efficacy of AVB-500 in PDOX models of childhood brain tumors. SCID mice were implanted with xenograft cells from the three models, (A) IC-1406GBM, (B) IC-2305GBM, and (C) IC-104488GBM. Tumors were allowed to grow for 2 - 4 weeks days to form solid intra-cerebral (IC) xenograft tumors before being treated with AVB-500 alone and in combination or radiation as highlighted in the figures. Kaplan-Meier estimate of median time-to event and EFS p values were calculated and compared between the treatment groups.

In the model IC-2305GBM-rV, treatment with AVB-500 alone extended median survival time to 113.5 days compared to 99 days in the control group (p=0.49, Log-rank test) (Fig. 16B). Treatment with AVB-500 in combination with fractioned radiation significantly extended median survival time to 166 days (p=0.019, Log-rank test) and treatment with fractionated radiation alone significantly extended median survival time to 152 days (p=0.0048, Log-rank test) (Fig. 16B).

In the model IC-104488GBM-rVI, the group treated with AVB-500 alone had a reduced median survival time 56 days compared to days in the control group (p=0.11, Log-rank test) (Fig. 16C). Treatment with AVB-500 in combination with fractioned radiation and treatment with fractionated radiation alone both extended median survival time to 70 days though this increase was only significant for the fractioned radiation only group (p=0.008, Log-rank test) and not significant for the AVB-500 and XRT combination group (p=0.09, Log-rank test) (Fig. 16C). No significant change in survival between AVB-500 with fractionated radiation versus fractionated radiation alone for any model.

3.3.3 AVB-500 induced changes to histology and markers of angiogenesis

H&E staining and IHC for Ki67 and cCaspase3 was conducted routinely on harvested brains from survival analysis mice (Figure 17). Though AVB-500 in combination with fractionated radiation significantly extended median survival time in 2/3 models, AVB-500 alone did not appear to induce significant change on routine histology (Figure 17).

Assessment of potential AVB-500 induced changes in angiogenesis was completed in one model, per the biology treatment protocol described above (*see 3.2.2.4*). Tumor formation was confirmed in IC-3938GBM-rIII via H&E and Ki67 staining (Fig. 18A). IHC for two markers of angiogenesis, VEGF-A and CD31, was conducted on control and AVB-500 treated samples for IC-3938GBM-rIII (Fig. 18B). Compared to control, AVB-500 treated samples sacrificed 24 hours after biology group treatment had reduced expression of both VEGF-A and CD31, indicating AVB-500 induced reduction in markers of angiogenesis which persisted one full day after treatment was concluded (Fig. 18B).

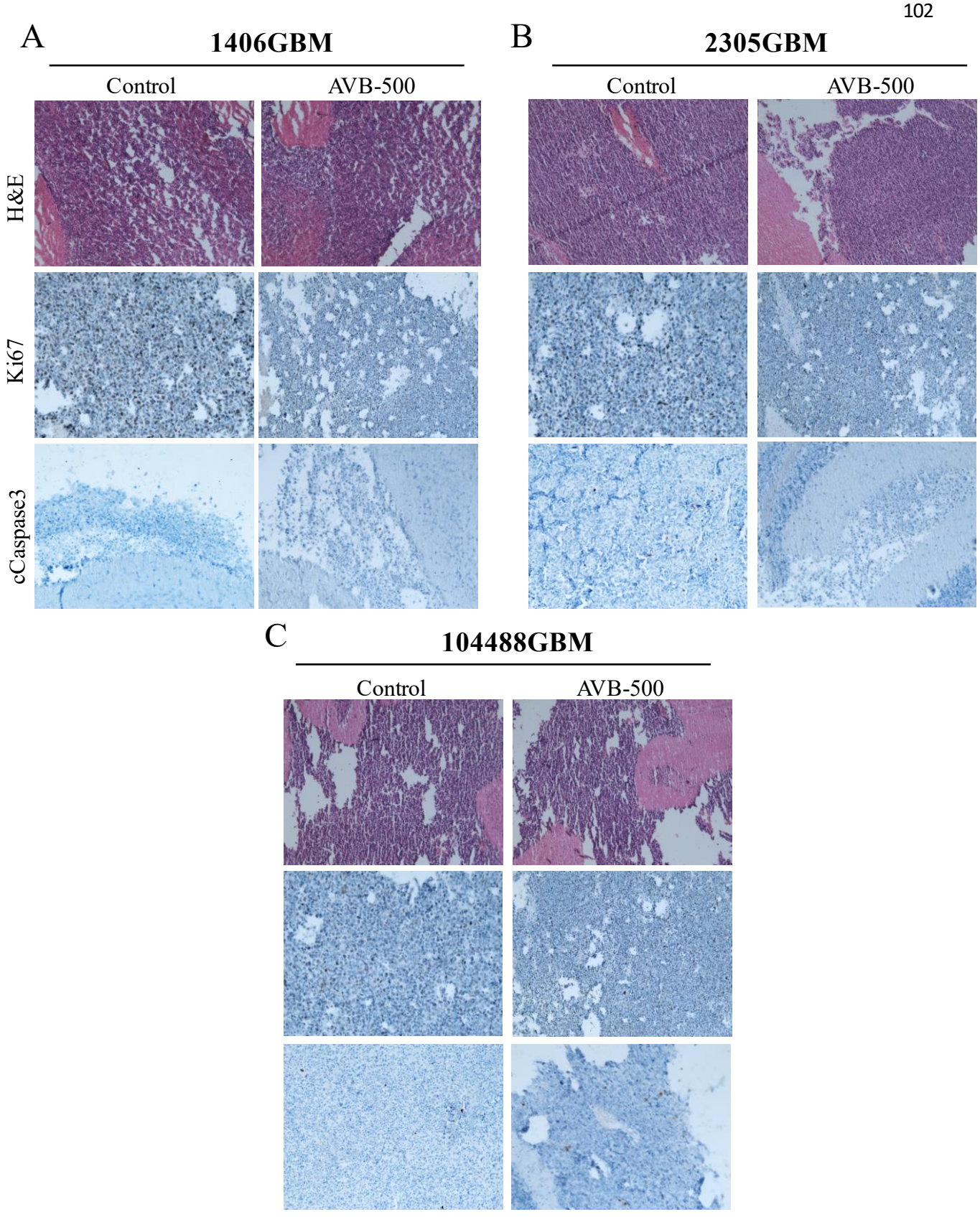

Figure 17. Representative imaging indicating no significant changes to gross morphology in (A) IC-1406 GBM, (B) IC-2305GBM, or (C) IC-104488GBM.

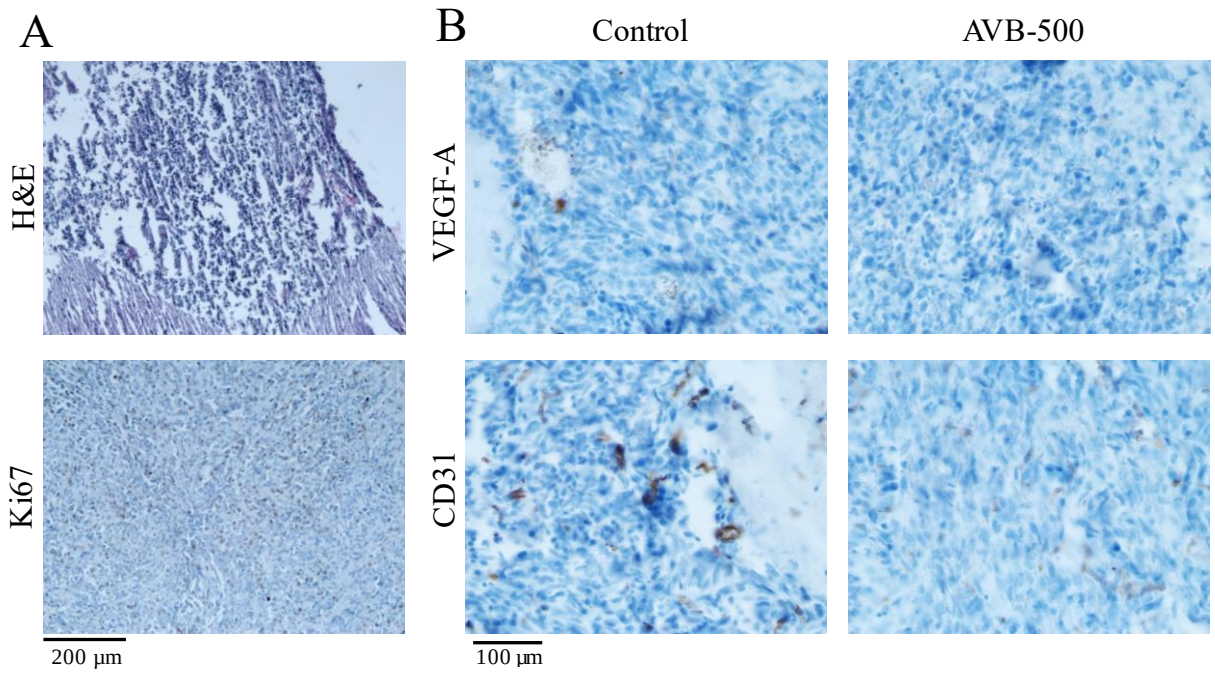

Figure 18. IC-3938GBM representative imaging (A) confirming tumor formation and for (B) markers of angiogenesis.

3.4 Discussion

AVB-500 is a novel fusion protein which ablates GAS6/AXL expression through GAS6 binding. AXL expression is expressed at varying levels in pediatric brain tumors and AXL expression has been associated with shorter overall survival in adult glioblastoma patients[103,104]. Our goal was to assess the potential therapeutic efficacy of AVB-500 in PDOX models of pediatric glioblastoma. We designed a regiment to assess AVB-500 either alone or in combination with radiation in three PDOX models of pediatric glioblastoma. We also assessed the acute biological effects of AVB-500 in one PDOX model of pediatric glioblastoma.

While survival analyses in each model yielded slightly different results, in general we observed a trend of longest survival in mice treated with radiation therapy alone, followed by AVB-500 and radiation in combination, AVB-500 alone, and finally untreated control. We did not observe any anomalies following implantation, the PDOX models chosen for survival analysis have been well-established in our laboratory and within each model, treatment with radiation alone significantly increased median survival. Combined, we are confident in the integrity of our survival analysis.

While no toxicity related deaths were reported, radiation therapy is tolerated much more poorly than AVB-500 alone. Following radiation therapy, mice exhibited symptoms such as poor skin turgor, sluggish movements, temporary weight loss, and excessive grooming. In humans, radiation therapy is also still associated with severe side effects. Despite significant increases in median survival when treated with radiation alone, the prevalence of adverse side-effects warrants additional assessment of AVB-500's therapeutic potential[111].

Targeting angiogenesis factors as a potential brain cancer therapeutic has been extensively explored. Several anti-angiogenic therapies have been developed and several more are currently undergoing clinical trials[112]. In PDOX tumors, we observed acute downregulation of two angiogenesis factors, VEGF-A and CD31 in response to treatment with AVB-500 alone. VEGF-A, one of six VEGF isoforms, is one of the main mediator of hypoxia-induced tumor growth. Early attempts to treat tumor progression with VEGF inhibitors have shown promising results but still require additional development[113 114]. Both VEGF-A and CD31, a marker of endothelial cells, can also serve as prognostic biomarkers of early stage carcinogenesis[115]. Further work is needed to elucidate the mechanism of CD31 and VEGF-A downregulation via AVB-500 treatment as well as the long term effects on angiogenesis factors after AVB-500 treatment.

3.6 Future Directions

Survival analysis of AVB-500 efficacy in 5 additional PDOX models is ongoing within our laboratory. Direct assessment of GAS6 or AXL expression before and after drug treatment in our models via IHC is also pending. We have collected blood serum from the majority of survival analysis animals which would prove to be a straightforward way to measure GAS6 or AXL expression in treated versus untreated mice. Throughout survival analysis, viable tumor cells were collected for each experimental group within each model. These cells will be vital for RNA-sequencing analysis, and potentially single-cell RNA-Sequencing analysis, allowing us to probe broad transcriptomic changes induced by AVB-500 alone or in combination with radiation therapy as well as the identification of therapy resistant cell subpopulations. The effects of AVB-500 on angiogenesis must also be elucidated more thoroughly. This can be done quicky and efficiently by counting the number of blood vessels (with <8 red blood cells) in AVB-500 treated versus untreated brain tissue. While we did not observe any general changes in gross histological structures between AVB-500 treated brains and untreated controls, it could be beneficial to assess the effects of AVB-500 on tumor invasion and metastasis. It is also important to note that AVB-500 has not yet been assessed for optimal dosage as Phase II trials are still underway. We report that AVB-500 is well tolerated in mice and potential increases in dosage may increase effectiveness of the treatment.

REFERENCES

1 Adel Fahmideh, M. & Scheurer, M. E. Pediatric Brain Tumors: Descriptive Epidemiology, Risk Factors, and Future Directions. *Cancer Epidemiol Biomarkers Prev* **30**, 813-821, doi:10.1158/1055-9965.EPI-20-1443 (2021).

2 Pollack, I. F. & Jakacki, R. I. Childhood brain tumors: epidemiology, current management and future directions. *Nat Rev Neurol* **7**, 495-506, doi:10.1038/nrneurol.2011.110 (2011).

3 Kasper, L. H. & Baker, S. J. Invited Review: Emerging functions of histone H3 mutations in paediatric diffuse high-grade gliomas. *Neuropathol Appl Neurobiol* **46**, 73-85, doi:10.1111/nan.12591 (2020).

4 Wu, G. *et al.* Somatic histone H3 alterations in pediatric diffuse intrinsic pontine gliomas and non-brainstem glioblastomas. *Nat Genet* **44**, 251-253, doi:10.1038/ng.1102 (2012).

5 Schwartzentruber, J. *et al.* Driver mutations in histone H3.3 and chromatin remodelling genes in paediatric glioblastoma. *Nature* **482**, 226-231, doi:10.1038/nature10833 (2012).

6 Lewis, P. W., Elsaesser, S. J., Noh, K. M., Stadler, S. C. & Allis, C. D. Daxx is an H3.3-specific histone chaperone and cooperates with ATRX in replication-independent chromatin assembly at telomeres. *Proc Natl Acad Sci U S A* **107**, 14075-14080, doi:10.1073/pnas.1008850107 (2010).

7 Goldberg, A. D. *et al.* Distinct factors control histone variant H3.3 localization at specific genomic regions. *Cell* **140**, 678-691, doi:10.1016/j.cell.2010.01.003 (2010).

8 Wong, L. H. *et al.* ATRX interacts with H3.3 in maintaining telomere structural integrity in pluripotent embryonic stem cells. *Genome Res* **20**, 351-360, doi:10.1101/gr.101477.109 (2010).

9 Pfister, S. M. *et al.* A Summary of the Inaugural WHO Classification of Pediatric Tumors: Transitioning from the Optical into the Molecular Era. *Cancer Discov* **12**, 331-355, doi:10.1158/2159-8290.CD-21-1094 (2022).

10 Larson, J. D. *et al.* Histone H3.3 K27M Accelerates Spontaneous Brainstem Glioma and Drives Restricted Changes in Bivalent Gene Expression. *Cancer Cell* **35**, 140-155 e147, doi:10.1016/j.ccell.2018.11.015 (2019).

11 Pathania, M. *et al.* H3.3(K27M) Cooperates with Trp53 Loss and PDGFRA Gain in Mouse Embryonic Neural Progenitor Cells to Induce Invasive High-Grade Gliomas. *Cancer Cell* **32**, 684-700 e689, doi:10.1016/j.ccell.2017.09.014 (2017).

12 Jones, C. & Baker, S. J. Unique genetic and epigenetic mechanisms driving paediatric diffuse high-grade glioma. *Nat Rev Cancer* **14**, doi:10.1038/nrc3811 (2014).

13 Chen, K. Y. *et al.* Reciprocal H3.3 gene editing identifies K27M and G34R mechanisms in pediatric glioma including NOTCH signaling. *Commun Biol* **3**, 363, doi:10.1038/s42003-020-1076-0 (2020).

14 Mackay, A. *et al.* Integrated Molecular Meta-Analysis of 1,000 Pediatric High-Grade and Diffuse Intrinsic Pontine Glioma. *Cancer Cell* **32**, 520-537 e525, doi:10.1016/j.ccell.2017.08.017 (2017).

15 Lewis, P. W. *et al.* Inhibition of PRC2 activity by a gain-of-function H3 mutation found in pediatric glioblastoma. *Science* **340**, 857-861, doi:10.1126/science.1232245 (2013).

16 Jain, S. U. *et al.* Histone H3.3 G34 mutations promote aberrant PRC2 activity and drive tumor progression. *Proc Natl Acad Sci U S A* **117**, 27354-27364, doi:10.1073/pnas.2006076117 (2020).

17 Shi, L., Shi, J., Shi, X., Li, W. & Wen, H. Histone H3.3 G34 Mutations Alter Histone H3K36 and H3K27 Methylation In Cis. *J Mol Biol* **430**, 1562-1565, doi:10.1016/j.jmb.2018.04.014 (2018).

18 Yang, S. *et al.* Molecular basis for oncohistone H3 recognition by SETD2 methyltransferase. *Genes Dev* **30**, 1611-1616, doi:10.1101/gad.284323.116 (2016).

19 De La Fuente, R., Baumann, C. & Viveiros, M. M. Role of ATRX in chromatin structure and function: implications for chromosome instability and human disease. *Reproduction* **142**, 221-234, doi:10.1530/REP-10-0380 (2011).

20 Picketts, D. J. *et al.* ATRX encodes a novel member of the SNF2 family of proteins: mutations point to a common mechanism underlying the ATR-X syndrome. *Hum Mol Genet* **5**, 1899-1907, doi:10.1093/hmg/5.12.1899 (1996).

21 Gibbons, R. J., Picketts, D. J., Villard, L. & Higgs, D. R. Mutations in a putative global transcriptional regulator cause X-linked mental retardation with alpha-thalassemia (ATR-X syndrome). *Cell* **80**, 837-845, doi:10.1016/0092-8674(95)90287-2 (1995).

22 Gibbons, R. J. *et al.* Mutations in the chromatin-associated protein ATRX. *Hum Mutat* **29**, 796-802, doi:10.1002/humu.20734 (2008).

23 Abedalthagafi, M. *et al.* The alternative lengthening of telomere phenotype is significantly associated with loss of ATRX expression in high-grade pediatric and adult astrocytomas: a multi-institutional study of 214 astrocytomas. *Mod Pathol* **26**, 1425-1432, doi:10.1038/modpathol.2013.90 (2013).

24 Kannan, K. *et al.* Whole-exome sequencing identifies ATRX mutation as a key molecular determinant in lower-grade glioma. *Oncotarget* **3**, 1194-1203, doi:10.18632/oncotarget.689 (2012).

25 Leeper, H. E. *et al.* IDH mutation, 1p19q codeletion and ATRX loss in WHO grade II gliomas. *Oncotarget* **6**, 30295-30305, doi:10.18632/oncotarget.4497 (2015).

26 Liu, X. Y. *et al.* Frequent ATRX mutations and loss of expression in adult diffuse astrocytic tumors carrying IDH1/IDH2 and TP53 mutations. *Acta Neuropathol* **124**, 615-625, doi:10.1007/s00401-012-1031-3 (2012).

27 Shu, Q. *et al.* Direct orthotopic transplantation of fresh surgical specimen preserves CD133+ tumor cells in clinically relevant mouse models of medulloblastoma and glioma. *Stem Cells* **26**, 1414-1424, doi:10.1634/stemcells.2007-1009 (2008).

28 Dobin, A. *et al.* STAR: ultrafast universal RNA-seq aligner. *Bioinformatics* **29**, 15-21, doi:10.1093/bioinformatics/bts635 (2013).

29 Abdel-Qadir, H. *et al.* A Population-Based Study of Cardiovascular Mortality Following Early-Stage Breast Cancer. *JAMA Cardiol* **2**, 88-93, doi:10.1001/jamacardio.2016.3841 (2017).

30 Love, M. I., Huber, W. & Anders, S. Moderated estimation of fold change and dispersion for RNA-seq data with DESeq2. *Genome Biol* **15**, 550, doi:10.1186/s13059-014-0550-8 (2014).

31 Subramanian, A. *et al.* Gene set enrichment analysis: a knowledge-based approach for interpreting genome-wide expression profiles. *Proc Natl Acad Sci U S A* **102**, 15545-15550, doi:10.1073/pnas.0506580102 (2005).

32 Haase, S. *et al.* H3.3-G34 mutations impair DNA repair and promote cGAS/STING-mediated immune responses in pediatric high-grade glioma models. *J Clin Invest* **132**, doi:10.1172/JCI154229 (2022).

33 Chen, C. C. L. *et al.* Histone H3.3G34-Mutant Interneuron Progenitors Co-opt PDGFRA for Gliomagenesis. *Cell* **183**, 1617-1633 e1622, doi:10.1016/j.cell.2020.11.012 (2020).

34 Korshunov, A. *et al.* Histologically distinct neuroepithelial tumors with histone 3 G34 mutation are molecularly similar and comprise a single nosologic entity. *Acta Neuropathol* **131**, 137-146, doi:10.1007/s00401-015-1493-1 (2016).

35 Céline Gonçalves, E. s. L. B., Philippe Arnaud, Bruno Costa. HOX gene cluster (de)regulation in brain: from neurodevelopment to malignant glial tumours. *Cellular and Molecular Life Sciences, Springer Verlag*, 3797-3821 (2020).

36 da Silva, R. A. *et al.* HOXA cluster gene expression during osteoblast differentiation involves epigenetic control. *Bone* **125**, 74-86, doi:10.1016/j.bone.2019.04.026 (2019).

37 Cimino, P. J. *et al.* Increased HOXA5 expression provides a selective advantage for gain of whole chromosome 7 in IDH wild-type glioblastoma. *Genes Dev* **32**, 512-523, doi:10.1101/gad.312157.118 (2018).

38 Bressan, R. B. *et al.* Regional identity of human neural stem cells determines oncogenic responses to histone H3.3 mutants. *Cell Stem Cell* **28**, 877-893 e879, doi:10.1016/j.stem.2021.01.016 (2021).

39 Funato, K., Smith, R. C., Saito, Y. & Tabar, V. Dissecting the impact of regional identity and the oncogenic role of human-specific NOTCH2NL in an hESC model of H3.3G34R-mutant glioma. *Cell Stem Cell* **28**, 894-905 e897, doi:10.1016/j.stem.2021.02.003 (2021).

40 Sturm, D. *et al.* Hotspot mutations in H3F3A and IDH1 define distinct epigenetic and biological subgroups of glioblastoma. *Cancer Cell* **22**, 425-437, doi:10.1016/j.ccr.2012.08.024 (2012).

41 Sweha, S. R. *et al.* Epigenetically defined therapeutic targeting in H3.3G34R/V high-grade gliomas. *Sci Transl Med* **13**, eabf7860, doi:10.1126/scitranslmed.abf7860 (2021).

42 Korshunov, A. *et al.* Integrated analysis of pediatric glioblastoma reveals a subset of biologically favorable tumors with associated molecular prognostic markers. *Acta Neuropathol* **129**, 669-678, doi:10.1007/s00401-015-1405-4 (2015).

43 Wiestler, B. *et al.* ATRX loss refines the classification of anaplastic gliomas and identifies a subgroup of IDH mutant astrocytic tumors with better prognosis. *Acta Neuropathol* **126**, 443-451, doi:10.1007/s00401-013-1156-z (2013).

44 Louis, D. N. *et al.* The 2016 World Health Organization Classification of Tumors of the Central Nervous System: a summary. *Acta Neuropathol* **131**, 803-820, doi:10.1007/s00401-016-1545-1 (2016).

45 Masui, K., Mischel, P. S. & Reifenberger, G. Molecular classification of gliomas. *Handb Clin Neurol* **134**, 97-120, doi:10.1016/B978-0-12-802997-8.00006-2 (2016).

46 Gallo, M. *et al.* A tumorigenic MLL-homeobox network in human glioblastoma stem cells. *Cancer Res* **73**, 417-427, doi:10.1158/0008-5472.CAN-12-1881 (2013).

47 Ulgen, E. *et al.* Mutations and Copy Number Alterations in IDH Wild-Type Glioblastomas Are Shaped by Different Oncogenic Mechanisms. *Biomedicines* **8**, 574, doi:10.3390/biomedicines8120574 (2020).

48 Torne, J. *et al.* Two HIRA-dependent pathways mediate H3.3 de novo deposition and recycling during transcription. *Nat Struct Mol Biol* **27**, 1057-1068, doi:10.1038/s41594-020-0492-7 (2020).

49 Yuan, A., Rao, M. V., Veeranna & Nixon, R. A. Neurofilaments and Neurofilament Proteins in Health and Disease. *Cold Spring Harb Perspect Biol* **9**, a018309, doi:10.1101/cshperspect.a018309 (2017).

50 Fults, D., Pedone, C. A., Morse, H. G., Rose, J. W. & McKay, R. D. Establishment and characterization of a human primitive neuroectodermal tumor cell line from the cerebral hemisphere. *J Neuropathol Exp Neurol* **51**, 272-280, doi:10.1097/00005072-199205000-00005 (1992).

51 Neftel, C. *et al.* An Integrative Model of Cellular States, Plasticity, and Genetics for Glioblastoma. *Cell* **178**, 835-849 e821, doi:10.1016/j.cell.2019.06.024 (2019).

52 Chiellini, C. *et al.* Stathmin-like 2, a developmentally-associated neuronal marker, is expressed and modulated during osteogenesis of human mesenchymal stem cells. *Biochem Biophys Res Commun* **374**, 64-68, doi:10.1016/j.bbrc.2008.06.121 (2008).

53 Lutsik, P. *et al.* Globally altered epigenetic landscape and delayed osteogenic differentiation in H3.3-G34W-mutant giant cell tumor of bone. *Nat Commun* **11**, 5414, doi:10.1038/s41467-020-18955-y (2020).

54 Papanicolaou, M. *et al.* Temporal profiling of the breast tumour microenvironment reveals collagen XII as a driver of metastasis. *Nat Commun* **13**, 4587, doi:10.1038/s41467-022-32255-7 (2022).

55 Fang, R. *et al.* Comprehensive analysis of single cell ATAC-seq data with SnapATAC. *Nat Commun* **12**, 1337, doi:10.1038/s41467-021-21583-9 (2021).

56 Skene, P. J. & Henikoff, S. An efficient targeted nuclease strategy for high-resolution mapping of DNA binding sites. *Elife* **6**, doi:10.7554/eLife.21856 (2017).

57 Stundon, J. L. *et al.* ALT in Pediatric High-Grade Gliomas Can Occur without ATRX Mutation and is Enriched in Patients with Pathogenic Germline MMR Variants. *Neuro Oncol*, doi:10.1093/neuonc/noac278 (2022).

58 Feuerbach, L. *et al.* TelomereHunter - in silico estimation of telomere content and composition from cancer genomes. *BMC Bioinformatics* **20**, 272, doi:10.1186/s12859-019-2851-0 (2019).

59 Henson, J. D. *et al.* The C-Circle Assay for alternative-lengthening-of-telomeres activity. *Methods* **114**, 74-84, doi:10.1016/j.ymeth.2016.08.016 (2017).

60 Canela, A., Vera, E., Klatt, P. & Blasco, M. A. High-throughput telomere length quantification by FISH and its application to human population studies. *Proc Natl Acad Sci U S A* **104**, 5300-5305, doi:10.1073/pnas.0609367104 (2007).

61 Hanahan, D. & Weinberg, R. A. Hallmarks of cancer: the next generation. *Cell* **144**, 646-674, doi:10.1016/j.cell.2011.02.013 (2011).

62 D'Souza, B., Meloty-Kapella, L. & Weinmaster, G. Canonical and non-canonical Notch ligands. *Curr Top Dev Biol* **92**, 73-129, doi:10.1016/S0070-2153(10)92003-6 (2010).

63 Chang, W. H. & Lai, A. G. Aberrations in Notch-Hedgehog signalling reveal cancer stem cells harbouring conserved oncogenic properties associated with hypoxia and immunoevasion. *Br J Cancer* **121**, 666-678, doi:10.1038/s41416-019-0572-9 (2019).

64 Aster, J. C., Pear, W. S. & Blacklow, S. C. The Varied Roles of Notch in Cancer. *Annu Rev Pathol* **12**, 245-275, doi:10.1146/annurev-pathol-052016-100127 (2017).

65 D'Amico, M. & De Amicis, F. Aberrant Notch signaling in gliomas: a potential landscape of actionable converging targets for combination approach in therapies resistance. *Cancer Drug Resist* **5**, 939-953, doi:10.20517/cdr.2022.46 (2022).

66 Kopan, R. & Ilagan, M. X. The canonical Notch signaling pathway: unfolding the activation mechanism. *Cell* **137**, 216-233, doi:10.1016/j.cell.2009.03.045 (2009).

67 Ayaz, F. & Osborne, B. A. Non-canonical notch signaling in cancer and immunity. *Front Oncol* **4**, 345, doi:10.3389/fonc.2014.00345 (2014).

68 Andersen, P., Uosaki, H., Shenje, L. T. & Kwon, C. Non-canonical Notch signaling: emerging role and mechanism. *Trends Cell Biol* **22**, 257-265, doi:10.1016/j.tcb.2012.02.003 (2012).

69 Pear, W. S., Aster, J.C., Scott, M. L., Hasserjian, R.P., Soffer, B., Sklar, J., Baltimore, D. . Exclusive development of T cell neoplasms in mice transplanted with bone marrow expressing activated Notch alleles. *Journal of Experimental Medicine* **183**, 2283-2291 (1996).

70 Bazzoni, R. & Bentivegna, A. Role of Notch Signaling Pathway in Glioblastoma Pathogenesis. *Cancers (Basel)* **11**, doi:10.3390/cancers11030292 (2019).

71 Qiang, L. *et al.* HIF-1alpha is critical for hypoxia-mediated maintenance of glioblastoma stem cells by activating Notch signaling pathway. *Cell Death Differ* **19**, 284-294, doi:10.1038/cdd.2011.95 (2012).

72 Dirks, P. B. Brain tumor stem cells: the cancer stem cell hypothesis writ large. *Molecular Oncology* **4**, 420-430 (2010).

73 Oldrini, B., Schuhmacher, A. J. & Squatrito, M. Take It Down a NOTCH in Forebrain Tumors. *Cancer Cell* **28**, 681-682, doi:10.1016/j.ccell.2015.11.008 (2015).

74 Phillips, H. S. *et al.* Molecular subclasses of high-grade glioma predict prognosis, delineate a pattern of disease progression, and resemble stages in neurogenesis. *Cancer Cell* **9**, 157-173, doi:10.1016/j.ccr.2006.02.019 (2006).

75 Hu, Y. Y. *et al.* Hif-1alpha and Hif-2alpha differentially regulate Notch signaling through competitive interaction with the intracellular domain of Notch receptors in glioma stem cells. *Cancer Lett* **349**, 67-76, doi:10.1016/j.canlet.2014.03.035 (2014).

76 Bergles, D. E. & Richardson, W. D. Oligodendrocyte Development and Plasticity. *Cold Spring Harb Perspect Biol* **8**, a020453, doi:10.1101/cshperspect.a020453 (2015).

77 Babikir, H. *et al.* ATRX regulates glial identity and the tumor microenvironment in IDH-mutant glioma. *Genome Biol* **22**, 311, doi:10.1186/s13059-021-02535-4 (2021).

78 Sabari, J. K., Lok, B. H., Laird, J. H., Poirier, J. T. & Rudin, C. M. Unravelling the biology of SCLC: implications for therapy. *Nat Rev Clin Oncol* **14**, 549-561, doi:10.1038/nrclinonc.2017.71 (2017).

79 Saunders, L. R. *et al.* A DLL3-targeted antibody-drug conjugate eradicates high-grade pulmonary neuroendocrine tumor-initiating cells in vivo. *Sci Transl Med* **7**, 302ra136, doi:10.1126/scitranslmed.aac9459 (2015).

80 Spino, M. *et al.* Cell Surface Notch Ligand DLL3 is a Therapeutic Target in Isocitrate Dehydrogenase-mutant Glioma. *Clin Cancer Res* **25**, 1261-1271, doi:10.1158/1078-0432.CCR-18-2312 (2019).

81 Xiu, M. X., Liu, Y. M. & Kuang, B. H. The Role of DLLs in Cancer: A Novel Therapeutic Target. *Onco Targets Ther* **13**, 3881-3901, doi:10.2147/OTT.S244860 (2020).

82 Jungk, C. *et al.* Spatial transcriptome analysis reveals Notch pathway-associated prognostic markers in IDH1 wild-type glioblastoma involving the subventricular zone. *BMC Med* **14**, 170, doi:10.1186/s12916-016-0710-7 (2016).

83 Liu, E., Hjelle, B. & Bishop, J. M. Transforming genes in chronic myelogenous leukemia. *Proc Natl Acad Sci U S A* **85**, 1952-1956, doi:10.1073/pnas.85.6.1952 (1988).

84 Graham, D. K., DeRyckere, D., Davies, K. D. & Earp, H. S. The TAM family: phosphatidylserine sensing receptor tyrosine kinases gone awry in cancer. *Nat Rev Cancer* **14**, 769-785, doi:10.1038/nrc3847 (2014).

85 Du, Z. & Lovly, C. M. Mechanisms of receptor tyrosine kinase activation in cancer. *Mol Cancer* **17**, 58, doi:10.1186/s12943-018-0782-4 (2018).

86 Zhu, C., Wei, Y. & Wei, X. AXL receptor tyrosine kinase as a promising anti-cancer approach: functions, molecular mechanisms and clinical applications. *Mol Cancer* **18**, 153, doi:10.1186/s12943-019-1090-3 (2019).

87 Lemmon, M. A. & Schlessinger, J. Cell signaling by receptor tyrosine kinases. *Cell* **141**, 1117-1134, doi:10.1016/j.cell.2010.06.011 (2010).

88 Piccart-Gebhart, M. J. *et al.* Trastuzumab after adjuvant chemotherapy in HER2-positive breast cancer. *N Engl J Med* **353**, 1659-1672, doi:10.1056/NEJMoa052306 (2005).

89 Feneyrolles, C. *et al.* Axl kinase as a key target for oncology: focus on small molecule inhibitors. *Mol Cancer Ther* **13**, 2141-2148, doi:10.1158/1535-7163.MCT-13-1083 (2014).

90 Sasaki, T. *et al.* Structural basis for Gas6-Axl signalling. *EMBO J* **25**, 80-87, doi:10.1038/sj.emboj.7600912 (2006).

91 Huang, H., Liu, H., Yan, R. & Hu, M. PI3K/Akt and ERK/MAPK Signaling Promote Different Aspects of Neuron Survival and Axonal Regrowth Following Rat Facial Nerve Axotomy. *Neurochem Res* **42**, 3515-3524, doi:10.1007/s11064-017-2399-1 (2017).

92 Sen, T. *et al.* Targeting AXL and mTOR Pathway Overcomes Primary and Acquired Resistance to WEE1 Inhibition in Small-Cell Lung Cancer. *Clin Cancer Res* **23**, 6239-6253, doi:10.1158/1078-0432.CCR-17-1284 (2017).

93 Kariolis, M. S. *et al.* Inhibition of the GAS6/AXL pathway augments the efficacy of chemotherapies. *J Clin Invest* **127**, 183-198, doi:10.1172/JCI85610 (2017).

94 Vajkoczy, P. *et al.* Dominant-negative inhibition of the Axl receptor tyrosine kinase suppresses brain tumor cell growth and invasion and prolongs survival. *Proc Natl Acad Sci U S A* **103**, 5799-5804, doi:10.1073/pnas.0510923103 (2006).

95 Funakoshi, H., Yonemasu, T., Nakano, T., Matumoto, K. & Nakamura, T. Identification of Gas6, a putative ligand for Sky and Axl receptor tyrosine kinases, as a novel neurotrophic factor for hippocampal neurons. *J Neurosci Res* **68**, 150-160, doi:10.1002/jnr.10211 (2002).

96 Wu, G. *et al.* Molecular insights of Gas6/TAM in cancer development and therapy. *Cell Death Dis* **8**, e2700, doi:10.1038/cddis.2017.113 (2017).

97 Katagiri, M. *et al.* Mechanism of stimulation of osteoclastic bone resorption through Gas6/Tyro 3, a receptor tyrosine kinase signaling, in mouse osteoclasts. *J Biol Chem* **276**, 7376-7382, doi:10.1074/jbc.M007393200 (2001).

98 Han, J. *et al.* Gas6/Axl mediates tumor cell apoptosis, migration and invasion and predicts the clinical outcome of osteosarcoma patients. *Biochem Biophys Res Commun* **435**, 493-500, doi:10.1016/j.bbrc.2013.05.019 (2013).

99 Ramjiawan, R. R., Griffioen, A. W. & Duda, D. G. Anti-angiogenesis for cancer revisited: Is there a role for combinations with immunotherapy? *Angiogenesis* **20**, 185-204, doi:10.1007/s10456-017-9552-y (2017).

100 Asahara, T. *et al.* Isolation of putative progenitor endothelial cells for angiogenesis. *Science* **275**, 964-967, doi:10.1126/science.275.5302.964 (1997).

101 Rothlin, C. V. & Lemke, G. TAM receptor signaling and autoimmune disease. *Curr Opin Immunol* **22**, 740-746, doi:10.1016/j.coi.2010.10.001 (2010).

102 Zagorska, A., Traves, P. G., Lew, E. D., Dransfield, I. & Lemke, G. Diversification of TAM receptor tyrosine kinase function. *Nat Immunol* **15**, 920-928, doi:10.1038/ni.2986 (2014).

103 Hutterer, M. *et al.* Axl and growth arrest-specific gene 6 are frequently overexpressed in human gliomas and predict poor prognosis in patients with glioblastoma multiforme. *Clin Cancer Res* **14**, 130-138, doi:10.1158/1078-0432.CCR-07-0862 (2008).

104 Staflin, K., Zuchner, T., Honeth, G., Darabi, A. & Lundberg, C. Identification of proteins involved in neural progenitor cell targeting of gliomas. *BMC Cancer* **9**, 206, doi:10.1186/1471-2407-9-206 (2009).

105 Bell, J. B. *et al.* MNK Inhibition Disrupts Mesenchymal Glioma Stem Cells and Prolongs Survival in a Mouse Model of Glioblastoma. *Mol Cancer Res* **14**, 984-993, doi:10.1158/1541-7786.MCR-16-0172 (2016).

106 Yu, L. *et al.* A single intravenous injection of oncolytic picornavirus SVV-001 eliminates medulloblastomas in primary tumor-based orthotopic xenograft mouse models. *Neuro Oncol* **13**, 14-27, doi:10.1093/neuonc/noq148 (2011).

107 Fuh, K. C. *et al.* Phase 1b study of AVB-500 in combination with paclitaxel or pegylated liposomal doxorubicin platinum-resistant recurrent ovarian cancer. *Gynecol Oncol* **163**, 254-261, doi:10.1016/j.ygyno.2021.08.020 (2021).

108 Lu, Q. *et al.* Tyro-3 family receptors are essential regulators of mammalian spermatogenesis. *Nature* **398**, 723-728, doi:10.1038/19554 (1999).

109 Angelillo-Scherrer, A. *et al.* Deficiency or inhibition of Gas6 causes platelet dysfunction and protects mice against thrombosis. *Nat Med* **7**, 215-221, doi:10.1038/84667 (2001).

110 Rokita, J. L. *et al.* Genomic Profiling of Childhood Tumor Patient-Derived Xenograft Models to Enable Rational Clinical Trial Design. *Cell Rep* **29**, 1675-1689 e1679, doi:10.1016/j.celrep.2019.09.071 (2019).

111 Donahue, B. Short- and long-term complications of radiation therapy for pediatric brain tumors. *Pediatr Neurosurg* **18**, 207-217, doi:10.1159/000120664 (1992).

112 Ahir, B. K., Engelhard, H. H. & Lakka, S. S. Tumor Development and Angiogenesis in Adult Brain Tumor: Glioblastoma. *Mol Neurobiol* **57**, 2461-2478, doi:10.1007/s12035-020-01892-8 (2020).

113 Stacker, S. A. *et al.* VEGF-D promotes the metastatic spread of tumor cells via the lymphatics. *Nat Med* **7**, 186-191, doi:10.1038/84635 (2001).

114 Holash, J. *et al.* VEGF-Trap: a VEGF blocker with potent antitumor effects. *Proc Natl Acad Sci U S A* **99**, 11393-11398, doi:10.1073/pnas.172398299 (2002).

115 Schluter, A. *et al.* CD31 and VEGF are prognostic biomarkers in early-stage, but not in late-stage, laryngeal squamous cell carcinoma. *BMC Cancer* **18**, 272, doi:10.1186/s12885-018-4180-5 (2018).

116 Hughes, I. A. *et al.* Consensus statement on management of intersex disorders. *Arch Dis Child* **91**, 554-563, doi:10.1136/adc.2006.098319 (2006).

117 Johnson, E. K. *et al.* Gonadal Tissue Cryopreservation for Children with Differences of Sex Development. *Horm Res Paediatr* **92**, 84-91, doi:10.1159/000502644 (2019).

118 Isaacs, H. *Germ Cell Tumors. In: Tumors of the Fetus and Infant*. 5-36 (Springer, 2002).

119 Wolffenbuttel, K. P. *et al.* Gonadal dysgenesis in disorders of sex development: Diagnosis and surgical management. *J Pediatr Urol* **12**, 411-416, doi:10.1016/j.jpurol.2016.08.015 (2016).

120 Talerman, A. & Roth, L. M. Recent advances in the pathology and classification of gonadal neoplasms composed of germ cells and sex cord derivatives. *Int J Gynecol Pathol* **26**, 313-321, doi:10.1097/01.pgp.0000250148.52215.ce (2007).

121 Ulbright, T. M., Young, R. H. *Tumors of the Testis and Adjacent Structures*. (American Registry of Pathology, 2013).

122 Cools, M., Looijenga, L. H., Wolffenbuttel, K. P. & Drop, S. L. Disorders of sex development: update on the genetic background, terminology and risk for the development of germ cell tumors. *World J Pediatr* **5**, 93-102, doi:10.1007/s12519-009-0020-7 (2009).

123 Mayur, P., Parikshaa, G., Anil, B., Shalini, G. & Arvind, R. 'Size does matter': Prophylactic gonadectomy in a case of Swyer syndrome. *J Gynecol Obstet Hum Reprod* **48**, 283-286, doi:10.1016/j.jogoh.2019.01.009 (2019).

124 Bumbuliene, Z., Varyte, G. & Geimanaite, L. Dysgerminoma in a Prepubertal Girl with Complete 46XY Gonadal Dysgenesis: Case Report and Review of the Literature. *J Pediatr Adolesc Gynecol* **33**, 599-601, doi:10.1016/j.jpag.2020.04.007 (2020).

125 McCann-Crosby, B. *et al.* State of the art review in gonadal dysgenesis: challenges in diagnosis and management. *Int J Pediatr Endocrinol* **2014**, 4, doi:10.1186/1687-9856-2014-4 (2014).

126 Krasna, I. H., Lee, M. L., Smilow, P., Sciorra, L. & Eierman, L. Risk of malignancy in bilateral streak gonads: the role of the Y chromosome. *J Pediatr Surg* **27**, 1376-1380, doi:10.1016/0022-3468(92)90180-f (1992).

127 Harris, C. J. *et al.* Establishing an Institutional Gonadal Tissue Cryopreservation Protocol for Patients with Differences of Sex Development. *J Urol* **204**, 1054-1061, doi:10.1097/JU.0000000000001128 (2020).

128 Van Batavia, J. P. & Kolon, T. F. Fertility in disorders of sex development: A review. *J Pediatr Urol* **12**, 418-425, doi:10.1016/j.jpurol.2016.09.015 (2016).

129 Sanders, C., Carter, B. & Lwin, R. Young women with a disorder of sex development: learning to share information with health professionals, friends and intimate partners about bodily differences and infertility. *J Adv Nurs* **71**, 1904-1913, doi:10.1111/jan.12661 (2015).

130 Finlayson, C. *et al.* Presence of Germ Cells in Disorders of Sex Development: Implications for Fertility Potential and Preservation. *J Urol* **197**, 937-943, doi:10.1016/j.juro.2016.08.108 (2017).

131 Kristensen, S. G. *et al.* Use of cryopreserved ovarian tissue in the Danish fertility preservation cohort. *Fertil Steril* **116**, 1098-1106, doi:10.1016/j.fertnstert.2021.05.096 (2021).

132 Kristensen, S. G. *et al.* A simple method to quantify follicle survival in cryopreserved human ovarian tissue. *Hum Reprod* **33**, 2276-2284, doi:10.1093/humrep/dey318 (2018).

133 Donnez, J. & Dolmans, M. M. Fertility Preservation in Women. *N Engl J Med* **377**, 1657-1665, doi:10.1056/NEJMra1614676 (2017).

134 Gellert, S. E. *et al.* Transplantation of frozen-thawed ovarian tissue: an update on worldwide activity published in peer-reviewed papers and on the Danish cohort. *J Assist Reprod Genet* **35**, 561-570, doi:10.1007/s10815-018-1144-2 (2018).

135 Shapira, M., Dolmans, M. M., Silber, S. & Meirow, D. Evaluation of ovarian tissue transplantation: results from three clinical centers. *Fertil Steril* **114**, 388-397, doi:10.1016/j.fertnstert.2020.03.037 (2020).

136 Papadakis, J. L. *et al.* Fertility Discussions: Perspectives of Adolescents and Young Adults With Differences of Sex Development. *Clin Pract Pediatr Psychol* **9**, 372-383, doi:10.1037/cpp0000373 (2021).

APPENDIX I: Workflow for Management of Gonadal Neoplasm in Two Patients with Differences of Sex Development Enrolled in an Experimental Gonadal Tissue Cryopreservation Protocol

Abstract

Objective: To outline our experimental gonadal tissue cryopreservation (GTC) protocol that does not disrupt standard of care in medically-indicated gonadectomy for patients with differences of sex development (DSD), including highlighting the multidisciplinary collaborative protocol for when neoplasm is discovered in these cases.

Methods: Two patients with complete gonadal dysgenesis (CGD) who were undergoing medically-indicated prophylactic bilateral gonadectomy elected to pursue GTC. Both were found to have gonadoblastoma on initial pathologic analysis, requiring recall of the gonadal tissue, which had been cryopreserved.

Results: Cryopreserved gonadal tissue was successfully thawed and transferred to pathology for complete analysis. Neither patient was found to have malignancy, so further treatment beyond gonadectomy was not indicated. Pathologic information was communicated to each family, including that long-term GTC was no longer possible.

Conclusion: Organizational planning and coordination between the clinical care teams, GTC laboratory and pathology were key to handling these cases with neoplasia. Processes that anticipated the possibility of discovering neoplasia within tissue sent to pathology and the potential need to recall GTC tissue to complete staging included: (1) documenting the orientation and anatomical position of tissue processed for GTC, (2) defining parameters in which tissue will be recalled, (3) efficiently thawing and transferring GTC tissue to pathology, and (4) coordinating release of pathology results with verbal communication from the clinician to provide context. GTC is desired by many families and at the time of gonadectomy and is: (1) feasible for patients with DSD and (2) did not inhibit patient care in two patients with gonadoblastoma.

Introduction

Differences of sex development (DSD, also referred to as intersex) are a diverse set of congenital conditions characterized by genitalia that is atypical or incongruent with chromosomal sex, sex chromosome aneuploidy, or disruption of sex hormone production or response[116,117]. One such DSD, complete gonadal dysgenesis (CGD, also referred to as Swyer syndrome) is characterized by aberrant gonadal development and the presence of streak gonads [118]. Streak gonads are typically defined as having variability in stromal cellularity, a lack of germ cells and no primordial follicles[118]. Streak gonads in CGD carry up to a 30% risk of gonadoblastoma and an estimated 50% risk of malignant transformation[119,120]. Gonadoblastoma can occur as early as infancy or early childhood, but most often is identified in adolescence and young adulthood[121]. Therefore, prophylactic bilateral gonadectomy is the typically recommended treatment following diagnosis of CGD[122-126]. Our team has previously described the complex process of gonadal management decision making in a multidisciplinary setting[117,127]. Individuals with DSD, including CGD, commonly experience infertility related to impaired gonadal development or long-term function, an issue that is of particular concern to patients and their families[128,129].

We previously described a novel institutional protocol for experimental gonadal tissue cryopreservation (GTC) for individuals with DSD undergoing medically indicated prophylactic gonadectomy[117,127]. When this protocol was developed, preparations were made to: (1) avoid the potential disruption of care incurred by the additional step of GTC; and (2) avoid the potential loss of tissue orientation in relation to the tissue screened in pathology if a neoplasm was identified, which (3) would trigger a tissue recall from the cryopreservation lab. These concerns were addressed through the early implementation of a comprehensive GTC protocol in case of

neoplasm diagnosis and clear, agreed-upon communication structures between all relevant departments. Through a detailed description of two cases, this report describes the GTC protocol workflow with emphasis on communication and handling of pathologic specimens for when a neoplasm is identified at the time of gonadectomy.

Case Presentations

Two patients who presented to the Ann & Robert H. Lurie Children's Hospital ('Lurie Children's') Gender and Sex Development Program (GSDP) with karyotype-phenotype discordance were found to have a diagnosis of 46, XY CGD. Patient 1 presented at 2 months of age and Patient 2 presented at 2.7 years of age. Table 10 lists clinical details for patients. In both cases, prenatal cell-free DNA screening indicated presence of Y chromosome material, but female-typical external genitalia were observed at birth. Postnatal peripheral blood chromosomal analysis confirmed 46, XY karyotype without evidence of mosaicism for both patients.

Patient 1 had positive fluorescence *in situ* hybridization (FISH) results for *SRY*, a gene located on the Y chromosome that encodes sex-determining region Y protein. At 3 weeks of age, serum studies revealed normal luteinizing hormone (2 μIU/mL), undetectable estradiol (<1 pg/mL), as well as elevated follicle-stimulating hormone (27 μIU/ mL) and undetectable anti-Müllerian hormone (<0.015 ng/mL), consistent with gonadal insufficiency. Pelvic ultrasound identified a pre-pubertal uterus and possible gonadal structures (right more prominent -**Figure 19**). The presence of uterus and normal adrenal function clarified the diagnosis of 46,XY CGD. This finding is not thought to be related to Patient 1's 46,XY CGD. Exome sequencing was offered but the family declined; thus the specific etiology of Patient 1's 46, XY CGD remains unknown.

Table 10. Patient Information

	Patient 1	Patient 2
Age at Gonadectomy (years)	1.5	3.6
Karyotype	46,XY Cells Counted: 15 Cells Analyzed: 5 Karyograms Prepared: 2	46,XY Cells Counted: 20 Cells Analyzed: 5 Karyograms Prepared: 3
Additional Genetic Testing	FISH SRY – positive DSD Gene Panel – non-diagnostic, a heterozygous variant of uncertain significance was identified in BBS1 (c.1378C>T, p.R460C). ALTERNATIVE: BBS1 c.1378C>T (R460C), heterozygous variant of uncertain significance, unknown inheritance	Periodic Fever Gene Panel – non-diagnostic, no reportable variants identified Exome Sequencing – non-diagnostic, a paternally inherited heterozygous variant of uncertain significance was identified in AMH (c.1213G>C, p.A405P). ALTERNATIVE: AMH c.1213G>C (A405P), heterozygous variant of uncertain significance, paternally inherited
Genetic Diagnosis	Unknown	Unknown
Right Gonad Morphology	typical appearance of streak gonad	Streak Gonad. Longer than left and extended more medially, right gonad measured 20x3mm.
Left Gonad Morphology	sits closer to body of uterus and has a similar shape but more full and slightly brownish color in half of gonad further from uterine body	Streak Gonad. Small irregular area on the medial edge - sent as part of the pathology portion, left gonad measured 18xmm.
Histology of Right Gonad	Dysgenetic gonad with small focus of gonadoblastoma	Gonadoblastoma. Streak Gonad. Fallopian tube tissue.
Histology of Left Gonad	Dysgenetic gonad with small focus of gonadoblastoma	Streak Gonad. Fallopian tube tissue.
Germ Cells Present?	No	No

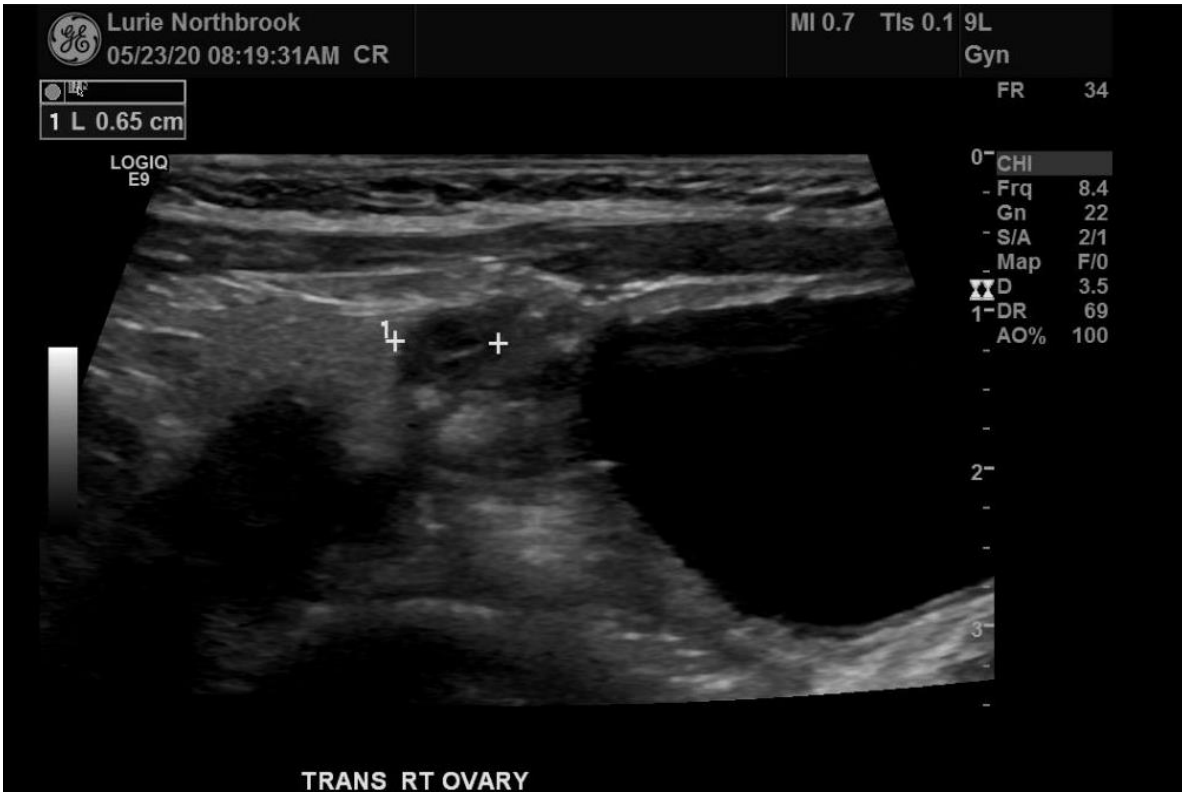

Figure 19. Pelvic ultrasound of right gonad of Patient 1.

Patient 1 had positive fluorescence *in situ* hybridization (FISH) results for *SRY*, a gene located on the Y chromosome that encodes sex-determining region Y protein. At 3 weeks of age, serum studies revealed normal luteinizing hormone (2 μIU/mL), undetectable estradiol (<1 pg/mL), as well as elevated follicle-stimulating hormone (27 μIU/ mL) and undetectable anti-Müllerian hormone (<0.015 ng/mL), consistent with gonadal insufficiency. Pelvic ultrasound identified a pre-pubertal uterus and possible gonadal structures (right more prominent -**Figure 19**). The presence of uterus and normal adrenal function clarified the diagnosis of 46,XY CGD. This finding is not thought to be related to Patient 1's 46,XY CGD. Exome sequencing was offered but the family declined; thus the specific etiology of Patient 1's 46, XY CGD remains unknown.

Patient 2's parents initially chose not to investigate Y chromosome material revealed through prenatal cell free DNA. However; at 1.7 years of age, Patient 2 was confirmed to have a 46, XY karyotype during genetic testing for periodic fever syndrome. At 3 years old, Patient 2 had normal luteinizing hormone (3.36 μIU/mL), undetectable estradiol (<2 pg/mL), elevated follicle-stimulating hormone (31 μIU/ mL), and very low anti-Müllerian hormone (0.04 ng/mL). Pelvic ultrasound identified a prepubertal uterus but no visible gonads. Based on hormonal findings indicating gonadal insufficiency, a physical exam with no evidence of androgen exposure, and lack of symptoms of adrenal insufficiency, 46,XY CGD was suspected. The family consented to exome sequencing, results of which identified a paternally inherited VUS in *AMH* (c.1213G>C, p.A405P). Chromosomal microarray analysis was offered to the family and declined; thus the specific etiology of Patient 2's 46,XY CGD remains unknown.

At the initial appointment for both patients, the multidisciplinary GSDP team reviewed the expected gonadal tumor risk for CGD, and the low likelihood of function for hormonal production and fertility. Prophylactic gonadectomy was discussed as a non-urgent procedure to be revisited. Attempted GTC was discussed as an option for patients who elected prophylactic gonadectomy, setting realistic expectations of the low likelihood that germ cells would be present in gonadal tissue of patients with a CGD diagnosis[130]. Following iterative multidisciplinary discussions over the course of several months, both sets of parents gave informed consent for laparoscopic bilateral gonadectomy.

GTC Protocol

Preoperative Counseling

Parents of both patients met with the multidisciplinary GSDP team, which included urology, endocrinology, psychology, and genetic counseling. Parents were counseled by the GSDP team regarding all management options, balancing risk of malignancy and feasibility of ultrasound surveillance with the risk tolerance of the parents. Parents were advised by the GSDP team that individuals with CGD commonly have nonfunctional streak gonads with increased tumor risk, hence the recommendation for consideration of pre-pubertal gonadectomy. The GSDP team also discussed the option of retaining gonads with serial imaging surveillance, explaining there are no established protocols for imaging type and frequency, and no currently available serum tumor markers that can reliably screen for gonadal tumors in CGD or other DSDs. The team also discussed the potential for experimental GTC should parents elect for gonadectomy. Following these discussions, both sets of parents elected to proceed with GTC during laparoscopic bilateral gonadectomy for their child.

Tissue Procurement

Laparoscopic bilateral gonadectomy under general anesthesia (tissue procurement), tissue processing for pathology, and tissue processing for cryopreservation all occurred on the same day. Patients 1 and 2 underwent surgery at 1.5 years old and 3.6 years old, respectively. Patient 1's laparoscopic findings were consistent with bilateral streak gonads. Patient 2 also had laparoscopic findings consistent with bilateral streak gonads, but there was an irregular, lobular area at the medial aspect of the left gonad (**Figure 20)**. The gonads that appeared like typical streak gonads were bisected longitudinally with one half allocated for pathological analysis, and

the other half processed for GTC, as specified in our GTC research protocol. For Patient 2, the portion of the left gonad with an atypical appearance was preferentially sent for pathological analysis per the surgeon's discretion. Both patients recovered well from surgery without intraoperative or postoperative complications, and both were discharged the same day.

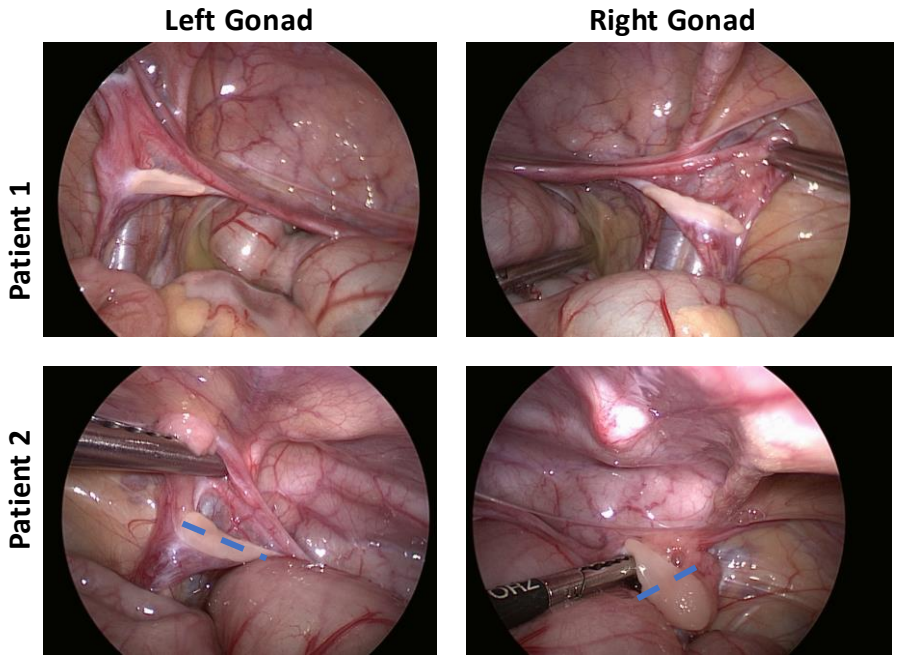

Figure 20. Surgical images. For Patient 2, the dashed blue line indicates where gonad was bisected. For the right gonad, the more bulbous, lateral half was sent to pathology

Gonadal Tissue Cryopreservation (GTC)

Set-Up

All preservation procedures were performed within a laminar flow hood using sterile technique and wearing appropriate personal protective equipment. Relevant cryovials, tubes and dishes were labeled with patient information and all materials and instruments were prepared before beginning the cryopreservation protocol. Photos were taken of tissue prior to and during tissue processing (**Figure 21)**.

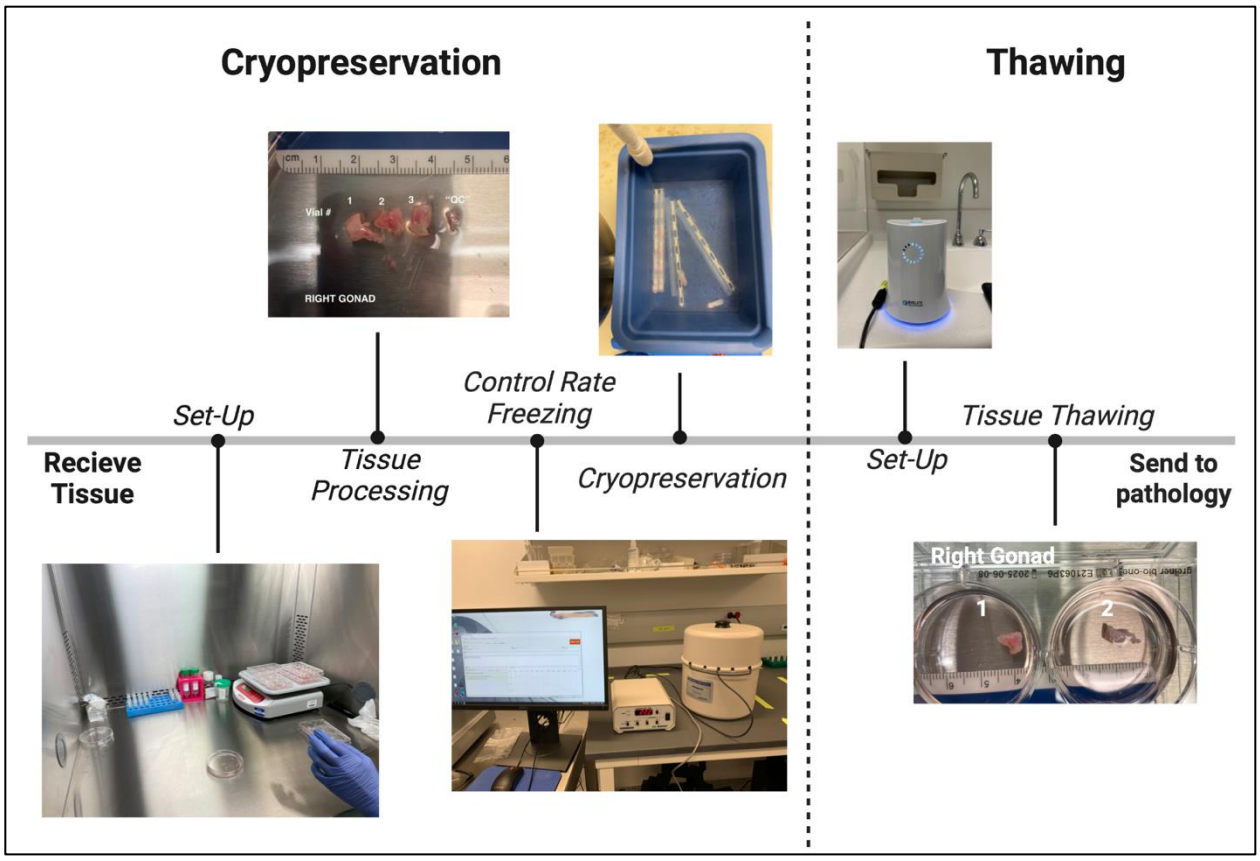

Figure 21. Cryopreservation and thawing protocol.

Tissue Processing for GTC

Gonadal tissue was placed in Oncofertility Consortium (OFC) Holding Media (Cooper Surgical ART-8040) and gross morphology and weight were recorded. Tissue for cryopreservation was processed sagittally or parallel to the cut side into 1.5 – 2.0 mm thick slices and transferred to a new dish of Holding Media. The slices were then processed into 3 – 5 mm wide strips. The weight of the strips was recorded. The orientation of the tissue pieces in how they related to their original anatomical location was tracked through the entire protocol. The smallest piece of tissue was designated on the tube for use in quality control ("QC") assessments to be performed post-thaw at the laboratory's discretion.

Cryopreservation

Processed tissue strips were transferred into dishes containing OFC Freezing Media of MOPS buffer, 1.5M ethylene glycol and 0.1M sucrose (Cooper Surgical ART-8050). Tissue strips were incubated in OFC Freezing Media on an orbital shaker for 10 minutes then transferred into pre-prepared cryovials containing OFC Freezing Media. This process is conducted within the sterile hood on a chilled ice pack maintained at 2 – 4°C. Tissue was then transferred to cryovials (Nunc 377267) containing approximately 1 ml of chilled OFC Freezing Media.

Control Rate Freezing

Tissue stored in cryovials was cryopreserved using a common "slow freeze" or control-rate freezing technique that has been used for successful live birth following thaw and autotransplantation of ovarian tissue[131-135]. Briefly, cryovials with tissue are stored at 4 - 6 °C for 30 minutes prior to putting them in the control rate freezer (Biogenics #CL8800i). The vials are cooled to –7 °C and seeded, then slowly cooled to -40°C before submerging the vials in liquid nitrogen. The cryovials are stored in a liquid nitrogen freezer on site at Lurie Children's.

Pathological Analysis

Within one week of surgery, pathological assessment indicated the presence of gonadoblastoma in both gonads for Patient 1 and in the right gonad for Patient 2. There was no gonadoblastoma in the left gonad that had a noted irregular, lobular appearance for Patient 2 (**Figure 22)**. No germ cells were identified in the gonadal tissue of either patient. Of note, Patient 2 was diagnosed with gonadoblastoma after the 21st Century Cures Act was implemented in

April 2022, which imposes automatic release of pathology reports to patients upon posting. The surgical team briefly paused automated release of records, to allow for initial verbal communication of the pathology results to the parents with clinical context, with the aim of minimizing parental distress. The patient's parents were contacted within 24 hours of pathology reports being available to clinicians and informed of the results. Families of both patients appeared to have an appropriate understanding of the pathology results, including the need to recall the cryopreserved tissue in liquid nitrogen storage for complete analysis by pathology and thus no gonadal tissue would be preserved for potential future use.

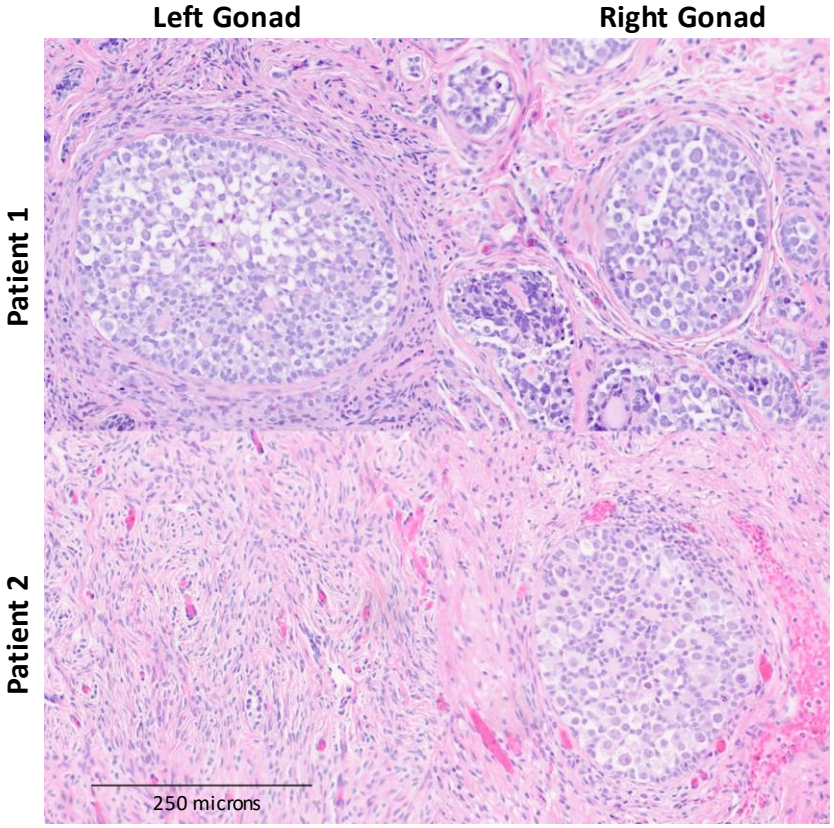

Figure 22. H&E stained gonadal tissue indicating gonadoblastoma in the initial half of the gonad designated for pathology in both gonads of Patient 1 (top row) and in the right gonad of Patient 2 (bottom row).

Tissue Thawing and Preparation for Follow-up Pathological Analysis

Set-Up

All procedures were performed within a laminar flow hood using sterile technique and wearing appropriate personal protective equipment. Relevant cryovials, tubes and dishes were labeled with patient information and all materials and instruments were prepared before beginning the thawing protocol. Thawing media was made by diluting the OFC Freezing Media with OFC Holding Media in 2:1, and 1:2 volumes.

Tissue Thawing

Cryovials containing the patient tissue were removed from the liquid nitrogen storage tank and maintained in liquid nitrogen until they were individually placed in the ThawSTAR (Biolife Solutions CFT2). The order and number noted on the vials referenced the anatomical location of each tissue piece, and therefore, this numbering scheme was maintained through the thaw process. Photos were taken of tissue after thaw (**Figure 21)**.The tissue was put through the prepared thaw media at room temperature for 10 minutes each before a final wash in OFC Holding Media. Lastly, the thawed tissue was transferred into new vials containing Phosphate Buffered Saline, again labeled with the number assigned to its location in relation to the entire specimen.

Pathological Analysis of Recalled Tissue

The thawed tissue was brought to pathology with an image that acted as a key for orientation of each piece of tissue to match the anatomical location in relation to the first half of the gonad originally reviewed by pathology. Pathology fixed the tissue in 10% neutral-buffered

formalin, processed and embedded the tissue in paraffin. The paraffin sections were stained with hematoxylin and eosin (H&E) and reviewed for an updated diagnosis. Recalled tissue from Patient 1 were identified as containing features of gonadoblastoma but no malignancy in either gonad **(Figure 23)**. Analysis of recalled tissue from Patient 2 revealed no features of neither gonadoblastoma nor malignancy **(Figure 23).**

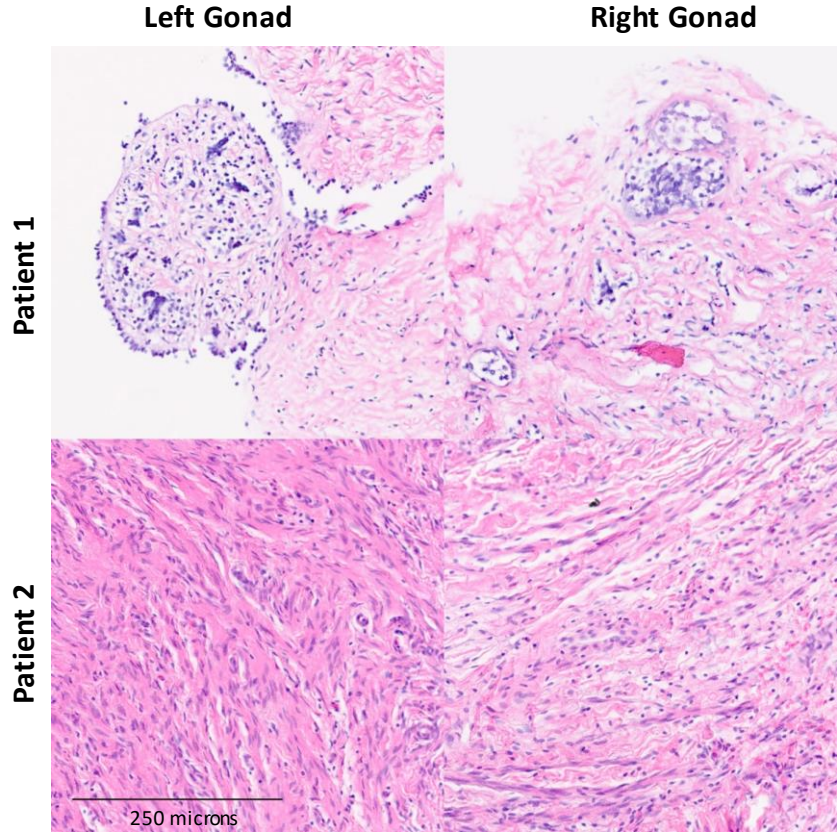

Figure 23. H&E stained recalled gonadal tissue indicating gonadoblastoma in both gonads of Patient 1 (top row) but in neither of Patient 2's gonads (bottom row).

Post-Operative Counseling and Tissue Disposition

During clinical follow-up, the multidisciplinary team reviewed pathology, future care and support including eventual disclosure of medical history to the patient, pubertal endocrinological needs, and future fertility and family building potential. The team discussed the importance of early disclosure related diagnosis, surgical history, and implications in a developmentally-appropriate way to ensure patients felt adequately supported throughout this process. The patients' parents once again appeared to have an appropriate understanding of the entire surgical, pathological and cryopreservation process, and final tissue disposition as demonstrated by parents' ability to summarize their understanding and ask relevant, thoughtful questions. Follow up was tentatively scheduled for 2 – 3 years.

Discussion

Fertility potential is a concern for many individuals with DSD and their families[128,129,136]. Recent work has demonstrated that germ cells are present in some individuals with DSD[130]. GTC for individuals with DSD who have an elevated risk of gonadal neoplasia involves additional steps beyond the standard testicular or ovarian cryopreservation workflow, which was part of the motivation for our team to create a separate IRB protocol and standard operating procedures from ovarian or testicular tissue cryopreservation for patients with cancer or non-oncologic conditions treated with stem cell transplant. For patients with DSD, the primary concern is that the cryopreserved tissue may need to be evaluated to make final staging and clinical decisions. We address these concerns by following a pre-established workflow with provisions for cases in which gonadoblastoma or other neoplasia are identified **(Figure 24).** Implementation of such a protocol enables providers to present GTC as a safe option to individuals with DSD despite tumor risk.

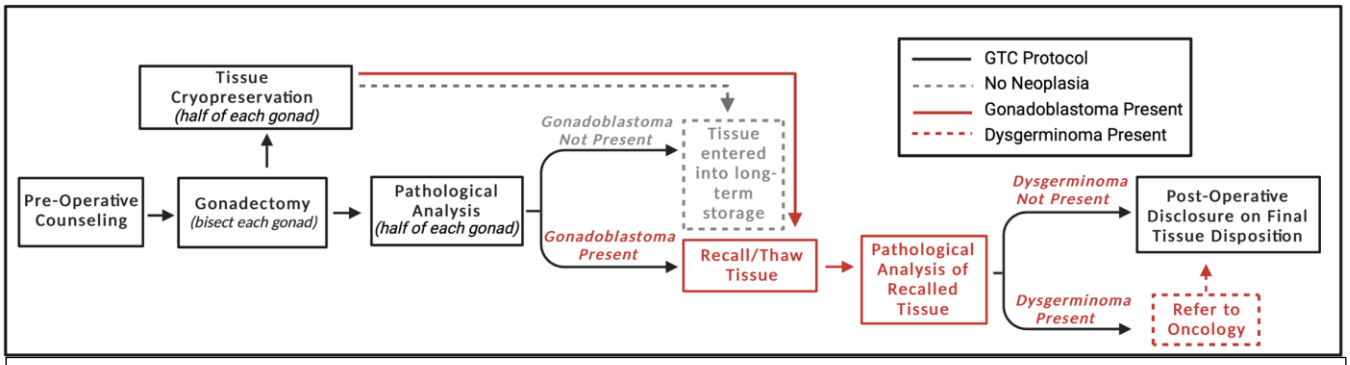

Figure 24. GTC Workflow highlighting steps for tissue handling protocol for when neoplasia is present.

We previously presented the first institutional GTC protocols and soon after, presented a cohort of patients with various DSD diagnoses who chose to pursue GTC[117,127]. Four major strengths of this protocol are: (1) the multidisciplinary approach; (2) coordination across departments; (3) pre-establishment of a detailed protocol that anticipated the potential recall of cryopreserved tissue for evaluation in the case of neoplasm, and (4) opportunity for families to make the final decision on whether to proceed with cryopreservation, discard or donate cryopreserved tissue following the final pathology report, if germ cells were not found. In cases where germ cells are not initially identified by pathology in gonadal tissue following medically-indicated gonadectomy, GTC is still presented as an option in that hopes that either (1) germ cells exist in portions of the tissue not examined by the pathologists and (2) biological fertility can still be facilitated through future advances in assisted reproductive technology.

While the presence of germ cells is suggestive of fertility potential, further work is needed to identify the optimal age for GTC, as the quantity of cells may decrease with age, and to assess the functionality and quality of these gametes[130]. A major concern for any fertility preservation (FP) protocol is the presence of neoplasia in cryopreserved tissue. The presence of neoplasia in the tissue would contraindicate use of this tissue for autotransplantation to restore fertility. Furthermore, because the tissue may not have natural fertility potential, the cryopreserved gonadal tissue for patients with DSD would likely be used to grow and mature gametes *in vitro* using future and existing assisted reproductive technologies. The patients and families are thoroughly counseled on the realities of the potential utility of this tissue as well as potential discordance between the patient's gender identity and gonadal sex. However, there are families that value this option and choose to pursue GTC with medically indicated gonadectomy[117].

In the present case series, we build on our prior work by providing a detailed report of our GTC workflow by discussing two cases in which neoplasia was identified. We report a clear and thorough system in which a multidisciplinary team collaborated to provide preoperative counseling to patient families, procure tissue, cryopreserve half of the tissue, assess the other half for presence of neoplasia, recall cryopreserved tissue, conduct further pathologic analysis on recalled tissue, and provide postoperative counseling to parents without delaying or inhibiting patient care.

A core feature of our approach is the communication and coordination between different departments, which serves to streamline the GTC protocol workflow. Collaboration between the tissue processing team and the surgical team allowed for the procurement of gonadal tissue and ensured that tissue was handled in a way that maintained the sterility of the half that was cryopreserved for potential future use. Communication between pathologists and the surgical team ensured that the patients' parents were contacted by the appropriate physician and briefed on pathology results in a timely manner. Coordination between the cryopreservation lab and pathology ensured that the thaw and transfer of tissue was performed efficiently while maintaining the anatomical orientation of the cryopreserved and thawed gonadal tissue to be reviewed.

The existence of a detailed GTC research protocol, developed through multidisciplinary collaboration and clinical ethics involvement, enabled the implementation of this protocol and efficient delivery of care[127]. While it is impossible to foresee all issues, substantial efforts were made to account for potential problems. This is particularly relevant in the case of time sensitive procedures. Risk of neoplasia was identified and discussed with the patients' family before the GTC protocol was offered to patients, which minimized confusion and miscommunication upon

diagnosis of gonadoblastoma in these cases. All gonadal tissue strips were labeled and frozen for easy identification upon thawing, expediting the process of returning temporarily stored tissue to pathology for further analysis. Additionally, the tissue for cryopreservation was handled using sterile techniques and arrived directly from the operating room instead of from the non-sterile pathology space. While neither patient in this report presented with malignant germ cell tumor on recalled tissue, it is important to expedite any additional pathological analysis if malignant transformation is identified.

Diagnosis of gonadal neoplasm can be stressful for patients and their families[136]. During pre-operative counseling, the patients' parents were counseled on the likelihood of gonadal neoplasia as well as how our GTC protocol accounts for potential diagnosis of neoplasia. In our follow-up conversations, both sets of parents expressed understanding of the GTC protocol, implications of gonadoblastoma for GTC, their choices regarding final tissue disposition, and potential complications that may arise in the future use of the tissue, such as discordance between the patients gametes and gender identity and the need for assisted reproductive technologies in the use of gametes.

Conclusion

GTC at the time of gonadectomy is feasible for patients with CGD. Implementation of a multidisciplinary GTC protocol did not interfere with the care of two CGD patients with a diagnosis of gonadoblastoma.